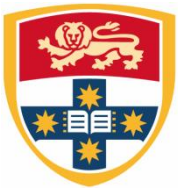

THE UNIVERSITY OF SYDNEY

Master of Philosophy (Engineering & IT)

Thesis

Statistical Shape Modelling and Segmentation of the Respiratory Airway

Robin Huang

Faculty of Engineering, School of IT

University of Sydney

Supervisors

Dr. Jinman Kim, Dr. Changyang Li

A thesis submitted in partial fulfilment of requirements for the degree of Master of Philosophy

Statement of originality

This is to certify that to the best of my knowledge, the content of this thesis is my own work. This thesis has not been submitted for any degree or other purposes.

I certify that the intellectual content of this thesis is the product of my own work and that all the assistance received in preparing this thesis and sources have been acknowledged.

Robin Huang

Abstract

The human respiratory airway consists of the upper (nasal cavity, pharynx) and the lower (trachea, bronchi) respiratory tracts. Accurate segmentation of these two airway tracts can lead to (i) a better diagnosis and interpretation of airway-specific diseases; (ii) improvement in the localization of abnormal metabolic or pathological sites found within and/or surrounding the respiratory regions; and (iii) be of great benefit in modeling and perform simulations on targeted airway structures for surgery planning, drug delivery and fluid-dynamics research. Due to the complexity and the significant variability displayed in the anatomical structure of the upper respiratory airway along with additional challenges such as distinguishing and separating the nasal cavity from non-respiratory air-filled regions such as the paranasal sinuses, it is difficult for existing algorithms to accurately segment the upper airway without manual intervention. Subsequently, there is significant scope in the formulation of a normalized model of the upper airway based on a statistical averages taken from a population distribution.

The lower respiratory tract consisting of the trachea and bronchial airway, while possessing a less complex structure when compared to the nasal cavity, has also proven to be difficult to segment when the medical images are taken via PET-CT due to the contrast issue resulting from a lowered radiation dosage. In order to efficiently and accurately segment both structures within the respiratory airway, knowledge of the anatomy through the form of shape priors are essential. Furthermore, the ability to model the anatomical variations within the airway, and to formulate statistical averages and variations of the anatomy is desired.

This thesis presents an implicit non-parametric framework for constructing a statistical shape model (SSM) of the upper and lower respiratory tract, capable of distinct shape generation and be adapted for segmentation. An SSM of the nasal cavity was successfully constructed using 50 nasal CT scans. The performance of the SSM was evaluated for compactness, specificity and generality. An averaged distance error of 1.36 mm and 1.47 mm was measured for specificity and generality assessment, where the specificity measurement was calculated based on the average of 50,000 randomly generated nasal shapes.

The constructed SSM was further combined with a modified locally constrained random walk algorithm to segment the nasal cavity. The proposed algorithm was able to automatically segment the complex nasal anatomy through the introduction of a robust multi-atlas initialization for seeds derivation and demonstrated its capability at separating the nasal airway from other connected airway regions using shape priors produced from the SSM. The proposed method was evaluated on 30 CT images and

outperformed comparative state-of-the-art and conventional algorithms. Its superior performance was demonstrated with a dice similarity coefficient of 90.1±2.2 and an average distance error of 0.34±0.07 mm. The clinical significance of the algorithm was demonstrated through directly comparing the computational fluid dynamics (CFD) outcomes of turbulent flow on nasal models produced from our algorithm against models produced from ground truth segmentation. The outcome of the CFD revealed minimal differences in airflow, and indicated the potential possibility of our algorithm as a faster, more efficient alternative to manually segmenting the nasal cavity for the creation of CFD models.

For the lower airway, a separate algorithm was proposed to automatically segment the trachea and bronchi, and was designed to tolerate the image characteristics inherent in low-contrast CT images. The proposed algorithm was able to accurately and robustly segment the airway through the introduction of: (i) a robust multi-atlas initialization which incorporated shape priori knowledge for seeds derivation; and (ii) a modified knowledge-based random walk segmentation that utilizes the derived seeds and manipulates the weights of the edge paths in a locally constrained search space. The proposed algorithm was evaluated on 20 clinical low-contrast CT from PET-CT patient studies and demonstrated better performance (87.1±2.8 DSC and distance error of 0.37±0.08 mm) in segmentation results against comparative state-of-the-art algorithms.

Acknowledgement

First and foremost I would like to thank Prof. Jinman Kim for being my supervisor throughout the years and has provided constant guidance and help. His expertise in medical imaging processing improved my research skills and prepared me for the future challenges. Next, I would like to thank Dr. Changyang Li, my auxiliary supervisor, for providing the assistance that others couldn't provide.

I would also like to acknowledge Prof. Paul Young and those at the Woolcock Institute for providing the research data and support for this research. I would like to further thank both Dr. Gregory King and Dr. Nick Stow for lending me their expertise on the medical side of this research.

Finally, I would like to thank everyone at the BMIT group on level 5 of SIT for constantly assisting me along the way, with particular mentions to Dr. Ashnil Kumar, Dr. Younhyun Jung, Lei Bi, Michael de Ridder, Euijoon Ahn. Without their help, I would not have been able to graduate on time.

List of Publications

Journals

[Under Preparation]**R. Huang**, C. Li, P. Young, G. King, N. Stow, C. Phillips, J. Schimd and J. Kim, "A level set approach to 3D statistical shape modelling of nasal cavity", *PloS One,* 2016.

[Under Preparation] **R. Huang**, A. Li, D. Fletcher, A. Nedanoski, J. Schmid, P. Young, N. Stow, L. Bi, D. Traini, J. Kim "A CFD Targeted Framework for Automated Segmentation of the Nasal Cavity in Computed Tomography", Journal of Biomechanics, 2016.

Conferences

R. Huang, A. Li, L. Bi, C. Li, P. Young, D. Feng, and J. Kim "A Locally Constrained Statistical Shape Model for Robust Nasal Cavity Segmentation in Computed Tomography," in *International Symposium on Biomedical Imaging: From Nano to Macro (ISBI)*, (accepted), 2016.

R. Huang, L. Bi, C. Li, Y. Jung, J. Kim, M. Fulham, and D. Feng "A Locally Constrained Knowledge-Based Random Walk Approach for Airway Segmentation on Low-Contrast Computed Tomography (CT) Images," *International Conference on Digital Image Computing Techniques and Applications (DICTA)*, 2015.

Table of Contents

List of Tables and Figures

Chapter 1. Introduction

1.1 Overview

The human respiratory system is a major biological system which provides the body the functionality to respirate (i.e. the exchange of oxygen and carbon dioxide between an organism and the environment). Within this system, the respiratory airway which consists of the upper (nasal cavity, pharynx) and lower respiratory tract (trachea, bronchi) is a vital passage for the transportation of oxygen into the lungs, maintains olfactory function allowing the body the ability to smell, regulates the overall temperature of the body, and acts as a primary filtering mechanism for foreign particulate matter [1]. The location and structure of the upper airway tract further provides a means for targeted drug delivery to the brain with potential to treat diseases such as Alzheimer's and Meningitis [2]. Due to the complexity of the respiratory system, disorders and infections within the airway are common (i.e. viral and fungal infection, cilia dysfunction, septal deviations, tracheal stenosis, etc.), and can often be the cause to other health related problems such as sleep apnea and cardiovascular risks [3-5].

In order to achieve a better understanding on the physiology and pathology of the respiratory airway, accurate modelling of the anatomical structure is essential. The term modelling, used in this thesis, is an activity defined as the mapping of the anatomical structures and components within a pre-determined section of the human body. The activity seeks to capture and represent knowledge of the anatomical structure of interest. This knowledge can then be used for a variety of purposes such as image *segmentation* and *visualization*, but more importantly, the captured knowledge can further be used for the formulation of physical and computerized models.

Accurate representations of the respiratory airway that are capable of capturing anatomical significance are vital for a wide range of research where such models have been used to describe the effects of airflow patterns on different pathologies including sleep apnea [5-7], atrophic rhinitis [8], sinus disease [9, 10], septal deviation [11, 12], and hypertrophic turbinates [13] etc. Airway models have also been used to describe the impact of airflow following nasal turbinate reduction [14, 15], septoplasty [14], implants [8], and sinus surgery [16, 17]. A number of studies have also investigated airflow in the same patient before and after having performed surgery [17, 18], and further studies have tried to address the effects of inter-individual variability in the nasal and airway anatomy [19-22]. Another area which required accurate models of the respiratory airway is nasal drug delivery, where studies have been focused on analyzing the

deposition of nanoparticles under the effects of airflow, and with potential to target brain specific diseases or for targeting diseases in the respiratory tracts that were difficult to treat [19, 23-25]. For additional details, the following surveys and reviews summarized over 60 studies involving the usage of airway models [26-28].

Although a significant amount of research have been conducted, our understanding on the physiology and pathology of the respiratory airway can still be improved. As concluded in prior studies on the respiratory anatomy, the amount of variations in the structure of the upper airway differs significantly across a population [29, 30], and hence concerns have been raised regarding the use of airway models derived from single patient profiles as a valid means for conducting generalized research [21]. As shown in a population-based numerical simulation study, the differences in nasal structure could impact greatly on the outcomes of each flow distribution [22]. Hence, recent studies have begun to take note of the variability of the airway structure and have started to conduct quantitative research using large amounts of single patient models [21, 31, 32]. In addition, population-based studies have also began to focus on the creation of standardized or idealized models of the upper airway, as evident in the works of [33, 34] where a standardized model of the Adult Malaysian female based on 24 samples and an idealized model of the infant airway based on 10 samples have been explored.

Overall, research on the respiratory anatomy is still ongoing, with a wide range of potential areas to further study and to improve, especially with the recent interest in regards to drug delivery. The need for accurate models of the respiratory anatomy is stronger than ever, particularly for normalized or standardized models based on a large population sample. Subsequently, due to the complexity of the respiratory airway, the process for model creation via image segmentation is difficult and time consuming [27], causing quantitative research that requires large amounts of airway models to be troublesome to perform. Hence, there is significant scope in improving segmentation accuracy and efficiency for airway structures and as well as establishing a framework for normalized model creation.

Image segmentation is the process of partitioning an image into smaller segments, often grouped together by color or texture [35]. In medical images, these segments would correspond to different tissue classes or organs, essentially dividing the human body into separate anatomical components. It is the first step towards modelling the anatomy. The work of this thesis is focused on the modelling and segmentation of the respiratory airway.

1.2 Research Context and Motivation

There is a significant amount of scope for improving existing methods of airway segmentation in order to allow for more accurate and efficient ways of patient-specific model generation. Furthermore, the ability to construct normalized as well as statistically quantified models of the respiratory airway based on a large population sample is also highly desired.

Statistical shape models (SSM) are a well-established method for computing accurate 3D representations of a targeted anatomy. Based on a set of training data, the variability of the class of training data is modelled by means of a normal distribution, and SSM can then formulate statistical averages and variations, as well as reconstruct patient specific anatomical representations through combining the statistical priors with the observed data. SSMs have been employed in many applications due to its wide range of capabilities such as in object recognition [36], image manipulation [37], surgery planning [38] as well as segmentation [39]. The existence of a statistical shape model (SSM) of the respiratory airway allows for the ability to generate statistically valid yet distinct structures of the modelled anatomy with precise control over the degree of variation, and the modelled variations can further adapted as *shape priors* to segment new images for the creation of additional patient-specific models.

Although a standardized model of the nasal cavity of an adult Malaysian female [33] has been created, a framework for modelling the statistical variations of the components within the respiratory anatomy have not yet been developed. This thesis focuses on SSM's ability at modelling the anatomical variations amongst a population distribution for shape generation and segmentation. In order to apply SSM on the respiratory airway, a successful method of shape model construction needs to be explored and established.

1.3 Aims and Contributions

The aims of this thesis are to establish a reliable framework for the creation of:

- A statistically quantified models of the upper respiratory airway.
- To map the variations in the anatomical structure across a population distribution.
- Improve the accuracy and efficiency of airway model generation via image segmentation through the incorporation of statistical prior knowledge.
- To optimize the methods of segmentation for 3D printing.

In particular, this thesis focuses on addressing the following issues that were encountered throughout this research project:

- Modelling the complex variations observed in the respiratory anatomy across a population distribution.
- Overcoming the lack of boundary between connected airway structures for segmentation.
- Establishing a reliable initialization method for automated airway segmentation.
- Resolving leakage issues encountered in low-contrast medical images.
- Segmenting thin airway structures with ambiguous intensity values due to the blurriness of the medical image.

These issues reflect the challenging aspects of airway segmentation which causes conventional methods to fail. This thesis will demonstrate in later chapters the limitations of current segmentation algorithms at tackling these mentioned problems. This thesis makes the following technical contributions aimed at addressing these issues:

- An automated segmentation framework was established for both upper and lower airway segmentation.
- The ability to identify and separate the nasal cavity from other connected airway structures.
- Improving and modifying existing algorithms and optimizing them for airway segmentation.
- Robust localization of region of interest (ROI) in low-contrast medical images.
- Combining graph-based algorithms with SSM and adapting it for airway segmentation
- Deriving an efficient initialization method for seeds derivation based on atlas registration.
- Proposing a novel energy localization constraint optimized for airway voxels.

Additional contributions were made as part of this research:

- A framework was derived for the construction of a 3D statistical shape model for the nasal and tracheal airway.
- A normalized model along with 50,000 other randomized models of the nasal cavity were generated with suitability for numerical simulations.
- A framework for customized 3D nasal printing was established for both patient-specific and population-specific nasal models.

1.4 Thesis Organization

This thesis is organized as follows. Chapter One provides the general overview of the thesis as well as states the motivations, research aims, and contributions. Chapter Two and Three presents related work in medical image segmentation and respiratory airway modelling. In Chapter Two, prerequisites in anatomy and medical imaging modalities are provided. The segmentation literature is notably presented under Chapter Three, which briefly covers the majority of segmentation algorithms which take advantage of anatomical knowledge. Main advantages and drawbacks of presented algorithms are reported to better highlight some of the efforts made in this thesis to improve some existing algorithms. Subsequently, the methodology of SSM is thoroughly detailed in Chapter Four. It further describes how shape priors are built from training data, and its use is then depicted in Chapter Five, where methods of airway segmentation incorporating shape prior knowledge have been tested and presented on both the nasal cavity and the trachea-bronchi structure. Evaluation of shape model construction is depicted in Chapter Four. Evaluation of airway segmentation algorithms are presented in Chapter Five. Chapter Six focuses on the clinical applications of the segmentation algorithms, especially in the field of nasal computational fluid dynamics. Chapter Seven discusses the strength and limitations of the work presented in this thesis. Finally, appendices are provided to give additional details.

Chapter 2. The Respiratory Airway

2.1 Introduction

In this chapter, detailed description of the respiratory anatomy is presented along with the imaging modalities used to capture the information onto digital image. Section 2.2 focuses on the anatomical details of the respiratory system. Section 2.3 reports the common acquisition modalities to image the respiratory system including the current known weakness of these modalities. Section 3.4 provides detailed summary of existing literature on the segmentation and modelling of different structures within the respiratory tract.

2.2 Anatomy

The respiratory airway within the human body is comprised of the upper and lower respiratory tract, with the upper tract consisting primarily of the nasal cavity, paranasal sinuses, pharynx, and the larynx. The lower tract is composed of the trachea, bronchi, and lungs. The upper respiratory tract is mainly responsible for providing the transportation of air (atmospheric gases) to the lower tract while at the same time acting as a filtration mechanism to prevent foreign substances from entering the body. The lower respiratory tract divides the air that has been breathed into the body, and directs them to the lungs for respiration. The oxygen in the air is taken into the blood stream for cellular respiration while other gases along with the waste CO2 is exhaled back out.

This thesis is targeted towards the statistical shape modelling and segmentation of the main respiratory airway consisting of the nasal cavity, pharynx, trachea, and bronchi which forms a direct passage leading from the entrance of the nostrils to the lungs, and particularly focuses attention on the nasal cavity as well as the trachea and bronchi airway passage due to these components being the primary targeted structures for segmentation. Section 3.2.1 goes into further details on the anatomy of the nasal cavity, as well as briefly outlines the motivations and challenges involved in nasal cavity segmentation. Section 3.2.2 provides the same set of descriptions for the trachea and bronchi airway.

2.2.1 Nasal Cavity

The nasal cavity belongs to the upper respiratory tract and is a major passage for the transportation of oxygen into the lung, providing olfactory function and acting as a primary filtering mechanism for foreign particulate matter. The nasal cavity is located below the base of the brain and above the oral cavity. The

structure of the nasal cavity begins from the nostrils and ends at the *pharynx* (airway passage leading towards the throat), and is composed of the left and right *nasal fossa* passage divided in the center by the *nasal septum*. The two nasal passages terminate at a common chamber that leads to the pharynx. The lateral walls of the nasal cavity are formed of the *maxilla*. Surrounding the nasal cavity are four pairs of pocket-filled airspaces called the *paranasal sinuses* (each pair possessing their own name) which are connected to the nasal cavity through small orifices called *ostia*. An overall break-down of the upper respiratory tract in sagittal view is shown in figure 2.2.1.1 below.

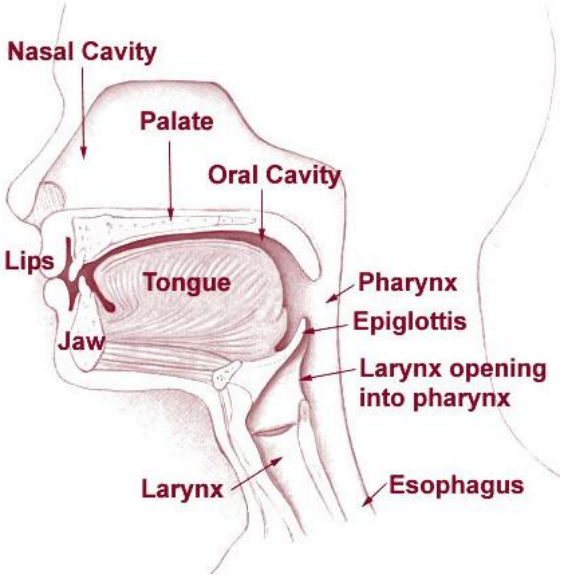

Figure 2.2.1.1. Cross-sectional view of the upper airway

The nasal cavity is about 12 cm long; the volume of each nasal fossa is 12 ml and has a surface area of around 150 cm^2 [23]. The left and right passages of the nasal cavity both consist of three different regions, namely the vestibule, the olfactory region and the respiratory region. The nasal vestibule lies at the entrance of the nasal passage with an area of about 0.6 cm^2. The respiratory region comes next and contains three nasal turbinates; the superior, the middle and the inferior turbinate. These turbinates project from the lateral wall of each half of the nasal cavity. The olfactory region is situated at the roof of the cavity and covers about 10% of the total surface area.

2.2.2 Trachea and Bronchi Tree

The trachea is a tube-like passage linking the cricoid cartilage of the larynx to the bronchi, forming part of the conducting system which transports air from the external environment to the lungs. The cervical part of the trachea lies generally in the median position, although this varies slightly depending on the position

of the head. The thoracic part of the trachea crosses the aortic arch, thus its positioning is moved slightly to the right at this level. The trachea bifurcates to form the two bronchi at the level of the 4th-6th intercostal space. The trachea contains numerous rings of hyaline cartilage which are C-shaped, being dorsally incomplete, connected to each other by elastic connective tissue. The ends of the incomplete rings are joined by the smooth trachealis muscle. The structural conformation of the trachea prevents collapse due to traction forces, whilst allowing it to adjust in length and diameter, as the neck moves and the diaphragm contracts. The trachea's walls are made up of a number of layers including the inner mucosa, fibrocartilaginous middle layer, and adventitia (in the neck) or serosa (in the thorax).

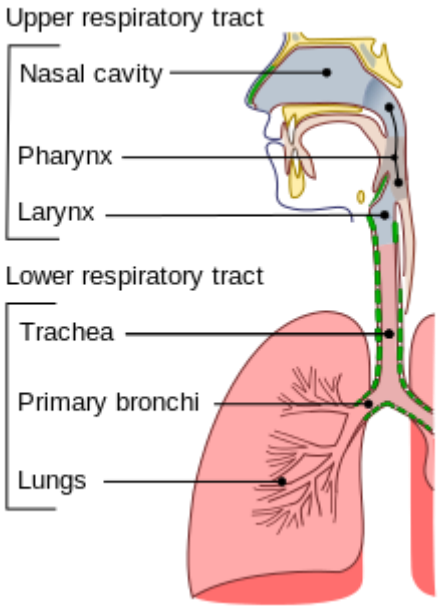

Figure 2.2.2.1. Diagram of the upper and lower respiratory tract.

The bronchi begins from where the trachea bifurcates into the left and right lung, approximately halfway between the thoracic inlet and the diaphragm. It divides into two principle bronchi, tubes which conduct air into the lungs, and they divide into two lobar bronchi for the left lung, and into four lobar bronchi for the right lung. These further divide into smaller bronchi and bronchioles within the lung tissue. The structure of the larger bronchi is identical to that of the trachea. On the smaller bronchi the C-shaped cartilage rings are gradually replaced by irregular plaques of cartilage. Bronchioles have no cartilage at all. The bronchioles are less than 1mm in diameter, and undergo further divisions, the last of which is characterized by the loss of goblet cells.

2.3 Imaging Modalities

Medical imaging is the technique and process of creating visual representations of the interior of the human body for clinical analysis and intervention. The commonly used modalities include computed tomography (CT), magnetic resonance imaging (MRI), ultrasound etc. However, for the imaging of the respiratory airway, the primary modality used is CT. Hence, the following section will briefly go over the some of the characteristics of CT, as well as its strength and limitations with regards to modelling and segmenting the airway.

2.3.1 Computed Tomography

Computed Tomography (CT) is a medical imaging procedure which utilizes computer processed X-Rays to produce tomographic images or "slices" of the human body [40]. The process typically projects x-rays at different angles along an arc of a circle and reconstructing them into a single 3D image. That is, ionising radiation is emitted from one point on a circle to a digital detector on the opposite side of the circle. Both ends of the device rotates around the body, picking up a number of angles of the same image while at the same time moving uniformly from one end of the human body to the other. This allows the height of the image to be constructed from very thin image slices stacked upon one another. The motion along and around the patient's body can be seen in the figure below.

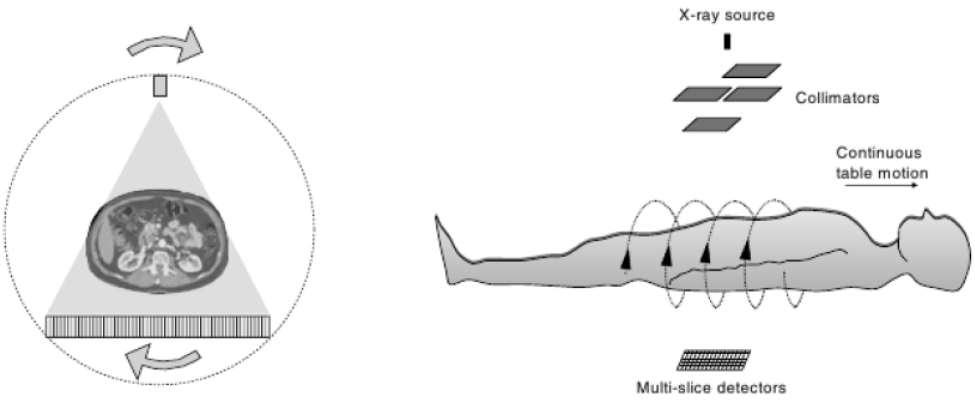

Figure 2.3.1.1. Diagram showing how 3D CT images are taken.

While CT imaging is essentially a more advanced method of X-Ray imaging, the major advantage in CT is that it creates a three dimensional reconstruction of the imaged body. CT imaging is often used to make assessments of a body part's structure, diagnosis of diseases, injury and particularly cancer. It is also used

as aid for surgery planning and radiotherapy. CT imaging is one of the few imaging techniques which provide humans the ability to view their internal organs.

2.3.2 Positron emission tomography

Positron emission tomography (PET) is a functional imaging procedure that produces a three-dimensional image of functional processes in the body. PET maps the changes in body metabolism through detecting the gamma rays emitted indirectly by a positron-emitting radionuclide (tracer), which is injected into the blood stream prior to scanning. 3D images of the tracer concentration within the body are then constructed by computer analysis to formulate the final PET images. Due to the nature of PET being a functional imaging procedure, it does not include details of the anatomy as it only depicts the spatial distribution of metabolic activities within the body. In order to better localize and provide easier understanding of the information depicted in PET, anatomical information gained from CT is often overlaid on top of PET. Hence, PET-CT have become one of the standard methods for obtaining detailed anatomical and metabolic activity within the human body.

2.3.3 Image resolution and contrast

Positron emission tomography (PET) combined with computed tomography (CT) is a standard routine imaging modality for the diagnosis and interpretation of malignant diseases within the respiratory tract. Accurate airway segmentation is critical for the localization of sites of abnormal metabolism detected with PET-CT. Such localization is pivotal to accurate disease staging prior to consideration of surgery and for radiation therapy planning. However, the CT performed in PET-CT has a lower radiation dose when compared to conventional chest CT. This results in images with a relatively lower soft tissue contrast which makes the separation of the airway tree from adjacent structures challenging.

Compared to conventional or high resolution chest CT, low-contrast CT images from PET-CT experiences more anatomy related artefacts as well as less anatomical details. Figure 2.3.3.1 exemplifies the difference between low-contrast CT with high-resolution CT. In this example, we can see that when compared against low-contrast CT, high-resolution CT exhibits clearer boundary distinctions between airway and non-airway voxels. For the modelling and segmentation of the trachea and bronchi, the data are derived from 20 PET-CT studies.

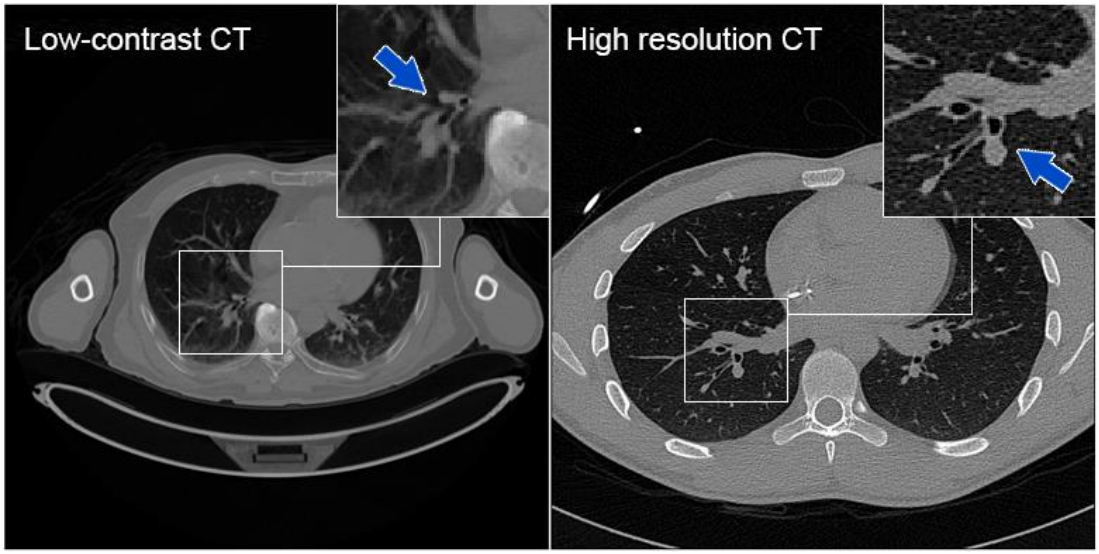

Figure 2.3.3.1. Comparison of airway structure between a low-contrast CT (left) 0.97x0.97x3 mm pixel resolution (512x512) and a high-resolution CT (right) with 0.6 x 0.6 x 0.6 mm pixel resolution (512x512). The inserts are1.5x zoomed images. The high-resolution CT has greater anatomical details of the airways (marked by arrows).

2.4 Related Work on Airway Segmentation

Image segmentation is defined as the process of partitioning an image into different segments [35]. The goal of segmentation is to simplify or change the representation of an image into something that is more meaningful and easier to analyze. In medical imaging, these segments often correspond to different tissue classes, organs or biologically relevant structures. It is one of the first steps leading to medical image analysis, interpretation, and extraction of medical data. The following section contains related literature on the segmentation of the upper (nasal cavity) and lower (trachea and bronchi) airway.

2.4.1 Nasal Cavity

Due to the complexity of the nasal cavity structure as well as the lack of boundary distinction between it and other airway components such as the paranasal sinuses, individual modelling and segmentation was rarely performed. Existing models of the nasal cavity were all manually extracted from a single patient CT scans [24, 41, 42]. The current known methods [43-50] are capable of producing adequate segmentations of the upper respiratory tract consisting of the nasal cavity, paranasal sinuses and the pharynx using relatively simple algorithms such as thresholding [45-48], region growing [43, 44], level-sets [49], and a level-sets distribution model [50]. However, the majority of these methods still require manual delineation [43-46] and/or requires the imaging modality to be taken from cone-beam CT (CBCT) [46-49] which provides higher contrast and reduces the amount of motion artifacts. More importantly, these

methods are restricted by their inability to differentiate and/or separate the nasal cavity from other airway regions components within the upper respiratory tract, thus limiting its application in nasal drug delivery [25], nasal computational fluid dynamics [51], and for the diagnosis and treatment planning of nasal diseases [27].

2.4.2 Trachea and bronchi airway

The majority of the recent segmentation approaches tends to focus on extracting the airway tree structure as deep as possible, and relies on the anatomical details present on of the high-resolution CT image. As shown in the EXACT09 airway segmentation challenge, where more than 15 methods were evaluated, due to the quality of the CT images which can adequately separate the voxels belonging to the airway, simple region-based algorithms such as the conventional *region growing* algorithm was capable of accurately segmenting the trachea structure as well as the main bronchi branches within the airway tree. Region growing relies on checking for similar intensity values between neighboring voxels in order to "grow" until there are no more similar voxels connected to the initial seeds. The majority of the proposed methods from [52] made use of region growing as their primary algorithm for initial segmentation and then combined it with additional algorithms for further refinement into the airway tree. For example, Irving et al [53] made use of morphological filtering to extract smaller branches within the airway tree after their region growing segmentation. Feuerstein et al [54] applied a sharpening filter to enhance the branch edges in order to extend their region growing method to smaller parts of the airway tree. Pechin et al [55] incorporated a combination of a trained appearance model along with vessel and airway orientation information to improve the performance region growing segmentation approach by accurately differentiating between airway and non-airway voxels. Lee and Reeves [56] initiated their region growing method through a tree segmentation framework which applied a locally-defined volume of interest boundary at each intersection of the airway in order to prevent leakages. While these algorithms performed well on high-resolution CT, their reliance on region growing meant that they were subject to lower performance when applied to low-contrast CT. Evidently, when tested on low-contrast CT images, region growing tend to suffer considerably from under- or over-segmentation errors [57].

Other segmentation algorithms designed for high-resolution CT, that are not reliant on region growing algorithms, such as the study from Tan et al [58], made use of *fast marching* methods for initial segmentation, followed by using surface diffusion algorithm as a feedback loop to continuously derive new seed points to further segment the region into the airway branches. Rikxoort et al [59] proposed a multi-*thresholding* framework using wave-front propagation to continuously segment new areas of the

trachea airway. Geng et al [60] segmented the lung airway through a combination of iterative thresholding and pulmonary regions extraction. Shang et al [61] introduced a novel region competition-based *active contour model* algorithm which made use of a vascular vector field to evolve the active contour along its center line for more accurate segmentation. In another study, Xu et al [62] made use of *fuzzy connectivity* for their initial airway approximation, and afterwards, a spatially constrained Markov random walk was applied on the tissue wall surrounding the airway for boundary refinement extend their segmentation into the deeper regions of the airway tree; the constraint was derived from airway wall estimation using FWHM [63] and least square ellipse fitting. Although some of these works presented advanced algorithms that leveraged prior knowledge in terms of prior knowledge from segmented datasets, as with previous region-based algorithms, they were also designed for high-resolution CT and hence were not optimized to tolerate the image characteristics inherent in low-contrast CT.

Attempts at low-contrast CT for airway segmentation have also been introduced; two previous works has been identified. Tschirren et al. [64] made use of fuzzy connectivity as their primary algorithm for segmentation where they assigned a fuzzy membership to each voxel based on the intensity similarity between the input image and two landmarks belonging either to the trachea or the airway wall. Their method allowed the two regions to compete against each other in order to classify airway voxels, and thereby adding tolerance to *fuzzy* voxels near the structure boundaries. Wang et al. [57] made use of anatomical knowledge to predict and derive seeds for their modified region growing method in a slice-by-slice approach. Although these algorithms presented feasibilities in low-contrast airway segmentation, they only made use of the information found within individual CT and did not take advantage of prior knowledge, which can provide more benefits especially for low-contrast CT images where e.g., leakages is a known issue [57, 64].

Chapter 3. Prior Knowledge in Medical Image Segmentation

3.1 Introduction

This chapter aims at presenting the literature in the domain of medical image analysis with emphasis on *image segmentation*. Medical image analysis involves the extraction of meaningful information from medical images. For a more detailed description of medical images, please refer to Chapter Two. Among the many techniques which can be employed for medical image analysis, image segmentation is the most commonly used, and often only as the first step leading to image analysis and interpretation. In computer vision, image segmentation involves the process of partitioning an image into different segments. The goal is to simplify or change the representation of an image into something that is more meaningful. In case of medical images, these segments often correspond to different tissue classes, organs or biologically relevant structures [35].

Due to the vast amount of segmentation algorithms that are available within the medical image analysis literature, this thesis will only cover the details of algorithms that are directly relevant. The criteria selection is based on algorithms which make use of *prior knowledge* to improve upon the segmentation. Prior knowledge is defined in this thesis as spatial and/or anatomical information of the targeted region of interest derived from additional data sources. Algorithms which take advantage of spatial and/or anatomical information can be roughly categorized as *knowledge-based* approaches for medical image analysis.

Chapter Three focuses on the review of current available segmentation algorithms which make use of prior knowledge. Section 3.2 briefly covers algorithms using weak or no prior knowledge as to provide better background information on image segmentation. Section 3.3 introduces image registration with the primary focus on its usage with medical image segmentation. Section 3.4 presents algorithms based on deformable models and its incorporation with statistical concepts. Section 3.5 addresses a separate category of algorithms which utilizes atlases for their prior knowledge segmentation. Section 3.6 covers a list of region-based state-of-the-art segmentation algorithms and their capability at incorporating shape prior knowledge.

3.2 Weak Prior Knowledge Approaches

Algorithms that fall under this category use little or no prior knowledge for image segmentation. These algorithms are often regarded as low-level techniques and are commonly used as a preprocessing step for more complex approaches due to the simplicity in their parameterization. The two types of algorithms presented in section 3.2 are *thresholding* and *region growing*.

3.2.1 Thresholding

Thresholding is one of the most basic algorithms which can be used to segment an image. When given any scalar (greyscale intensity eg., CT pixel value) or multi-dimensional (color value eg., RGB or LAB) image, the thresholding algorithm separates the pixels in the image into either foreground or background based on comparing the pixel value against the user specified parameter (threshold). If the pixel value is above the specified threshold then it is assigned as a part of the foreground, if it is below the threshold then it becomes a part of the background.

Thresholding algorithms can be categorized into either global or local approaches [65]. Global approaches tend to be more simplistic where the same threshold value is used for the entire image, while local approaches varies the threshold based on additional information such as using spatial knowledge. Global approaches such as Otsu Thresholding [66] and Isodata Thresholding [67] focuses their algorithm on automatically deriving the most optimal threshold value based on additional analysis such as based on the *histogram* of the image. A histogram is a graphical representation of the intensity distribution in an image. However, these algorithms are still relatively simple and cannot be used to segment specific areas within an image.

To overcome some of the shortcomings of global approaches, local thresholding algorithms were designed to be able to flexible when segmenting an image, and can vary its threshold value depending on the location within the image. Examples of local thresholding algorithms can be read from the works of Niblack [68], Mardia and Hainsworth [69], and Oh and Lindquist [70]. More advanced thresholding approaches are unsupervised and tend to rely on some basic prior knowledge, such as the number of classes, and are often the result of analysis on the histogram of the image. [71] contains additional details on the formulation of these approaches.

Generally, for images presenting little noise and strong contrast between structures to segment, where clear boundaries can be distinguished between the foreground and background, thresholding algorithms

can be a simple yet effective approach. However, thresholding algorithms tend to exhibit very poor performances when in the presence of moderate noise and/or artefacts, which are often encountered in medical images. Overall, within the medical image processing literature, thresholding tend to be used as part of a preprocessing step for more advanced algorithms.

3.2.2 Region Growing

Region growing is another relatively simple image segmentation approach that has been widely used since its creation. The region growing algorithms segment an image via classifying pixels of with similar characteristics into the same region. This is achieved through an iterative process where given an initial starting pixel, the algorithm searches its pixel neighbors to look for pixels of similar characteristic (such as intensity value) and add them to the foreground region. The algorithm continues to expand or "grow" until it can no longer locate additional pixels of similar characteristics.

Region growing approaches typically begins from selecting foreground voxels labeled as *seeds*. By exploring the neighbors of these seeds, new potential voxels are added to the foreground region. The seeds required to start the algorithm can be either manually given by an operator or automatically derived using other algorithms such as thresholding based on known intensity values. A number of variations of region growing segmentation method exist in literature such as adaptive region growing [72], seeded region growing [73], unseeded region growing [74]. For more information on region growing, the following survey is recommended for reading [75].

3.3 Registration

Image registration is a frequently used technique in medical image processing. The goal is to identify the spatial relationship between two or more images. Although image registration is not a segmentation algorithm by itself, it can be used for segmentation, however it is more often used together or as a preprocessing step for other image segmentation algorithms. The aim of this section is not to provide a comprehensive review but to present the necessary information on the concept of registration and its usage in medical image segmentation. Section 3.3.1 introduces the transformation parameters used for registration. Section 3.3.2 presents the similarity metrics used for medical images. The following publications may be of interest for those wishing to obtain a more comprehensive knowledge on registration [76-78].

Registration can be generalized as the process of establishing spatial correspondences between two or more images. More specifically, it is the process of finding the transformation that maps one image to another. During registration, one image, which is called the *moving image*, is deformed or shifted to fit the other image, the *fixed image*. Registration attempts to solve the problem of finding a coordinate transformation which can allow the moving image to be spatially aligned to the fixed image. The quality of the alignment is dependent on the similarities between the two images as well as the appropriateness of the chosen similarity metric.

The steps involved during registration rely on the following components: registration features; transform and associated regularization; similarity metric; optimization and interpolation. Figure 3.3.1 gives an overview of the registration process. In an iterative manner, the similarity between the reference and target features is first computed. Target features are computed based on the target image and the chosen transform parameters. Since images are discretized signals, an interpolation is necessary to estimate the target features. Given the computed similarity value and the optimization strategies, new values of the transformation are computed and the procedure repeats. The optimization process usually will iterate until it considers that the similarity has reached an extremum.

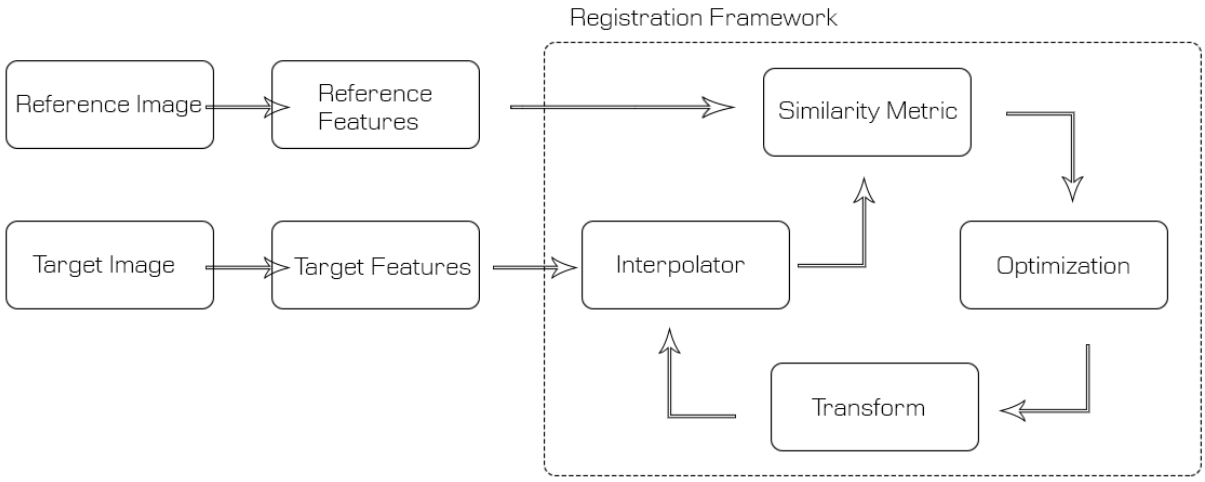

Figure 3.3.1 Overview of registration framework.

3.3.1 Transform and Regularization

For registration, different types of transformations are available. Based on the selected transformation type, the results of registration might differ considerably. They are commonly categorized based on their ability to capture global or local changes. Local transforms are also often referred to as non-rigid types.

Transforms are also characterized by the amount of *degrees of freedom* (DOF); the number of independent transformation parameters. The more DOFs a transform has, the more complex changes it can express. A list of well-known registration transformations can be viewed in Table 3.3.1.1, categorized as either global or local.

Rigid and similarity are two of the most commonly seen transformation types of the global category. They are also known as linear transforms as they cannot model local geometric differences between images. Affine transform characterized by translation, rotation, scaling and shearing is a first crude approximation of a non-rigid transformation [76]. Polynomial transform is another attempt at approximating a non-rigid transformation while providing better control over the DOF [79].

Non-rigid approaches focuses more on local features with attempt to model more accurately the amount of deformations by increasing the DOF. Piece-wise affine transform was proposed with the intention to allow for a tradeoff between DOF and non-rigidity. It works by splitting the reference and target images into pieces and to compute the best affine transform to match each of the pieces. Spline-based registration algorithms use corresponding ‘‘control’’ points, in the source and target image and a spline function to define correspondences away from these points [80]. Each control point belonging to a thin-plate spline has a global influence on the transformation in that, if its position is perturbed, all other points in the transformed image change. This can be a disadvantage because it limits the ability to model complex and localized deformations and because, as the number of control points increases, the computational cost associated with moving a single point rises steeply. By contrast, B-splines are only defined in the vicinity of each control point; perturbing the position of one control point only affects the transformation in the neighborhood of the point. Because of this property, B-splines are often referred to as having ‘‘local support’’. B-spline based non-rigid registration techniques are popular due to their general applicability, transparency and computational efficiency [81].

Transformation Type	DOF	Global	Remarks
Rigid	6	Yes	Intra-patient, rigid structures
Similarity	7	Yes	Intra-patient, different scales
Affine	12	Yes	Coarse approximation of non-rigid transform
Polynomial	$3\sum_{i=1}^{d} C_{i+2}^{0}$	Yes	*d* = polynomial order, non-rigid approximation

Piece-wise affine	12*N*	No	Non-rigid, *N* = number of pieces
FFD (bspline)	$3N_xN_yN_z$	No	Non-rigid, $N_xN_yN_z$ = grid size
Deformation maps	3*N*	No	*N* = number of deformation vectors

Table 3.3.1.1. Common 3D registration transforms.

3.3.2 Similarity Metrics

Similarity metrics express the quality of matching between reference and target features. They are a key component of the registration process as the optimization tries to minimize them. A number of similarity metrics exist for different image types. The commonly seen metrics are listed in table 3.3.2.1, which can be categorized based on the types of image features to be registered. For biomedical images, *Mutual Information* (MI) [82] is one of the most used metrics, which is based on the concepts of information theory where MI minimizes the joint density of the gray value distribution by using kernel density estimation techniques. In order to make MI less sensitive to the overlap of the reference and the transformed image, normalized MI (NMI) [83] was proposed, which encountered great success [84-86].

Similarity Metric	Metric Type
Sum of square differences (SSD)	Intensity conservation
Cross correlation (CC)	Intensity conservation
Normalized cross correlation (NCC)	Intensity conservation
Normalized gradient flow (NGF)	Intensity changes conservation
Correlation ration (CR)	Functional relationship in image intensity
Bivariate correlation ration (BCR)	Functional relationship in image intensity
Mutual information (MI)	Functional relationship in image intensity
Normalized mutual information (NMI)	Functional relationship in image intensity

Table 3.3.2.1. List of common similarity metrics and their metric type.

3.4 Atlas-based Approaches

Atlas-based approaches are a type of image segmentation method which make use of a known template or pre-defined shape of the targeted anatomy as a reference frame for segmentation. Compared to other methods, atlas-based approaches make use of prior knowledge gained from the pre-defined template(s)

and can segment an image without regard to regions or voxel intensity. The template(s) used for segmentation are referred to as atlases, hence the name atlas-based approaches. An atlas is generated by compiling information on the anatomy that requires segmenting, usually each atlas comes in pairs, composed of two parts; the atlas image and a segmentation label. The atlas-guided approaches essentially treats segmentation as a registration problem. The simplest approach involves registering a single atlas image to the target image, and then applying the transformation map to the segmentation label to warp it to the same reference frame as the registered atlas image. The transformed segmentation label should now overlap with the targeted anatomy for segmentation. More advanced methods of atlas-guided approaches utilizes multiple atlases incorporating statistics as well as additional methods for segmentation. This section primarily introduces the core concepts of atlas-guided approaches for segmentation and registration which will be used as part of the methods included for respiratory airway modelling and segmentation in the later chapters.

3.4.1 Multi-atlas

Multi-atlas segmentation (MAS) was first introduced and popularized in the works of Rohlfing et al. [87] and Klein et al. [88] where multiple atlases were combined together to segment anatomical structures. MAS in its simplest implementation is essentially merging individual atlases together on the same reference frame to gain a general idea of where the target structure lies based on the region of overlap. MAS has become much more sophisticated over the years through the combination with other algorithms employing ideas from other fields such as machine learning, probabilistic modelling, optimization, and computer vision. For a more in-depth review of multi-atlas segmentation algorithms in biomedical images, refer to [89].

3.4.2 Probabilistic atlas

Probabilistic atlas segmentation (PAS) appeared around the same time as MAS where statistics about the labels, such as the probability of observing a particular label at a given location, are precomputed in atlas space. The novel image is then segmented in the atlas coordinate frame with a probabilistic inference procedure that utilized parametric statistical models. The spatial normalization to the atlas could be computed via registration with a population template created at training, or estimated jointly with the segmentation within the probabilistic model; the latter alternative has the advantage that it is adaptive to variations in image intensity profiles, such as MRI contrast [90].

Probabilistic atlas-based segmentation offers two major advantages. First, by employing a single coordinate frame, to which all images are normalized, one automatically established spatial correspondence across all images. This facilitates the statistical analysis of biological variation across the population. The second advantage is in the computational cost. One only need to run the computationally expensive image registration step (spatial normalization) only once per novel image [89].

3.5 Deformable Models

Deformable models covers a broad range of segmentation algorithms which performs image segmentation through the evolution or deformation of some form of model. In medical image processing, deformable model approaches tend to segment the targeted anatomical structure through overlaying a model in the same spatial coordinates (usually via registration), and evolve the model into the same structure as the targeted anatomy. The model used for segmentation can be represented using different methods. Types of deformable model segmentation approaches can be categorized based on the type of representation used for the model.

The two main representations are continuous and discrete. In discrete representation, less information is typically used to denote the shape of the anatomy. This is usually done using a set of points. The points (co-ordinates) used to represent the shape are usually spread evenly around the anatomy and should capture the important features of the anatomy. The surface of the shape can then be represented using meshes such as triangular or simplex meshes, which fills in the gap left behind by the set of points. Using less points to represent a shape can allow for more complex representation of shapes with higher arbitrary topology while remaining computationally inexpensive.

Continuous representation yields more accurate details of the shape at a cost of requiring higher computational requirements. Continuous representations commonly rely on some form of *parameterization* which limits the amount of freedom on the variation of shape topology. For instance, spherical harmonics could only describe shape topologies equivalent to a sphere. However, the amount of parameterization needed for shape representation varies based on the selected approach. In general, parameterization restrictions are adequate for the segmentation of structures with a relatively simple geometry, though they might not be as suitable for more complex shapes. However, the advantages of continuous approaches is that they are more robust to image artefacts and missing information whereas discrete approaches tend to perform poorly due to their reliance on image information.

Continuous Representation	
Explicit	*Implicit*
Snakes Spherical Harmonics	Level-sets Medial
Discrete Representation	
Meshes	*Particle Systems*
Triangular meshes Simplex meshes	Point Cloud

Table 3.5.1. List of different representation types for shape.

This section covers the three commonly used methods of representation. Section 2.5.1 introduces the explicit representation active contour snakes. Section 2.5.2 focuses on the implicit representation using level-sets. Section 2.5.3 traverses through the discrete representation of deformable model approaches. Section 2.5.4 introduces the correspondence issue that affects deformable model approaches.

3.5.1 Snakes

One of the earliest deformable model approaches dates back to Kass et al.'s *Active Contours Model*, popularly known as *Snakes*. It introduced the idea that model evolution can be driven by two main energies. Given a 2D image domain Ω, snakes are parametric curves $C: [0,1] \to \Omega$ driven by the minimization of an energy function:

$$E(C) = \frac{\alpha}{2}\int_0^1 |C'(q)|^2 dq + \frac{\beta}{2}\int_0^1 |C''(q)|^2 dq + \gamma \int_0^1 |f(C(q))| dq \qquad (3.5.1.1)$$

The first two integrals denote the internal energy which enforces model smoothness based on Tikhonov stabilizers of the 2nd order. The last integral expresses the external energy which attracts the contour towards the boundaries of the structures to segment. In its simplest form, snakes are attracted by edges with higher gradient magnitude, i.e. $f(x) = \|\nabla I(x)\|$. Coefficients α, β and γ weight the stretching, bending and image attraction of the snake. Natural extensions to the 3D case were proposed by [91] based on the first and second order derivatives.

Based on the principle of variation, the snake evolution follows the Euler Lagrange equation: $\nabla E(C) = 0$. To solve this equation, an artificial time variable t is introduced and the snake $C(q)$ is thus made dynamic:

$$\frac{\partial}{\partial t}C(t,q) = \alpha C''(t,q) - \beta C''''(t,q) + \gamma \nabla f(C(t,q)) \qquad (3.5.1.2)$$

This equation can be efficiently solved with finite differences discretization and the iterative solving of the discrete system. This minimization is local and the snake will thus converge to a local minimum.

The main weaknesses of snakes include its necessity to be initialized closely enough to the boundary of the targeted anatomy, its inability to move into concavities of the boundaries, and its fixed topology. The first shortcoming was partially addressed by Cohen [92] through the introduction of "balloon" forces which pushed the snake to inflate or delate in the normal direction. The main issue with this force was the need of a priori knowledge on whether an inflation or deflation was required, which prevented the initialization of the snake across the boundaries of the anatomy. The use of gradient vector flow fields [93] to model the external energy resulted in an increase of the snake capture range and a better delineation of concavities. Davatzikos and Prince [94] proposed the use of constraint points to better capture concavities in case of the brain cortex. The support of topological changes was included in the "T-Snakes" of McInerney and Terzopoukos [95]. Chan and Vese [96] further introduced the concept of snakes without edges, which has now been popularly referred to as the Chan-Vese segmentation approach. For more details regarding active contour models and its applications on image segmentation, it can be obtained from the following surveys [97, 98].

3.5.2 Level-sets

Level-sets were first introduced by Osher and Sethian [99], featuring an implicit shape representation and could be employed with regional or edge-based features. The level-sets shape model is embedded in a higher dimensional space, such that for a level-set S, an iso-hypersurface of a function $\phi: \Omega \rightarrow \mathbb{R}, \Omega \in \mathbb{R}^d$ can be represented through:

$$S = \{x \in \Omega | \phi(x) = c\} \tag{3.5.2.1}$$

Where c is a constant usually equal to zero. When $d = 2$ or $d = 3$ the level-set S is an iso-contour or an iso-surface. The level-set S is also seen as the boundary ∂R which enclose a region R:

$$s = \partial R \tag{3.5.2.2}$$

$$R = \{x \in \Omega | \phi(x) < c\}$$

This formulation allows an implicit definition of the deformable model with ϕ. By evolving the function ϕ, the deformable model represented by S becomes implicitly modified. The greatest advantage with respect to using level-sets for deformable modelling is that S can naturally undergo topological changes

as it can split and/or merge into various iso-hypersurfaces during its evolution [100]. The common way to define the function ϕ is to use the zero level-set, the signed distance function (SDF) for the representation of the deformable model. Given a point $x \in \Omega$, $SDF(x)$ is the signed Euclidean distance between x and its closest point on the deformable model. A negative sign is arbitrarily chosen, e.g. $SDF(x) < 0$ when $x \in R$ given equation (3.5.2.1). Figure 3.5.2.1 illustrates the usage of SDF to implicitly define a nasal structure.

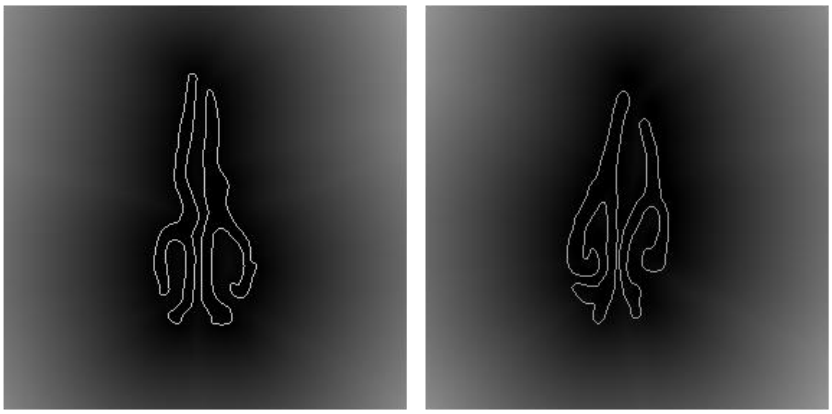

Figure 3.5.2.1. Implicit deformable model representation of 2D slices of the nasal cavity computed using SDF.

The level-set approach for deformable models was first introduced to medical image segmentation by Malladi et al. [101], where a time parameter t was applied to the level-sets equation to evolve the SDF overtime similar to that of snakes:

$$\frac{\partial}{\partial t}\,\phi + \vec{v}.\nabla\phi = 0 \qquad (3.5.2.3)$$

where $\vec{v}$ is the external force field driving the evolution towards the correct image location. This field is computed based on image information such as the image gradient magnitude. This formulation requires the need to solve partial differential equations (PDE). Caseslles et al. [102] combined the snake-based evolution with the level-sets formulation into a new method called *geodesic active contours* (GAC). In addition to the possible topology changes, GAC brings several advantages with respect to the classic snakes implementation. First, there is no need for re-parameterization during evolution. Second, the function ϕ is independent from the contour parametrization which means that the deformation are only dependent on the shape of the deformable model.

Although GAC have solved the problem of re-parametrization during the level-set evolution, it could not solve the issue of experiencing irregularities within the level-set function (LSF) during the evolution. The

original remedy to this issue was proposed by Weber et al. [103] through the re-initialization of the LSF, and to periodically replace the degraded LSF with a SDF. However, this approach causes extra computational burden and required additional time in order for the algorithm to complete the level-set evolution. An alternative solution to this issue was proposed by Li et al. [104] through adding an additional energy term called the Distance Regularization Term to the level-set equation. The distance regularization term is defined with a potential function such that the derived level-set evolution (LSE) has a unique forward-and-backward (FAB) diffusion effect which is able to maintain a desired shape of the LSF. This yields a new type of level-set evolution which the paper named it as the Distance Regularized Level-Set Evolution (DRLSE). The Distance Regularization effect is able to ultimately eliminate the need for re-initialization.

While there are many advantages to using level-sets for deformable models, disadvantages also exist. In cases where the topology of the anatomical structure is known in advance, the ability of the level-set to adopt topological changes can become an issue. The other main problem in using level-sets is the computational burden, especially in 3D. Using level-sets for shape representation can be extremely memory inefficient [105]. For further reviews on level-sets, the following papers are recommended for reading [105-107].

3.5.3 Discrete Deformable Models

Discrete deformable models are characterized by a series of points representing the boundaries of the shape model. When an explicit connectivity is established between the points, the discrete deformable models are referred to as meshes. Figure 3.5.3.1 illustrates various possible representations for a nasal cavity shape.

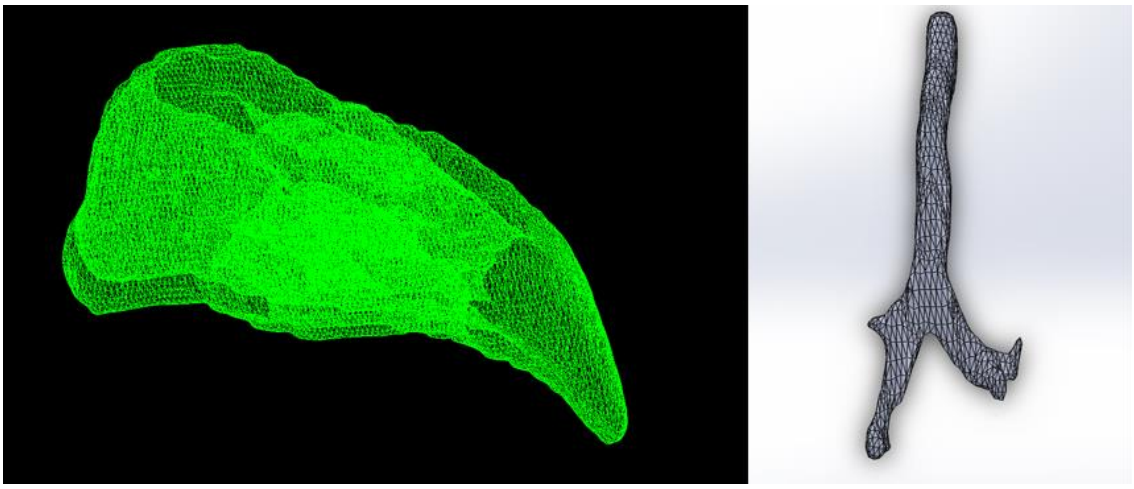

Figure 3.5.3.1 Examples of explicit discrete deformable model representation. The nasal cavity shape (left) is represented using 3D geometry, the trachea airway (right) is represented using triangular mesh.

More formally, a discrete model S can be represented in a d-dimensional space as a triplet $S = \{X, N, G\}$, where $X = \{x_1, \dots, x_M\}$ is the point set composed of M points $x_i \in \mathbb{R}^d$, $N = \{n_1, \dots, n_M\}$ is the optional normal set, one normal per point, and G is the connectivity information which specifies the point indices of using edges and the edges of faces. G is only defined for meshes. Normals can be defined from the point set X using only point-based techniques such as Oriented Particles [108], Moving Least Squares (MLS) [109], and Implicit Surface [110], or in conjunction with the connectivity information G based on neighbours positions [111].

For discrete deformable models, meshes are the most popular method of shape model establishment. The most commonly seen type is Triangular Meshes, which are two dimensional manifolds characterized by triangular faces. In the field of computer graphics, triangular meshes are natively supported by the graphics hardware. In the domain of image segmentation, they are often the preferred choice for combining with discrete points for the representation of shapes due to their superior ability at capturing the arbitrary topology and complexity of shapes.

Miller et al. [111] proposed their geometrical deformable models that evolved under external and internal constraints. Local curvature was estimated from the neighbours of a vertex. The evolution was carried out with an algorithm that moved vertices in the direction of steepest descent along the cost surface computed from the external and internal constraints. Local curvature was estimated from the neighbours of a vertex. The evolution was carried out with an algorithm that moved vertices in the direction of steepest descent along the cost surface computed from the external and internal constraints. Lachaud and Montanvert [112] designed a coarse-to-fine segmentation approach using triangular meshes which

was able to undergo topological changes via Eulerian topological transformation of creation, deletion or inversion. Snel et al. [113] used multi-resolution deformable triangular meshes to segment carpal bones in MRI images based on Lagrangian mechanics. More recently, Willimon et al. [114] introduced an automatic mesh generator that provides a triangular mesh encapsulating the entire non-rigid object without pre-defined values or feature correspondence.

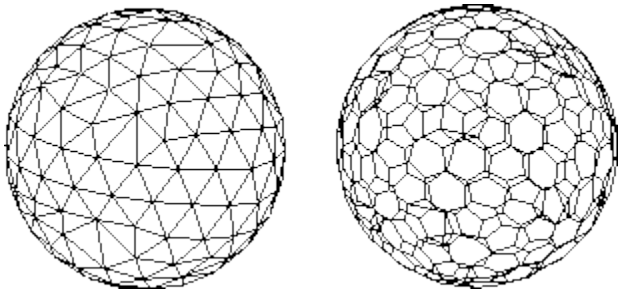

Figure 3.5.3.1 Illustration of a triangular mesh (left) and a 2-simplex mesh (right)

Another popularly used mesh type is Delingette's simplex meshes [115]. The algorithm is able to reconstruct surfaces with minimal restriction on their shape or topology. k-simplex meshes are discrete models with a constant vertex connectivity of $k + 1$ neighbours. Figure 3.5.3.1 shows an example of the structure of a 2-simplex mesh used to represent surfaces when compared against triangular mesh. Each vertex of a 2-simplex mesh is connected to three neighbours. 2-simplex meshes are topologically dual to triangulations, meaning there exists a dual triangle for each mesh vertex and a dual triangulation vertex for each mesh face. Due to their constant connectivity, the geometry of simplex meshes is rather simple. A notion of surface local shape description allows the definition of shape memory constraints in the deformation process.

Many works have adapted simplex meshes for deformable models. These include segmentation works by Gilles et al. [116, 117] on the musculoskeletal structures from MRI. Schmid et al. [118] made use of 2-simplex meshes for their statistical shape model (a more complex type of deformable model) for MRI bone segmentation in presence of small field of view. A review on the types of discrete representation for deformable models can be found in [100].

3.6 Statistical Shape Models (Knowledge-based Deformable Models)

Deformable models which incorporate statistical prior knowledge derived from probabilistic analysis from within a distribution of a class of shape objects are often referred to as *Statistical Shape Models* (SSM). SSMs are commonly applied for computing accurate 3D representations of a targeted anatomy. Based on

a set of training data, the variability of the class of training data is modelled by means of a normal distribution, and SSM can then formulate statistical averages and variations, as well as reconstruct patient specific anatomical representations through combining the statistical priors with the observed data. SSMs have been employed in many applications due to its wide range of capabilities such as in object recognition [36], image manipulation [37], surgery planning [38] as well as segmentation [39, 107, 119]. However, this thesis will focus primarily on the aspect of SSM modelling and segmentation.

SSMs can be categorized in the same way as deformable models where it is primarily split between discrete and continuous representation for shape. Discrete methods of SSM creation and utilization are commonly referred to as *Point Distribution Models* (PDM) while continuous methods are commonly referred to as *level-set distribution models* (LSDM) within the medical image analysis literature. Section 2.6.1 introduces more specific details of PDM as well as their advantages and disadvantages. Section 2.6.2 covers the details of LSDM and recent works related to its use in medical images.

3.6.1 Point Distribution Models

The earliest well known shape model that incorporated statistical means as part of its variance distribution belongs to Cootes et al.'s [120] *Active Shape Model* (ASM) which made use of a set of discrete "landmark" points to represent their shape (popularly referred to PDMs). A landmark is a point of correspondence used to examine and measure shape change [121]. This method has since become inaugurated as the conventional approach to building SSMs. Typical steps involve the use of a set of points distributed across the surface of the targeted shape (which can be extracted into a single vector space using algorithms such as *Marching Cubes* [122]) for representation, to which once successfully aligned and gathered into a common space frame, principal component analysis (PCA) is then deployed to extract the mean shape and a number of modes of variations from the collection of points used during representation [119].

While landmark approaches have become the conventional method for building shape models, a key issue that needs to be addressed is correspondence. When measuring shape variance of a certain part of an object across a population, it is important to compare the same features. If two training shapes are misaligned, the resulting PCA will not be capturing the appropriate anatomical shape variance. This holds especially true for landmark-based approaches where the targeted shape is usually represented by only a small handful of points where each landmark point needs to directly correlate across all training data through precise point correspondence, which previously required the manual labelling of points across all

training data as a means of achieving accurate point correspondence, a feat which is tedious and difficult to achieve especially for complex 3D objects such as the nasal cavity.

Although pioneering works such as Davies et al. [123] and Wang et al. [124] provided the means for achieving automatic landmark correspondences through methods such as *Minimum Description Length* (MDL, global method) and *Landmark Sliding* (pairwise method), they have shown to be inefficient when the population size is large, or they tend to be less accurate and can produce poor shape correspondence when the population has a large amount of shape variations [125]. While recent works such as Munsell et al. [126] aimed at improving the quality of automatic correspondence methods through the introduction of a shape tree for pre-organising shape instances, the effectiveness of these methods have yet to be fully evaluated against large volumes of training data with complex shape variations.

3.6.2 Level-set Distribution Models

Level sets were first introduced by Osher and Sethian [99], featuring an implicit shape representation and can be employed with regional or edge-based features. Leventon et al. [107] further extended the original energy formulation by adding an additional term which deforms the contour towards a previously learned shape model and demonstrated its usage in SSM literature. The advantage of using level-sets is that one can perform numerical computations involving curves and surfaces on a fixed Cartesian grid without having to parameterize these objects. The use of signed distance function as the representation of shape prevents solving the general correspondence problem due to its tolerance to slight misalignment of object features. By coarsely aligning the training data (typically binary segmentations) using techniques such as rigid registration prior to shape representation (via SDF), the entire correspondence issue can potentially be bypassed [127]. However, this approach requires a considerably higher dimensional space for PCA computation due to the choice of using *signed distance maps* (data created using SDF) for representation over distinctive landmark points. The size of the resulting covariance matrix is typically twofold the number of pixels of each training image, which makes the level set approach to be less practical for implementation on 3D training data. Nevertheless, this problem of needing high computational space requirement is gradually being solved by the advancement of modern day computer hardware. This is evident with a number of recent publications such as Wimmer et al. [128] which employed parametric representations of densities to their level set-based active shape model in order to boost classifiers to analyse appearance information. More recently, Tomoshige Sho, et al. [129] integrated an error model into their conditional level set based SSM which estimated the reliability of the observed conditional features and subsequently relaxes the conditional statistical shape model accordingly.

Level set SSM was also implemented in the work of Last et al. [39, 50] where they adapted their SSM to obtain locally optimal solutions by allowing a unique fit of the corresponding SSM in each contour point in order to overcome the issue of having limited training samples. Their locally deformable SSM was used to segment the paranasal sinuses, which are air-filled spaces located within the bones of the skull and face surrounding the nasal cavity structure. Their focus was on a rough structure of the entire paranasal sinus region which encompasses the nasal cavity, as exemplified in figure 3.6.2.1, and thus not needing to model the complexities present in the nasal cavities. These complexities demand an SSM that is capable of capturing thin and curvy structures with high degrees of variation across a population.

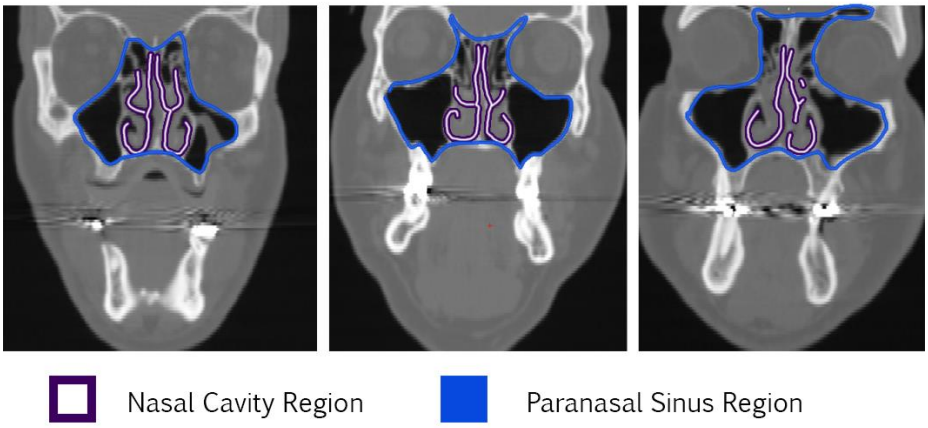

Figure 3.6.2.1 Illustration indicating differences between Last el al. (2011)'s work and the nasal cavity region.

3.7 Incorporating Prior Knowledge to Existing Algorithms

Knowledge derived from statistical shape models can be incorporated into many existing segmentation algorithms. In the medical image analysis literature, detailed knowledge of the targeted anatomy can often greatly improve the results of segmentation. The current state-of-the-art region-based segmentation algorithms include Graph Cut [130], Random Walks [131], and Geodesic methods [132]. These methods basically treat an image as a weighted graph with nodes corresponding to pixels in the image and edges being placed between neighboring pixels, and minimize a certain energy function on this graph to produce a segmentation. A shared benefit of region-based segmentation algorithms is their compatibility with the SSM of continuous representation, where SSM results derived from PCA can be incorporated to restrict and/or influence the outcome of segmentation. Section 3.7.1 presents the incorporation of level-set SSM with Geodesic methods. Section 3.7.2 introduces Graph-Cut LSDM. Section 3.7.3 focuses on adapting level-set SSM with Random Walks.

3.7.1 Geodesic Methods

Geodesic methods are essentially level-set based segmentations which involves solving the energy-based active contours minimization problem. Level-set based segmentation approaches have existed within the image processing field for a long time now. Generally, a classical level-set framework consists of an implicit data representation of a hypersurface, a set of partial differential equations (PDE) that govern how the curve moves, and the corresponding numerical solution for implementing this method. Geodesic level-set methods have since evolved over time through the additions of newer energy terms and functions as mentioned previously in Section 3.5.2.

Statistical knowledge gained via PCA on training datasets represented in the form of SDM can be incorporated into geodesic level-set PDEs as an additional energy term which is capable of constraining the LSF to valid anatomical shapes of the targeted anatomy as the LSF evolves over time. Given an energy function $E(\varepsilon)$ over a contour ε as the sum of an internal and external energy, the function to evolve the shape contour to minimize the energy is as follows:

$$E(C) = \frac{\alpha}{2}\int_0^1 |C'(q)|^2 dq + \frac{\beta}{2}\int_0^1 |C''(q)|^2 dq + \gamma \int_0^1 |f(C(q))| dq \quad (3.7.1.1)$$

The minimization problem can then be reduced to the following form:

$$min \int g(|\nabla I(\varepsilon(q))|)\, |\varepsilon'(q)| dq \quad (3.7.1.2)$$

where g is a function of the image gradient in the form of $\frac{1}{1+|\nabla I||^2}$ with I being the input image. Using Euler-Lagrange, the following shape evolution equation can be derived:

$$\frac{\partial \varepsilon(t)}{\partial t} = gkN - (\nabla g . N)N \quad (3.7.1.3)$$

where k is the shape and N is the unit normal. By defining an embedding function u of the contour ε, the equation for a higher dimensional SDM surface u can be computed.

$$\frac{\partial u}{\partial t} = g(c + k)|\nabla u| + \nabla u . \nabla g \quad (3.7.1.4)$$

Where c is an image-dependent balloon force which stabilizes the contour to flow outward [92]. In this LSF function, the surface u evolves at every point perpendicular to the level-sets as a function of the curvature at that point and the image gradient. Given the contour at time t, an evolution step that brings the contour closer to the final anatomical shape based on the local gradient and global shape information

is computed. Equation 3.7.1.4 provides the means of evolving the initial surface shape u over time towards the solution to the original minimization problem stated in Equation 3.7.1.2. The surface of the SDM at time $t+1$ can be computed from $u(t)$ by:

$$u(t+1) = u(t) + \lambda_1(g(c+k)|\nabla u(t)| + \nabla u(t).\nabla g \quad (3.7.1.5)$$

where λ_1 is a parameter defining the update step size. By estimating the final surface u^* at a given time t, the contour can be evolved in the direction of the maximum *a posteriori* final surface:

$$u(t+1) = u(t) + \lambda_2(u^*(t) - u(t)) \quad (3.7.1.6)$$

where $\lambda_2 \in [0,1]$ is the linear coefficient that determines the amount of influence the maximum a posteriori take effect during LSE. Combining these equations yields the following expression:

$$u(t+1) = u(t) + \lambda_1(g(c+k)|\nabla u(t)| + \nabla u(t).\nabla g) + \lambda_2(u^*(t) - u(t)) \quad (3.7.1.7)$$

Many recent works have modified or updated equation 2.7.6 through the introduction of new energy terms such as seen in Li et al. [106] where a distance regularized term was proposed to remove the need for re-initialization. Wang et al. [133] improved on the current Chan-Vese level-set methods through binding the shape energy and local intensity feature to evolve the surface both globally and locally towards the closet shape driven by the PCA, for their liver segmentation algorithm. Qin et al. [134] modified their geodesic level-set methods with an adaptive shape prior to constrain the direction of the LSE for bladder MR image segmentation.

3.7.2 Graph-Cuts

Graph Cuts segmentation was originally proposed by Boykov and Jolly [130] where given some foreground and background seeds, an energy function based on both boundary and region information can be minimized to result in a segmentation. The goal is essentially to find a set of labels $A = (A_1, A_2, \dots, A_p, \dots, A_{|P|})$ that minimizes an energy function $E(A)$ given by:

$$E(A) = \lambda R(A) + B(A) = \lambda \sum_{p \in P} R_p(A_p) + \sum_{\{p,q\} \in Np} B_{p,q}\delta_{Ap \neq Aq} \quad (3.7.2.1)$$

where the set P is a set of pixels or voxels in a 2D or 3D image, and the energy $R_p(A_p)$ is a matching cost of a graph, assigning label $A_p \in L$ to p. The symbol A_p is an element of label set $L = (1,0)$; with 1 being the foreground and 0 being the background. This cost is defined by a negative log probability of the intensity values from the CT image, where the probability density function of each class is assumed to be

a normal distribution with parameters estimated by an EM algorithm. The set Np is a set of voxels in the 6-neighborhood of p, and the function δ is 1 if $Ap \neq Aq$ and 0 otherwise. The energy $B_{p,q}$ is a n-link cost of labeling the pair p and q with labels $Ap \neq Aq \in L$. The coefficient λ is a constant value balancing the two costs. Detailed explanation of each energy term can be found in [130].

3.7.3 Random Walk

Random Walk is another region-based segmentation algorithm which treats an image as a graph and solves an energy minimizing problem in order to obtain a segmentation [131]. Given an input image, a graph consisting of $G = (V, E)$ with nodes $v \in V$ and edges $e \in E$ can be derived. For 3D images, 26-connected lattice was used for the construction of V and E. An edge e, spanning two nodes v_i and v_j, is denoted by e_{ij}. A weight is assigned to each edge in order to provide better path finding. The weight of an edge e_{ij} is denoted by w_{ij} and is given as:

$$w_{ij} = \exp(-\beta(g_i - g_j)^2) \tag{3.7.3.1}$$

where g_i indicates the image intensity at voxel i. The value of β is a changeable parameter value which controls the edge weight w_{ij}, where large values of β restricts the random walks from crossing edges more easily. The degree of a node is $d_i = \Sigma w_{ij}$ for all edges e_{ij} incident on v_i. An input image is associated with a graph by identifying each voxel with a node and defining edges being the connection between voxels to its neighbors.

The random walks segmentation algorithm computes the probability for each voxel x that a random walk leaving that voxel will first arrive at a foreground seed before arriving at a background seed. These probabilities can be calculated analytically by solving the Dirichlet problem with the boundary conditions given by seed locations. A Dirichlet integral is defined as:

$$D[U] = \frac{1}{2}\int_{\Omega} |\nabla U|^2 \, d\Omega \tag{3.7.3.2}$$

for a field u and a region Ω. A solution can then be obtained through solving a harmonic function that satisfies the Laplace equation:

$$\nabla^2 U = 0. \tag{3.7.3.3}$$

The Laplacian matrix can be defined as:

$$L(i,j) = \begin{cases} d_i & \text{if } i = j, \\ -w_{ij} & \text{if } v_i \text{ and } v_i \text{ are adjacent nodes,} \\ 0 & \text{otherwise,} \end{cases} \quad (3.7.3.4)$$

where $L(i,j)$ is indexed by nodes v_i and v_j.

Given a set of foreground seeds V_F and background seeds V_B, where $V_F \cap V_B = \emptyset, V_S = V_F \cup V_B$. We can compute the probabilities x_i that a random walk leaving node v_i arrives at a node in V_F before arriving at a node V_B by solving:

$$L_U x_U = -B x_S. \quad (3.7.3.5)$$

The variable x_U represent the set of probabilities corresponding to unseeded nodes. x_S is the set of probabilities corresponding to seeded nodes (i.e., 1 for foreground and 0 for background nodes). L_U and B correspond to the matrix decomposition of L

$$L = \begin{bmatrix} L_S & B \\ B^T & L_U \end{bmatrix} \quad (3.7.3.6)$$

Using the probability obtained by solving (3.7.3.5), each voxel in the image is then assigned to its corresponding label for which it has the highest likelihood of being (either as part of the foreground or background). As such, the Dirichlet integral for the random walk energy is formulated as follows:

$$E_{rw} = \frac{1}{2} x^T L x \quad (3.7.3.7)$$

As each node in the random walk algorithm is labeled as either foreground for background, the probability matrix for the entire graph can be formulated as $x = \begin{bmatrix} x_S \\ x_U \end{bmatrix}$. Hence (3.7.3.7) can be decomposed as:

$$E_{rw}[x_U] = \frac{1}{2} \begin{bmatrix} x_S^T & x_U^T \end{bmatrix} \begin{bmatrix} L_S & B \\ B^T & L_U \end{bmatrix} \begin{bmatrix} x_S \\ x_U \end{bmatrix} \quad (3.7.3.8)$$

The solution of the unlabeled probabilities can be obtained by differentiating (3.7.3.8) with respect to x_U.

Random Walk with Shape Priors

Assuming there is a set of real-valued, nodewise priors λ_i^s that represent the probability density that the intensity at node v_i belongs to the intensity distribution of a predicted label (shape) g^s. Baye's theorem gives the probability that a node v_i belongs to g^s as:

$$x_i^s = \frac{\lambda_i^s}{\sum_{q=1}^{k} \lambda_i^q} \tag{3.7.3.9}$$

which can be rewritten in vector notation as:

$$\left(\sum_{q=1}^{k} \Lambda^q\right) x^s = \lambda^s \tag{3.7.3.10}$$

where Λ^s is a diagonal matrix with the values of λ^s. From this, the minimum energy distribution for the aspatial functional (3.7.3.7) can then be expressed as:

$$E_{rw}(x^s) = \sum_{q=1,\ q\neq s}^{k} x^{qT}\, \Lambda^q\, x^q + (x^q - 1)^T\, \Lambda^s\, (x^s - 1). \tag{3.7.3.10}$$

These energies may be combined into a single functional with the introduction of a free parameter γ as:

$$E_{total} = E_{rw} + \gamma E_{rw} \tag{3.7.3.11}$$

and be minimized with respect to the free nodal probabilities. When adapting with shape priors, γE_{rw} is replaced with the energy functional of the shape prior label, which in this thesis will hence be referred to as E_{priors}. Adaptations of this method have been used for medical image segmentation in multiple situations. For further details, please refer to [155-156].

Chapter 4. Statistical Shape Modelling

4.1 Introduction

As discussed in previous chapters, SSMs have been widely used for computing accurate 3D representations of a targeted anatomy. Although methods of SSM construction have already been established, an optimized framework for modelling the respiratory airway still do not exist. This chapter focuses on the appropriate method of SSM construction and its applications to model generation. Section 4.2 details the selected framework used in this thesis for a level-set SSM construction. Section 4.3 describes the usage of SSM for segmentation through the incorporation of shape energy. Section 4.4 evaluates the robustness of the created SSM through performing assessment on the generality, specificity and compactness. Section 4.5 discusses the captured variances as well as the effectiveness of SSM at predicting new shapes.

4.2 Level-Set Shape Model Construction

The method of SSM construction can be divided into four procedures: training data creation; shape alignment; shape representation; and shape model construction. An overview of the entire process is illustrated in figure 4.2.1.

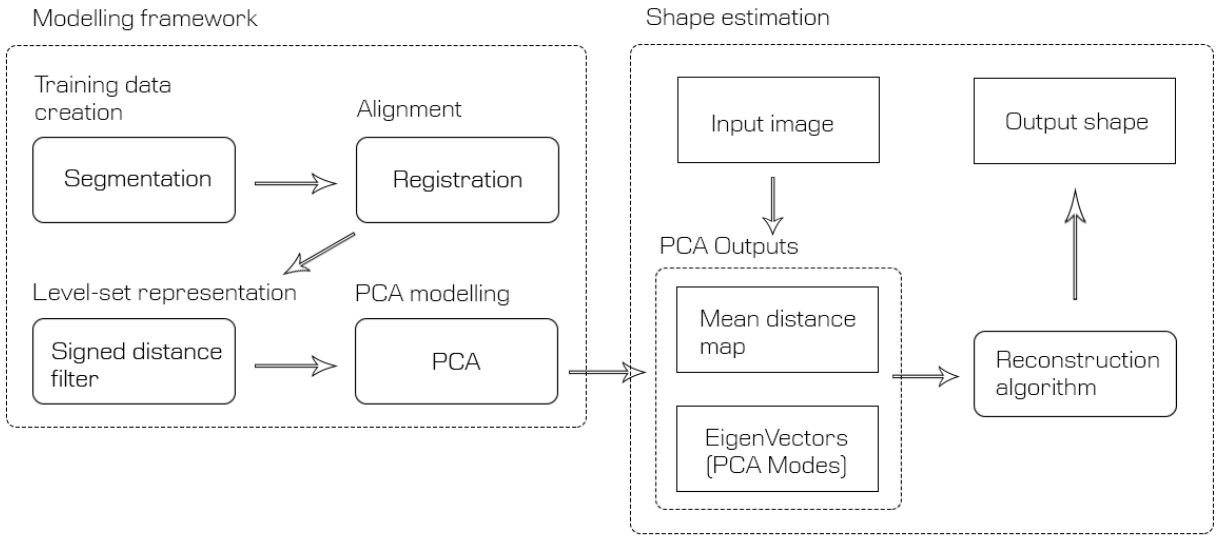

Figure 4.2.1. Framework depicting method of nasal SSM construction

4.2.1 Training Data Creation

Nasal Cavity

For the training data material on the nasal cavity, fifty male subjects between the ages of 35 to 50 provided consent for allowing their CT data to be used in this research. All CT images were obtained from Royal Prince Alfred hospital's Radiology department with each patient's image taken with a GE Lightspeed-16 CT Scanner using Helical CT imaging protocols with an average exposure time of 707 seconds. The resulting images maintain a resolution of 220 by 220 mm (512 by 512 voxels) each with an average of 200 slices where each slice consists of a voxel width and height of 0.43 mm and a voxel depth of 1.25 mm – yielding an approximate overall dimension of 220 by 220 by 250 mm.

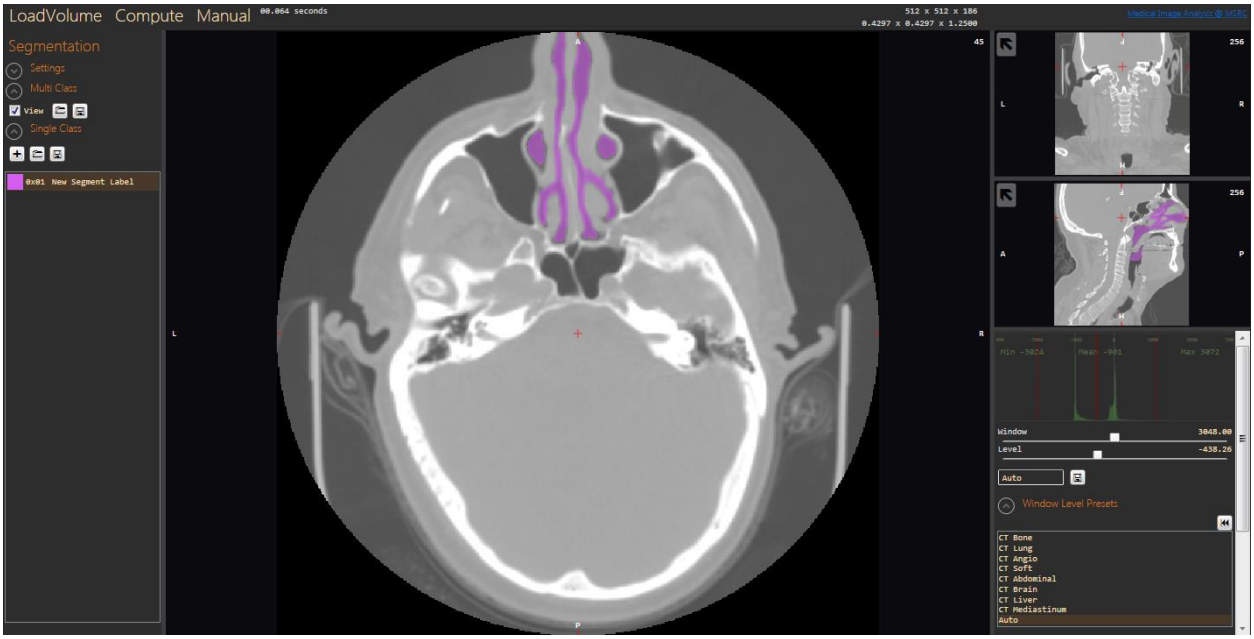

Figure 4.2.1.1 Semi-automatic Geodesic Active Contours segmentation performed using GeoS.

In order to ensure a robust SSM construction, the obtained CT images were semi-automatically segmented using GeoS: Geodesic Image Segmentation [28] by an experienced operator with the assistance of a nasal surgeon. Figure 4.2.1.1 depicts the software used for segmentation. The segmented data were further re-examined by a medical professional with expertise in CT readings to ensure the quality of the training data. Each CT image required approximately half an hour to segment. The semi-automatically segmented images were then used as material for SSM construction.

Trachea and Bronchi

The training data for the trachea and bronchi consisted of 20 whole-body PET-CT patient studies from 20 patients with non-small cell lung cancer (NSCLC) who were scanned in the Department of PET and Nuclear Medicine (Molecular Imaging) at Royal Prince Alfred Hospital (Camperdown, NSW, Australia) on a Biograph TruePoint scanner (Siemens Medical Solutions, Hoffman Estates, IL, USA). All the CT images had a voxel depth of 3 mm, pixel width and height of 0.97 mm, and a matrix size of 512×512 (500 by 500 mm).

The ground truth data were semi-automatically segmented by an operator experienced in medical image processing using Geodesic Image Segmentation. The segmented components is comprised of the trachea which is the central airway that divides at the carina into the left and right main bronchi; the main bronchi then subdivide into smaller lobar bronchi and bronchioles. The resulting segmentation were used as training data for the creation of SSM.

4.2.2 Shape Alignment and Representation

The next step in building our SSM was to align the training shapes (binary segmentations) to a common reference shape to ensure accurate computation of statistics across a population. In order to align the training data, an intensity-based medical image registration using Elastix [29] was performed on the training images (both nasal and tracheal), where rigid registration was initially used to roughly align the training images, followed by a similarity registration to capture scale changes. Of the 50 nasal segmentation images, a single volume was randomly selected as the reference for registration and the rest were separately aligned accordingly to the referenced volume. The same goes to the trachea segmentations.

After registration, Euclidean distance transform was used to convert the binary training data into signed distance maps (SDM); the zero level set representation of binary segmentations; where each voxel in a training image is assigned with a value that is of the distance between it and its nearest nonzero voxel [30]. This allows direct comparisons to be made on a voxel level across a set of SDMs, as voxels of corresponding positions should contain similar values and movement. Since each distance map is subject to approximations instead of precise positions, it is tolerant to slight misalignments and can still allow PCA to capture shape variances inherent in the population due to dependence of nearby voxels in shape representation.

4.2.3 Principal Component Analysis

Statistical shape model construction consists of extracting the mean shape and a number of modes of variation from a collection of training samples. The variation among the set of segmented training shapes is used to describe the variation of the shape model; as such, having a large training dataset would allow for a better representation of the overall distribution of allowable shapes.

We employ shape model construction of Leventon et al. [107] where each shape in the training dataset is embedded as the zero level set of a higher dimensional shape. Here, each zero level set distance map x is a Euclidean distance transform of a binary training shape. The training set T consists of a set of signed distance maps $T = \{x_1, x_2, \dots, x_n\}$, where n is the total number of training shapes. The mean distance surface $\bar{x}$ is first computed by taking the mean of the signed distance maps

$$\bar{x} = \frac{1}{n}\sum x_i \tag{4.2.3.1}$$

The mean shape $\bar{x}$ is then subtracted from each x_i to create a mean-offset map $\hat{x}_i$. Each $\hat{x}_i$ is placed as a column vector in an $N^d \times n$ dimensional matrix M, where N^d is the total number of voxels in each training shape x_i. Using Singular Value Decomposition (SVD), the covariance matrix $\frac{1}{n}MM^T$ is decomposed as:

$$U\Sigma V^T = \frac{1}{n}MM^T \tag{4.2.3.2}$$

where U is a matrix whose column vectors represent the set of orthogonal modes of shape variation and Σ is a diagonal matrix of corresponding singular values.

Decomposing the covariance matrix results in an ordered set of eigenvalues and eigenvectors. Each eigenvector represents a principal mode of shape variation. The associated eigenvalues characterise the amount of shape variance defined by each mode of variation. All training shapes and new nasal shapes can be reconstructed through a linear combination of eigenvectors and the mean signed distance model.

4.2.4 Shape Estimation and Reconstruction

Using data obtained from equation (4.2.3.2), an estimate of a novel shape u can be represented by k principal components in a k-dimensional vector of shape parameters $\propto$, with the maximum value of $k \leq n$:

$$\propto = U_k^T(u - \bar{x}) \tag{4.2.4.1}$$

where U_k is a matrix consisting of the first k columns of U that is used to project a surface into the eigen-space. Given the shape parameters $\propto$, an estimate of the shape u, namely $\tilde{u}$ is reconstructed from U_k and $\bar{x}$ such that:

$$\tilde{u} = U_k \propto + \bar{x} \tag{4.2.4.2}$$

where $\tilde{u}$ results in a matrix containing the estimate SDM of the input shape u. The output of $\tilde{u}$ can then be converted back into that of a binary image. This method is used as a means of validating the accuracy of the constructed nasal SSM through its ability at predicting new shapes.

4.3 Shape Priors

The estimated shape $\tilde{u}$ can further be incorporated into an additional energy term and be adapted with other segmentation methods. In this thesis, the constructed SSM for the nasal cavity was combined with random walker (RW) for image segmentation. The general overview of the RW algorithm was given in section 3.7.3.

4.3.1 Adapting Shape Prior Energy to Random Walker

To combine level-set shape energy into RW, a new energy term called E_{priors} is defined and added to the Dirichlet energy functional given in eq (3.7.3.7), and the entire equation is rewritten as:

$$E_{total} = E_{rw} + E_{priors} \tag{4.3.1.1}$$

where E_{priors} is the fitting constraint that requires the function to be as close to the prior label assignment as possible, and can be simplified as:

$$E_{priors} = (z - \tilde{u})^T (z - \tilde{u}) \tag{4.3.1.2}$$

where z is the solution of random walk probabilities which was formulated as $z = \begin{bmatrix} z_S \\ z_U \end{bmatrix}$. In section 3.7.3, z was denoted as x. To avoid confusions, it has been changed accordingly.

In order to adapt (4.2.4.2) to the probability framework in graph-based systems using matrix calculus, $\bar{x}$ needs to be converted from its SDM representation to probability representation using $\bar{x}_{prob} = \frac{1}{1+\exp(\bar{x})}$. Thus the shape prior energy function can be rewritten as:

$$E_{priors} = (z - (U_k \propto + \bar{x}_{prob}))^T (z - \left(U_k \propto + \bar{x}_{prob}\right)) \tag{4.3.1.2}$$

A segmentation can then be performed through the minimization of the functional $E_{total}(z, \propto)$.

4.4 Evaluation

4.4.1 Evaluation Metrics

We measure the performance of the built SSMs with three quantitative measures: compactness, generality and specificity [135]. Compactness evaluates shape correspondence by measuring the amount of variance of the resulting SSM. Generality evaluates the resulting SSM's ability at representing new shapes, and specificity evaluates shape correspondence through measuring the SSM's capability to generate new legal shapes. We measured compactness as $C(M) = \sum_{i=1}^{M} \lambda_i$ where λ_i is the i^{th} eigenvalue and M being the number of eigenmodes. Model specificity was measured as:

$$S(M) = \frac{1}{N} \sum_{j=1}^{N} \| v_j(M) - w_j^c \|^2 \quad (4.4.1.1)$$

where N is a chosen number of randomly generated shapes, $v_j(M)$ is a randomly generated nasal shape, and w_j^c is the binary nasal training shape in $\{w_1, w_2, \dots w_n\}$ that has the shortest Euclidean distance to $v_j(M)$. The signed distance map form of $v_j(M)$ was randomly generated as:

$$v_j(M) = \bar{x} + \sum_{i=1}^{M} b_i U_i \quad (4.4.1.2)$$

where b_i is a randomly generated value from a Gaussian distribution $N(0, \lambda_i)$.

We use relevant comparison metrics [136] to assess the quality of nasal reconstructions: (i) the average symmetric surface distance (ASSD in mm), (ii) the average symmetric root mean square surface distance (ASRSD in mm), (iii) Absolute Relative Volume Difference (ARVD in %), (iv) Signed Relative Volume Difference (SRVD in ml), (v) Maximum Surface Distance (MSD in mm), (vi) Volumetric Overlap Error (VOE in %), and the (vii) Dice Coefficient Similarity (DSC) calculated as the overlap between the two volumes according to: $DSC = \frac{2\,|X \cap Y|}{|X| + |Y|}$ where X is the segmentation label and Y being the ground truth label. The ASSD and ASRSD are given in millimetres and are based on the surface voxels of two segmentations. The ASSD reflects the overall accuracy of the segmentation while the ASRSD measures the error variations over the shape by including the variance in its calculation. MSD is known as Hausdorff Distance where differences between both sets of surface voxels are determined using Euclidean distances, and the maximum value yields the maximum symmetric surface distance. VOE measures the volumetric overlap

error between two sets of voxels and is given in percentages where a perfect segmentation gives a score of 100.

4.4.2 Compactness

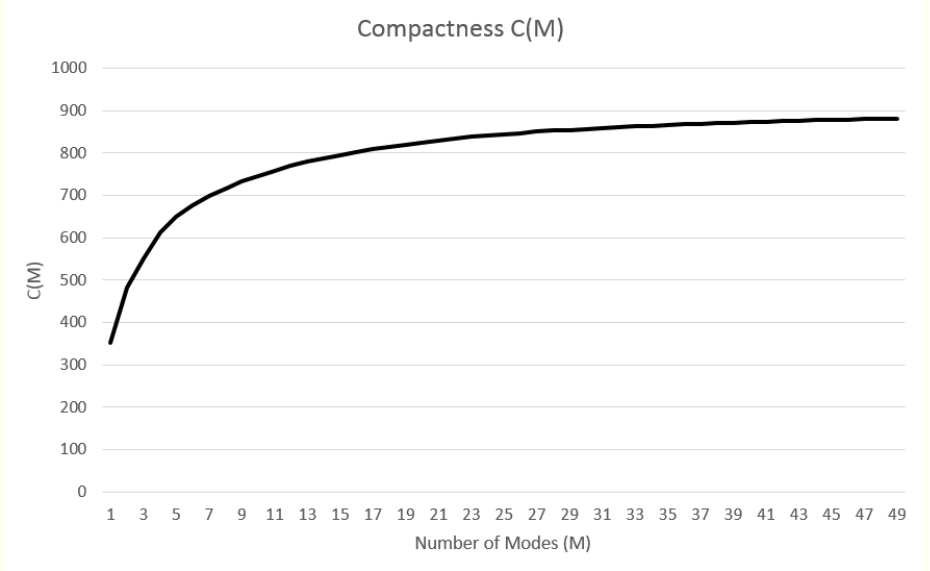

Figure 4.4.2.1. Graph depicting measurement of compactness of constructed SSM.

4.4.3 Specificity

For specificity evaluation, we selected *N* in equation (5) to be 1000. Overall, 50,000 nasal shapes were randomly generated as the results of this evaluation. The outcome of S(M) in mm difference (Euclidean distance divided by total number of voxels, then converted to volume difference) resulted in a range from 530 to 830 mm^3. An averaged volumetric difference of 585 mm^3 was measured when comparing each training shape against 49 other shapes, which can be used as comparison relative to the specificity results.

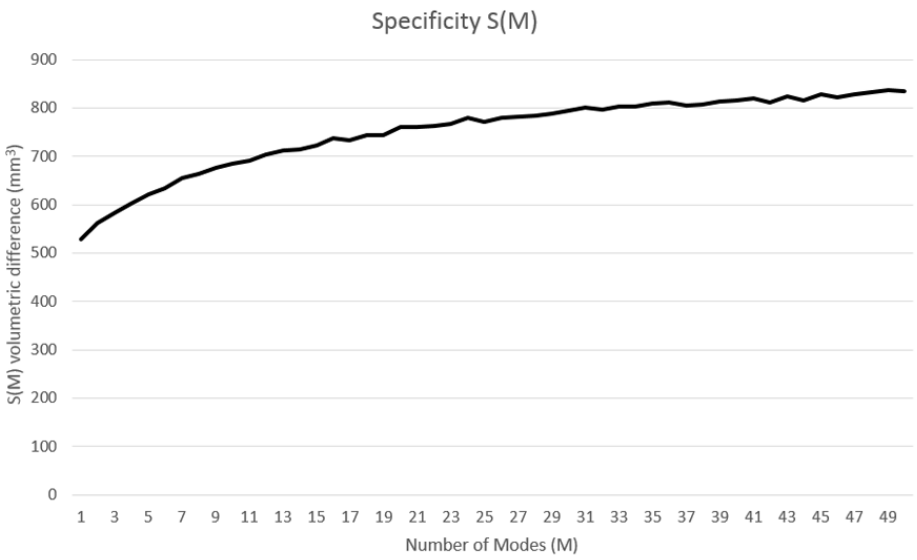

Figure 4.4.3.1. Graph depicting measurement of specificity of 50,000 nasal shapes across 49 eigenmodes.

4.4.4 Generalization

Cross validation was performed on 50 training data set in order to evaluate the generality of our built SSM. This process was repeated for every shape in the training data set. The effectiveness of dimensionality reduction was measured using direct comparisons in performance between SSM built using different amounts of eigenmodes (min 1, max 49). Figure 4.4.4.1 depicts the performance of SSM at predicting new shapes measured using ASSD from 1 mode to 49 modes.

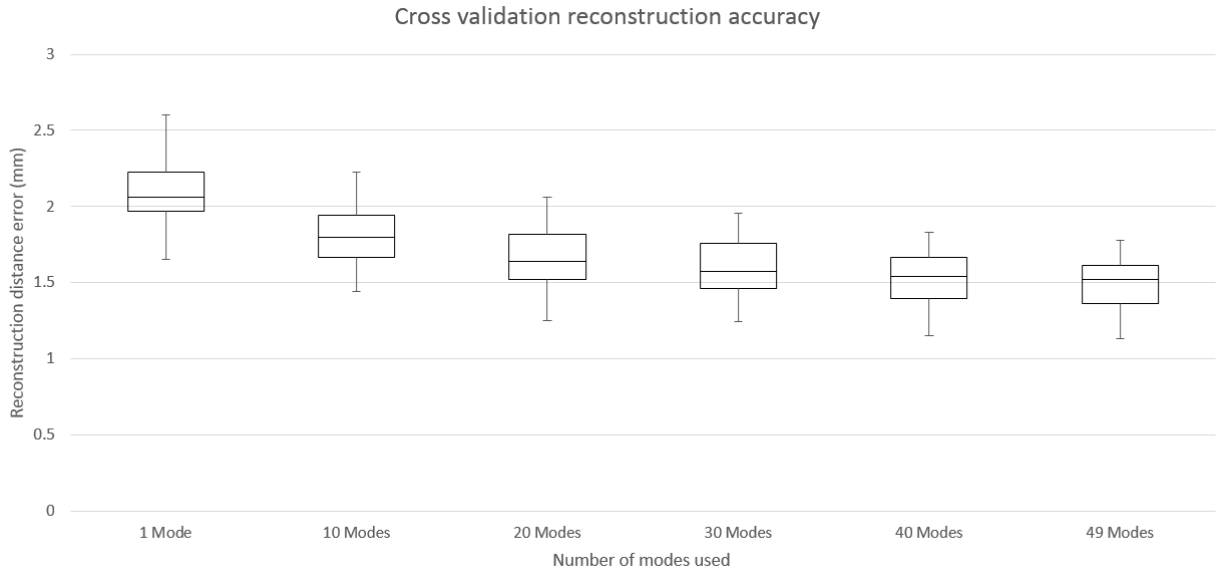

Figure 4.4.4.1 Cross validation accuracy measured using ASSD metrics across 1 to 49 eigenmodes

Table 4.4.4.1 presents the overall measurement of shape approximation evaluated using a number of mentioned metrics. An averaged reconstructed accuracy of 1.51 mm ASSD was observed when using 49 modes as compared to a measurement of 1.54 mm for 40 modes (40 modes was standard deviation of 0.15 mm was calculated for ASSD of 49 modes. The majority of shapes scored within similar accuracy range, with an outlier difference of no more than 0.64 mm. The differences between ASSD and ASRSD, along with the large MSD value suggest that error distribution over the shapes was inhomogeneous. For each nasal shape, we computed the asymmetric distance at the voxel level as being the distance between each voxel of a reference shape and its projection on the reconstructed shape. It is found that large errors mostly occur amongst the nasal side and end passages, where the two areas have been noted to contain large amounts of discrepancy within the training data set. These findings of error prone areas were expected after initial examination of the training dataset. The overall results of validation confirm the success of constructed nasal SSM and that the reconstructed shapes are able to approximately match that of the original testing shape, with an averaged error rate of 1.5 mm.

Modes	DSC Mean	SVD [ML]	SRVD [%]	ARVD [%]	ASSD [MM]	ASRSD [MM]	MSD [MM]	VOE [%]
1	69	25.46	16.19	18.29	2.10	3.22	21.98	48.16
10	71	10.43	6.37	10.09	1.80	2.61	17.46	46.01
20	71	5.49	3.59	8.34	1.66	2.36	15.83	45.07
30	72	3.19	2.37	8.38	1.59	2.24	14.83	44.74
40	72	1.72	1.38	6.83	1.54	2.14	13.91	44.56
49	73	1.30	1.07	6.78	1.51	2.08	13.28	44.57

Table 4.4.4.1 Comprehensive evaluation of generality using different metrics

4.4.5 Case Analysis

An averaged DSC of 73 and ASSD of 1.51 mm was measured when using 49 eigenmodes, with the highest individual accuracy measurement of 81 DSC achieved for shape number 42. Visual comparison between the estimated nasal reconstruction shape and original training shape of case number 42 showed high similarity in features and overall shape. The worst case accuracy measurement was observed in case number 1 which yielded an ASSD of 1.67 mm and a DSC value of 59. This was attributed to the unusual

structure observed in training shape 1's side passage, which consists of two smaller pairs of airway instead of the typical one pair airway observed in the majority of the training shapes. The reconstructed and original shapes for case number 42 and 1 are shown in figure 4.4.5.1, featuring as visualisation of the best and worst shape prediction cases.

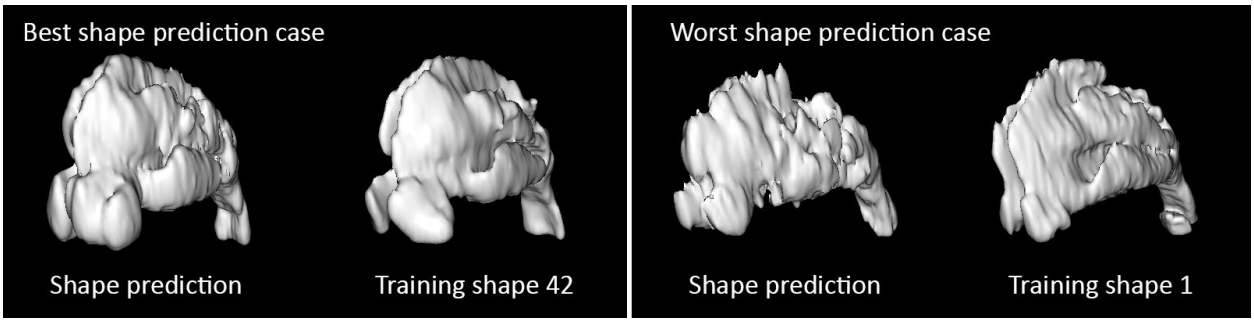

Figure 4.4.5.1 Visualization of best and worst shape predicting cases

Overall, 36 cross validation cases out of 50 were able to achieve a DSC score of equal or higher than 70 when using 49 eigenmodes. Excluding case number 1, the rest of the reconstructed shape predication cases were able to achieve a minimum score of 60 DSC or higher. Further examination reveals that high scoring shapes all share approximate similarities in structure and size when investigated visually. Comparison of DSC and ASSD score between cross validation cases using 40 and 49 modes reveal near similar performance in results between the two. This was expected as 40 modes was initially projected to be able to capture up to 98% of total shape variance. Subsequently, using higher number of modes generally results in better performance.

4.4.6 Examination of Eigenmodes

Examination of the eigenvalues produced by the PCA showed that the first mode was able to capture up to 10% of the variance in the training data, with the first thirty-one modes capturing over 95% of the total variation. The effect of each eigenmode was investigated through manipulating the shape parameter $\propto$ of each mode i (Eq. 4.2.4.2) in the interval $[-3\sigma, 3\sigma](\sigma = \sqrt{\lambda_i})$ and visualising the produced nasal model. Figure 4.4.6.1 depicts the first three modes and their sigma deviations.

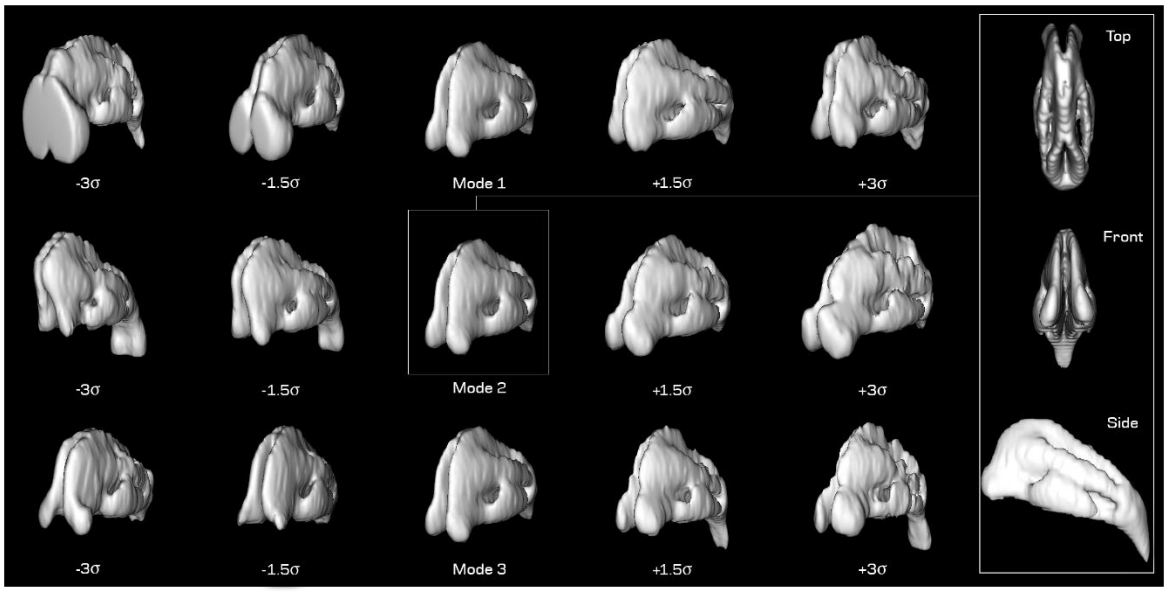

Figure 4.4.6.1 Visualization of the first 3 modes and their sigma deviations

The first eigenmode focuses on the two front passages of the nasal cavity starting from the entrance of the nostrils. As the deviation increases negatively, a difference in the size of the nostril entrances can be observed; the larger the deviation is, the bigger and more distorted the entrance becomes. Differences in the size and curve of the upper section of the nasal airway were also observed. A display of fullness, or well-roundness, can be used to describe the top part of the cavity seen in the -3σ deviation of the first mode. As the value of the shape parameter moves towards the positively end of the spectrum, the top part of the cavity starts to curve inwards and no longer displays the fullness of the passage, while the entrance of the nasal airway becomes considerably smaller.

The second mode influences the size ratio between the front and back of the nasal structure. As we move towards the negative end of the spectrum, the main body of the nasal structure decreases in size while the end passage becomes longer and larger. As for the positive end of the spectrum, it becomes the opposite where the front part of the cavity becomes larger while the end passage becomes relatively thin and small. The third mode influences the length and height of the nasal structure, as can be seen in figure 4.4.6.2, the overall structure changes in length and height each time we increase or decrease the shape parameter. From the left to right, the nasal shapes become taller and longer in length each time the sigma deviation increases from negative to positive, and slowly turns from a rectangular sized shape into a semi-circle shape when viewed from the side.

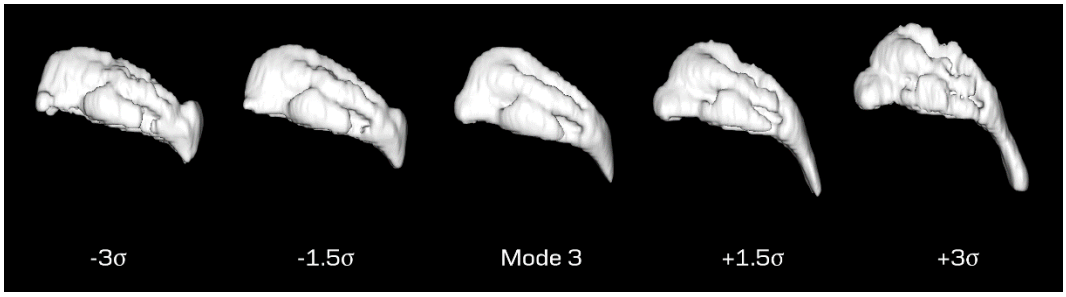

Figure 4.4.6.2 Side view illustration of Mode 3

Although only the first three modes have been visualised in figure 4.4.6.2, clear distinctions can be perceived between each eigenmode. The examination of the first twenty-one modes reveal that each mode influences a specific aspect of the nasal shape. The first ten modes heavily influence the overall structure of the nasal cavity whereas the effects of the later modes are not as strongly observed. Structural changes within the side and upper nasal airway are often correlated to the size of the end nasal passage as well as the width of the entire shape. Comparison between different modes of variation against the initial training images shows similarity in structure, shape and size.

4.5 Discussion

4.5.1 Training Data Size and Complexity

While current results demonstrated the feasibility of level set representation for nasal SSM construction, we suggest that a higher level of shape prediction accuracy can be achieved if a larger training data size was used. As with all level set approaches, its ability at predicting shapes outside of its modelled class can be subpar when compared with using landmarks [127]. For our training data, an average voxel difference of 2500 (575 mm^3) was measured when comparing each training shape against 49 other shapes. This signifies that each of the training shapes approximately contained 2500 features different to others. To further reinforce this view, the first principal mode of our resulting SSM was only able to capture up to 10% of total shape variance. Overall, 40 eigenmodes were required to model 98% of nasal shape variance. This suggested that out of the 50 training shapes, 40 of them contained unique features that are not possessed by other shapes, which greatly impacted our SSM's generality. Hence, we expect an increase in training data size will improve on the overall shape prediction results, as with all population based method, the larger the size of the training data, the better the outcome will be.

4.5.2 SSM Specificity

As discussed in the earlier sections of this paper, specificity expresses the capability of SSM to generate shapes that are specific to the underlying model. An SSM of high specificity is ultimately what we are aiming for as one of the primary goals of this study. However, prior works have noted that for level set based SSMs where PCA is computed using signed distance maps, the resulting feature space might not be a linear space, which is problematic as the linearity of the space is theoretically one of the assumptions to use PCA [127]. This means that with level set SSMs, there exists a probability that it can create shapes outside of its legal bounds (non-specific shapes). Therefore, extra evaluative metrics were employed for the assessment of specificity in order to determine the validity of all generated shapes.

Our initial specificity evaluation revealed a steady increase in voxel difference as more and more eigenmodes were used. Of the 50,000 randomly generated nasal shapes, the highest average voxel difference was measured to be of 3605 voxels. If these voxels are randomly distributed across the nasal surface, an accurate distance error could be calculated using voxels to millimetre conversion. However, since current specificity evaluation methods do not provide information on the distribution of error voxels, the outcome of the evaluation cannot be accurately assessed. Hence, in order to gain a more comprehensive understanding on the accuracy and validity of our specificity evaluation, ASSD metric was computed once more for each generated shape against the training dataset using the same evaluation method. Results listed in the previous section revealed that every mode column maintained an averaged distance error of less than 1.5 mm. The highest distance error within the 50,000 nasal shapes was measured to be 1.79 mm. Visualisation of the worst specificity case is shown in the figure below. Visual examination showed no irregularity in the structure of the generated shape. The worst case for every mode *M* was also visually examined to ensure validity. Overall assessment of shape specificity revealed no irregular nasal shape was created in the 50,000 generated shapes.

Chapter 5. Using Shape-Priors for Segmentation

5.1 Introduction

This chapter focuses on the adaption of prior knowledge for airway segmentation. Section 5.2 adapts the constructed level-set SSM directly with random walker as a hard constraint for the segmentation of the nasal cavity. Section 5.3 adopts a softer constraint process based on the weights of the constructed graph for random walker segmentation on the trachea and bronchial airway. The majority of section 5.2 is taken from [149] while section 5.3 is primarily comprised of [150].

5.2 Nasal Cavity Segmentation

5.2.1 Overview

The nasal cavity belongs to the upper respiratory tract and is a major passage for the transportation of oxygen into the lung. Accurate segmentation of the nasal cavity plays a pivotal role for the creation of patient specific nasal models which are essential for the diagnosis and treatment planning of nasal-related disorders and diseases [6, 27], be of benefit to endonasal surgeries [137], and is critical for research on nasal airflow and drug delivery [24, 25]. Due to the complexity and diversity of the nasal structure as well as the lack of boundary distinction to other airway components, existing algorithms are unable to produce a standalone segmentation of the nasal cavity.

The current known methods [43-50] are capable of producing adequate segmentations of the upper respiratory tract consisting of the nasal cavity, paranasal sinuses and the pharynx using relatively simple algorithms such as thresholding [45-48], region growing [43, 44], level-sets [49], and a level-sets distribution model [50]. However, the majority of these methods requires manual delineation [43-46] and/or requires the imaging modality to be taken from cone-beam CT (CBCT) [46-49] which provides higher contrast and reduces the amount of motion artifacts. More importantly, these methods are restricted by their inability to differentiate and/or separate the nasal cavity from other airway regions components within the upper respiratory tract, thus limiting its application in nasal drug delivery [25] and computational fluid dynamics [51].

The nasal cavity is recognized as a difficult structure to segment due to the complexity and diversity of its anatomy; its interconnectedness to other airway regions; the lack of clear boundaries; and the narrowness observed in many of its airway passages [27, 29]. Figure 5.2.1.1 exemplifies the close proximity of the

paranasal sinuses to the nasal cavity and highlighted some of the connectivity observed between the two regions. The nasal cavity is further directly connected to the entrance of the nostrils, making it difficult for generic segmentation algorithms to prevent leakage. In order to establish clear boundaries around the nasal cavity and to separate it from other airway regions, spatial and anatomical information needs to be utilized.

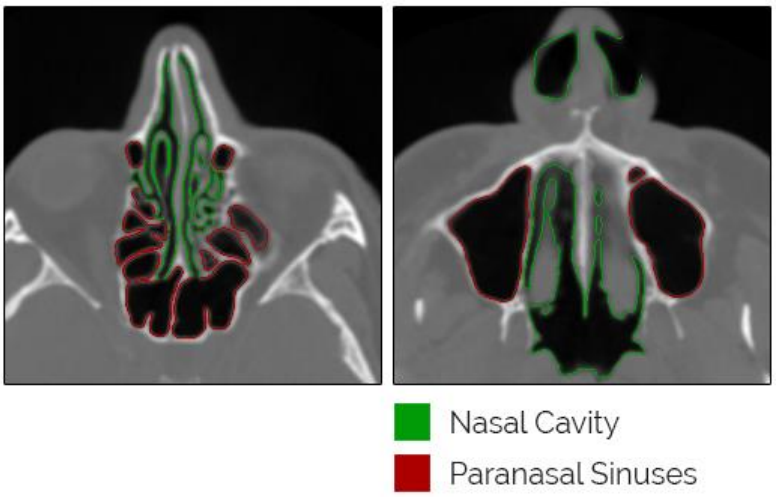

Figure 5.2.1.1 Examples illustrating the connectivity between the nasal cavity to other airway regions in CT.

Statistical shape models (SSM) have been widely employed in the medical image analysis literature as a reliable method for segmentation [119]. Based on a set of training data, the variability of a class of objects can be captured by means of a normal distribution, and the SSM can incorporate this knowledge for segmentation. However, due to the diversity of the nasal cavity structure, it is challenging to establish precise point correspondence for the construction of a generic SSM of the discrete nature. Level-set approaches, which are based on evolving contours do not require point correspondence and can still incorporate statistical knowledge as shape priors into its energy formulation [107, 128]. Although level-set methods have been known to suffer from issues such as becoming trapped inside a local minimum during segmentation, these issues can be avoided by adapting its shape priors for use with other advanced segmentation methods such as graph-based algorithms.

Graph-based algorithms such as graph-cuts (GC) [130] or random walker (RW) [131] have been adapted to work with level-set SSMs in recent literature to overcome the known issues of level-set SSMs at segmentation [129]. Graph-based algorithms formulate an image as a graph, model voxels as graph vertices, assign weights to vertex connectivities and produce vertex labeling by minimizing energy functionals usually based on weights. Compared to GC, RW can better localize specific regions within an

image through the initialization of foreground and background voxels. This makes RW a preferable choice to be adapted with SSM shape priors for nasal segmentation.

In this study, we propose a new fully automated segmentation algorithm designed to overcome the challenges involved in differentiating the nasal cavity from other airway components of the same voxel intensity range. Compared to other literature, our paper makes the following contributions: (i) we present a robust probabilistic-atlas approach for initialization, allowing automatic derivation of the foreground and background seeds needed for our improved statistical RW segmentation; and (ii) we introduce a novel constraint method to locally bind the estimated shape probabilities of RW at each differential iteration stage during segmentation to converge towards a global minimum. Our proposed method was evaluated with 30 volumes of clinical CT data.

5.2.2 Methods

Initialization: Affine and Bspline registration using Elastix [138] is performed on the atlas CT images to align them to the input target image. The transformation parameters of the registration is then applied on the atlas segmentations to warp them to the same reference frame as the target image. A probabilistic multi-atlas A is constructed as the average of the registered segmentations $\{G_1, G_2, \dots, G_n\}$ over the total number of the atlases n, denoted as $A = \frac{1}{n}\sum_{j=1}^{n} G_j$.

Thresholding is applied on the input image to extract the position of the airway voxels. By overlaying A on top of the thresholded image T, an estimate P of the nasal cavity can be obtained from the union of the thresholded image and the atlas, defined as: $P = A \cup T$. The input image is further cropped in order to better localize the nasal cavity and to reduce the computation time. Smaller airway regions captured by P are removed to ensure accurate seeds derivation. Foreground seeds are derived from the remaining airway regions that lie within P. Background seeds are derived from tissue voxels and airway voxels of a distance σ away from P, with σ being a numerical parameter specified during initialization.

Once the required seeds have been derived and an estimate of the nasal cavity P is obtained, we construct the shape priors to capture the statistical variances of the nasal cavity.

SSM Construction: We adopt a similar construction method as to section 4, where a mean offset matrix of the training data, denoted as $\{x_1 - \bar{x}, x_2 - \bar{x}, \dots, x_n - \bar{x}\}$ is constructed, with x_1 to x_n being the signed distance representations of the training shapes and $\bar{x}$ being the mean denoted as $\bar{x} = \frac{1}{n}\sum_{i=1}^{n} x_i$. The resulting eigenvector U and eigenvalues obtained from the singular value decomposition (SVD) of the

mean offset matrix holds the decomposed features of the nasal cavity shape across a linear distribution. An estimate of a novel nasal shape s_{est}, can be represented by k principal components in a k-dimensional vector of coefficients, α:

$$S_{est} = U_k\alpha + \bar{x} \tag{5.2.2.1}$$

Due to the diversity of the nasal cavity structure, it is necessary for outlier shapes to be removed from the training data. A similarity guided framework was implemented to assign a weight w to each training shape t calculated as $w = \frac{|P \cap t|}{|P|+|t|-|P \cap t|}$. Nasal shapes that scored below the mean weight were removed from the training dataset.

Segmentation: We embed the constructed SSM in a graph-based segmentation framework and formulate an image as a graph $G = (V, E)$, where each vertex $v \in V$ corresponds to an image voxel and each edge $e \in E$ connects two vertices in V. We borrow the idea from RW and construct the Dirichlet energy as $E_{rw} = z^T Lz$, where L is the Laplacian matrix defined in [131] and denotes the pairwise affinities among the vertices in V, and $z \in R^{|V|\times 2}$ is a labeling vector indicating voxel foreground (background) probabilities. In our nasal cavity segmentation problem, we define a new energy term which holds the captured shape variances from the nasal SSM to the labeling vector of image voxels. The labeling vector can be optimized by solving a graph Dirichlet problem to produce the final probabilistic labeling. The proposed energy term was defined as:

$$E_{\ priors} = z - (U_k\alpha + \bar{x}_{prob}))^{\mathrm{T}}(z - \left(U_k\alpha + \bar{x}_{prob}\right)) \tag{5.2.2.2}$$

where $\bar{x}_{prob} = \frac{1}{1+\exp(\bar{x})}$ and $z = \begin{bmatrix} z_M \\ z_N \end{bmatrix}$, where z_M denotes the predefined labels i.e. foreground and background seeds, and z_N denotes other labels. Given the definition of E_{priors}, the complete energy function is formulated as $E_{total} = E_{rw} + E_{priors}$.

An estimation of the nasal cavity is obtained by minimizing the proposed functional $E_{total}(z_N, \alpha)$, iteratively, with respect to each of its variables z_N and α. First, we start from the mean shape and initialize $\alpha = 0$. Since E_{total} is convex, we differentiate E_{total} with respect to z_N and find the critical point yielding:

$$z_N = (L_N + I)^{-1}(2\left(U_k\alpha + \bar{x}_{prob}\right) - B^{\mathrm{T}}z_M) \tag{5.2.2.3}$$

where *I* is an identity matrix, *L* is the Laplacian matrix of the image and *B* is the matrix partitioned from *L* which correlates the labeled set to the unlabeled set. Secondly, we use the updated z_N to differentiate E_{total} once more with respect to α, which yields the following:

$$\alpha = (U_k^{\mathrm{T}} U_k)^{-1} U_k^{\mathrm{T}} (z_N - \bar{x}). \quad (5.2.2.4)$$

In order to reduce the amount of over-segmentation caused by the influence of the shape prior term without lessening its effect, we constrained the output of E_{total} to remain within the boundaries of the nasal airway by computing a probability of the estimated foreground voxels and removing those which overlapped into the tissue regions based on their intensity value at each step of the differential iteration.

5.2.3 Results

Experimental Setup

We performed the leave-one-out cross validation on 30 CT images (30 folds) where 29 ground truth labels were used each time for the creation of the PA and SSM. We set the initialization parameter σ=5. This value was empirically derived based on experiment validations.

We compared our algorithm to both the conventional and recent state-of-the-art segmentation algorithms including Probabilistic Multi Atlas (MA) [139], Grow-Cut (GC) [140], Seeded Region Growing (SRG) [141], Random Walker (RW) [131], Distance Regularized Level Set (DRLSE) [104], and Laplacian Coordinates (LAP) [142]. For MA, consistent to our algorithm, for each test images, 29 atlases were registered into the input image and the final result was the average of the transformed labels. We used the same seeds derived from our algorithm to initialize the segmentation for GC, SRG, LAP, DRLSE and RW. We used the same evaluation metrics as the previous SSM generality assessment.

Experimental Results

Table 5.2.3.1 presents the segmentation results of our algorithm compared with other methods. Our algorithm achieved the highest averaged DSC (90.9%), the lowest averaged distance error (0.34±0.07 mm), the lowest ASRSD (1.07 mm), and the least amount of VOE (16.6%).

Evaluation Metrics	*DSC*	*ASSD*	*ASRSD*	*MSD*	*VOE*
Our method	$\mathbf{90.9 \pm 2.2}$	$\mathbf{0.34 \pm 0.07}$	$\mathbf{1.07 \pm 0.11}$	$\mathbf{9.5 \pm 0.7}$	$\mathbf{16.6 \pm 3.6}$
GC	65.08±4.7	1.72±0.2	2.98±0.6	22.31±7.2	50.67±4.7
RW	64.59±4.4	0.98±0.04	1.67±0.01	10.58±0.3	50.03±4.3
DRLSE	63.91±0.9	1.13±0.01	1.91±0.1	12.23±0.7	52.78±1.0
LAP	61.79±2.8	1.22±0.04	2.04±0.2	11.51±0.6	54.39±2.9
MA	60.91±3.7	1.06±0.1	1.63±0.2	9.87±0.9	56.08±4.1
SRG	60.21±6.2	1.26±0.2	2.22±0.2	15.43±1.0	55.88±5.9

Table 5.2.3.1. Comparative evaluation of our algorithm against other methods at segmenting the nasal cavity

Quantitative evaluation of our proposed algorithm (blue) when compared against the RW (orange) is shown in figure 5.2.3.1. We selected RW as the base method for comparison to demonstrate the effect of the level set shape priors on nasal segmentation. Our algorithm which incorporated statistical knowledge achieved the best minimum (85.1%) and maximum (97.2%).

Figure 5.2.3.1. A quantitative DSC evaluation of our algorithm with comparison to the base RW algorithm

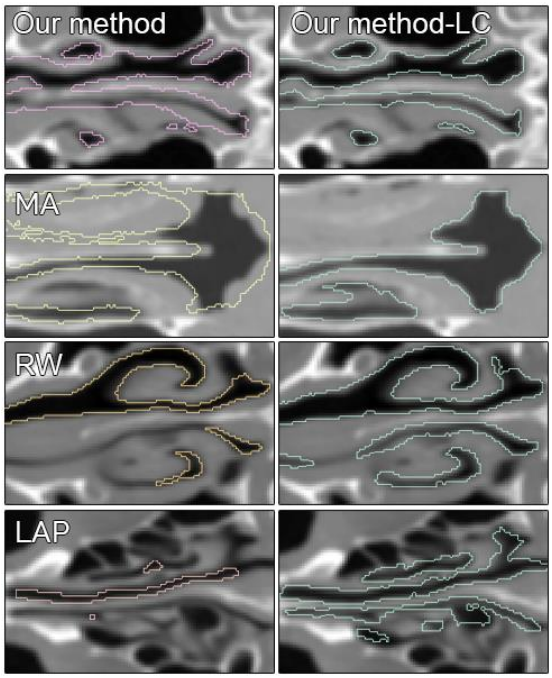

Figure 5.2.3.1. Comparison of our method (right column) against MA, RW, and LAP

5.2.4 Discussion

Overall, our method was able to achieve a much higher accuracy rate primarily due to the influence of statistical priors to the segmentation algorithm. The nasal passages contains very narrow airway pathways in which the width of the passage could, at certain sections of the structure, be as thin as roughly two voxels across in distance. Furthermore, those voxels at times contains a lowered intensity value due to fuzziness of the CT image. This causes seed-reliant algorithms to experience under-segmentation in certain areas of the nasal cavity. The effect of the shape priors is able to overcome this difficulty and allow our algorithm to connect across thin passages found within the nasal structure through the evolution of the shape approximation initialized during the differential stage of the segmentation. Over-segmentation was also minimized, preventing leakage into non-nasal airway regions such as the paranasal sinuses. The majority of the other tested algorithms were unable to minimize this issue.

Figure 5.2.3.2 illustrated where the majority of the segmentation errors occur at for other algorithms. Region-based methods (RW, LAP, GC, SRG) all experienced the same weakness at segmenting the narrower passages within the nasal cavity structure, mainly caused by the fuzziness of the voxel intensity. RW, LAP, and DRLSE performed considerably better than GC and SRG due to the advantage of the background seeds which prevented the majority of the leakage. GC and SRG suffered from both under-segmentation and over-segmentation, with the majority of the over-segmented area being at the

entrance of the nostrils. Algorithms that made use of prior knowledge tend to perform better in our experiments due to their ability to detect the narrower airway passages within the nasal structure.

5.3 Airway Tree Segmentation

5.3.1 Overview

Positron emission tomography (PET) combined with computed tomography (CT) is a routine imaging modality for the diagnosis and interpretation of malignant diseases of the thorax [143]. Accurate airway segmentation is critical for the localization of sites of abnormal metabolism detected with PET-CT. Such localization is pivotal to accurate disease staging prior to consideration of surgery and for radiation therapy planning [55, 144]. The CT performed in PET-CT has a lower radiation dose when compared to conventional chest CT. This results in images with a relatively lower soft tissue contrast which makes the separation of the airway tree from adjacent structures challenging. Figure 5.3.1.1 exemplifies the difference between low-contrast CT with high-resolution CT (images from the EXACT09 [52] dataset). In this example, we can see that when compared against low-contrast CT, high-resolution CT exhibits considerably greater anatomical details and maintains clearer boundary distinctions between airway and non-airway voxels. In addition, high-resolution CT is less susceptible to anatomy-related artefacts such as airway obstructions and heart beat motion. These image characteristics adds greater complexity in segmentation of low-contrast CT images.

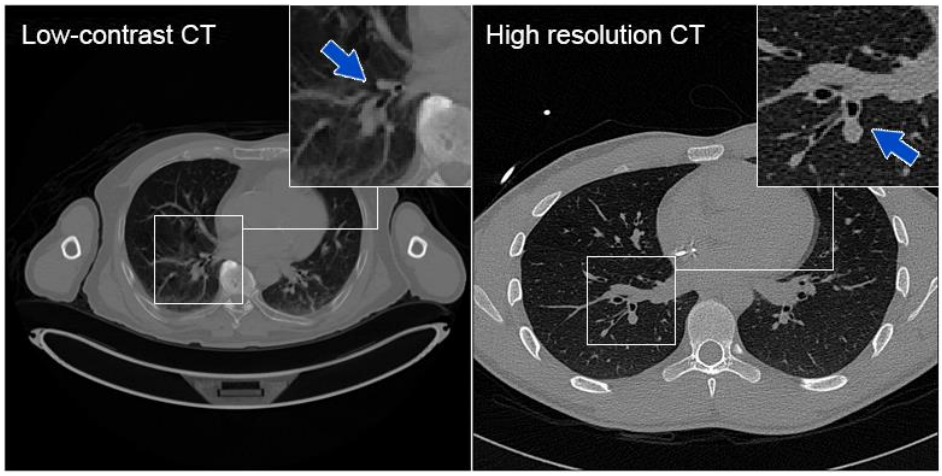

Figure 5.3.1.1 Comparison of airway structure between a low-contrast CT (left) 0.97x0.97x3 mm pixel resolution (512x512) compared against a high-resolution CT (right) with 0.6 x 0.6 x 0.6 mm pixel resolution (512x512). The inserts are1.5x zoomed images. The high-resolution CT have greater details depicting the airway structure.

This section presents a fully automated airway segmentation algorithm designed to overcome the characteristics of low-contrast CT images. Compared to other methods, our approach makes the following contributions: (i) we introduce the use of multi-atlas for the initialization of the segmentation process. For low-contrast images that are prone to cause leakage, it is important to accurately determine foreground and background voxels. By incorporating shape priors gained from our multi-atlas initialization, robust seeds can be derived for segmentation; and (ii) we propose the use of an efficient locally constrained random walker algorithm. Random Walker (RW) is a well-known interactive segmentation algorithm which requires manual input of seed points and segments the target image as a weighted graph structure containing nodes and edges [131]. By combining RW with spatial and anatomical information derived from our shape priors, a knowledge-based random walk can be achieved through constraining the edge weights. Our algorithm was evaluated against 20 clinical low-contrast CT from PET-CT studies and was compared against other well-known algorithms including region growing [141], multi-atlas [145], grow-cut [146], and geodesic active contour segmentations [132].

5.3.2 Methods

Our method of airway segmentation can be separated into two components: initialization and segmentation. The novelty of our method is to utilize shape prior knowledge gained from multi-atlas registration to accurately derive robust seeds for our locally constrained random walk segmentation. We further made use of our shape priors to restrain the weights among graph edges to lean towards voxels with high probability of being part of the airway structure. An overview of the method is shown in figure 5.3.2.1.

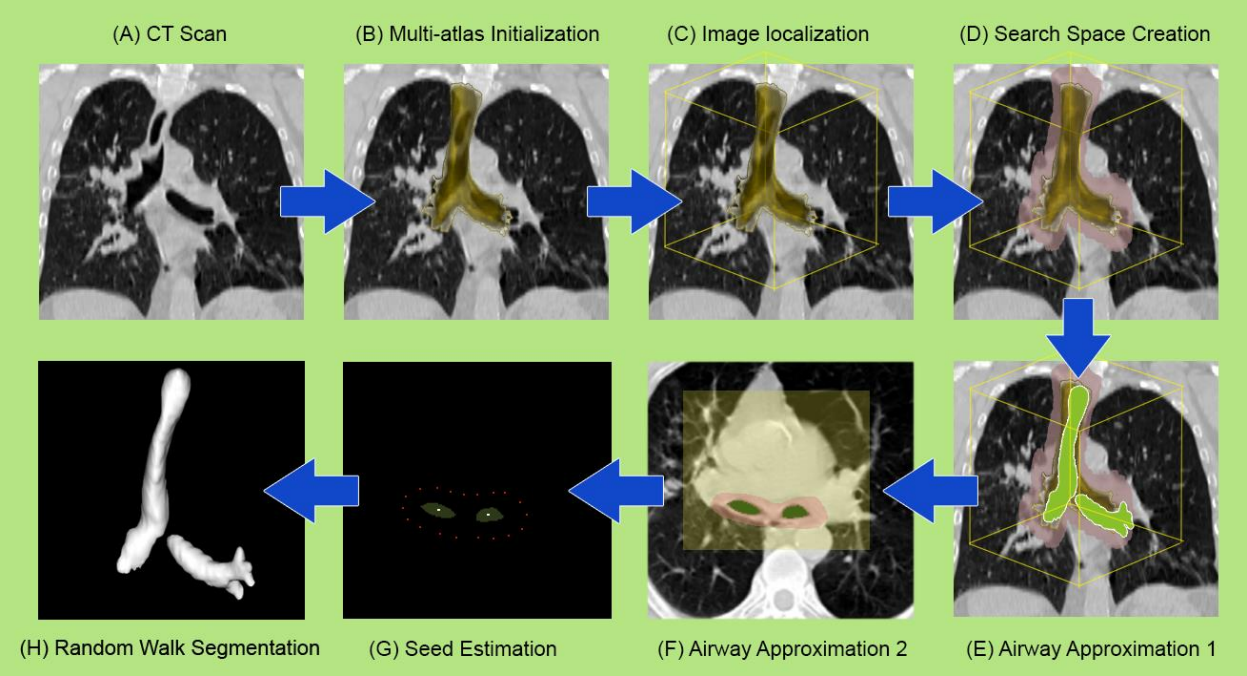

Figure 5.3.2.1 Flowchart of our proposed segmentation method. The visualized result shown in part (G) contains an obstructed airway branch which is disconnected from the main airway.

Initialisation: affine and Bspline registration using Elastix [138] were performed on the atlas CT images to the input target image. The transformation parameters of the registration were then applied to the atlas segmentations to warp them to the same reference frame as the target image. The registered atlas segmentations will then be used as shape priors for our algorithm. The results of each shape prior transformation was superimposed onto one image to form an initial multi-atlas-based estimation of the main trachea structure, which we refer to it as the shape priors region. A visual illustration of the initialized shape priors region is shown in Figure 5.3.2.1 (B). In order to reduce computation time, the input image was cropped based on the initial placement of the shape priors.

A signed distance map of the shape priors region was computed to assign a distance value to voxels that do not reside in the shape prior region. We selected a distance value σ, as a parameter used for performing a constrained threshold on airway voxels within distance σ to the shape priors region. The thresholded voxels become the initial search area for our airway approximation step as illustrated in Figure 5.3.2.1 (E). 3D connected region detection was used to group the thresholded voxels into separate airway regions. We iteratively looked through each region r for those with a high voxel count and have a high probability of being part of the trachea airway. We used the parameter value γ as selection criteria where regions that have a higher voxel count than γ were kept. Regions that have a voxel count of below

γ were removed as background noise. A probability value $P(r)$ was then calculated and assigned to the remaining regions. The value $P(r)$ can be derived as:

$$P(r) = \frac{|r| \cap |X|}{|r|} \quad (5.3.2.1)$$

where X is the shape priors region. We used φ as another parameter value for the selection of regions for airway approximation. All regions where $P(r) > \varphi$ were kept as the final approximation. The derived airway approximation region(s) were further added to the shape priors region.

The seeds used for segmentation were derived from the airway approximation. For each slice within our airway approximation, 2D connected region detection was employed in order to locate the number of airway regions within in 2D slice. We selected regions with a pixel count of greater than λ to derive seeds. This was to ensure that our algorithm would only derive seeds from definite regions within the airway structure. The centroid of each region was then calculated and used as the foreground seed for random walk as shown in Figure 2 (G). Background seeds were derived from the voxels that are on the edge of the constrained signed distance region where the boundary voxels maintain a distance value of smaller than σ.

Segmentation: we adapted the work reported by Grady et al [131] as part of our segmentation pipeline. Given an input image, a graph consisting of $G = (V, E)$ with nodes $v \in V$ and edges $e \in E$ can be derived. For 3D images, 26-connected lattice was used for the construction of V and E. An edge e, spanning two nodes v_i and v_j, is denoted by e_{ij}. A weight is assigned to each edge in order to provide better path finding. The weight of an edge e_{ij} is denoted by w_{ij} and is given as:

$$w_{ij} = \exp(-\beta\alpha(g_i - g_j)^2) \quad (5.3.2.1)$$

where g_i indicates the image intensity at voxel i. The value of β is a changeable parameter value which controls the edge weight w_{ij}, where large values of β restricts the random walks from crossing edges more easily. α is calculated as:

$$\alpha = 1 + (P(v_i) - P(v_j)) \quad (5.3.2.2)$$

where $P(v_i)$ is the probability of voxel i being part of the airway structure. The probability is derived as:

$$P(v_i) = \frac{x_i}{N} \quad (5.3.2.3)$$

such that x_i is the number of overlap of shape priors at voxel i and N is the total number of priors used.

The weight of α makes the random walk harder to cross fuzzy boundaries that are outside the region of the shape priors or voxels where the probability values are low. This will prevent leakage from occurring during segmentation.

The RW algorithm computes the probability for each voxel that a *random* walk leaving that voxel will first arrive at a foreground seed before arriving at a background seed. These probabilities can be computed by solving a linear equations with a graph Laplacian matrix defined as:

$$L(i,j) = \begin{cases} d_i & \text{if } i = j, \\ -w_{ij} & \text{if } v_i \text{ and } v_i \text{ are adjacent nodes,} \\ 0 & \text{otherwise,} \end{cases} \quad (5.3.2.4)$$

where $L(i,j)$ is indexed by nodes v_i and v_j.

Given a set of foreground seeds V_F and background seeds V_B, where $V_F \cap V_B = \emptyset, V_S = V_F \cup V_B$. We can compute the probabilities x_i that a random walk leaving node v_i arrives at a node in V_F before arriving at a node V_B by solving

$$L_U x_U = -B x_S. \quad (5.3.2.5)$$

The variable x_U represent the set of probabilities corresponding to unseeded nodes. x_S is the set of probabilities corresponding to seeded nodes (i.e., 1 for foreground and 0 for background nodes). L_U and B correspond to the matrix decomposition of L

$$L = \begin{bmatrix} L_S & B \\ B^T & L_U \end{bmatrix}. \quad (5.3.2.6)$$

Using the probability obtained by solving (6), each voxel in the image is then assigned to its corresponding label for which it has the highest likelihood of being (either as part of the foreground or background).

While the typical size of the Laplacian matrix L is constructed from $E \times E$, which often results in a large matrix especially when applied on 3D images. The size of L can be heavily reduced if spatial and anatomical knowledge was provided beforehand. By constraining the search space of L to only the voxels that are within a predetermined search space, as shown in Fig 5.3.2.1. (D), a much smaller Laplacian matrix can be used for computing the final probabilities.

For our algorithm, we locally constrained the search space of L by building the Laplacian matrix using only edges e_{ij} found within the constrained space of our signed distance map created from the combination of our shape priors region and the airway approximation, where i and j are voxels that with a distance value of less than $\sigma + 1$. In order for RW to successfully perform segmentation on a constrained space of L, the distance of the constrained search space needs to be greater than σ so that a walk can exist between all foreground and background seeds.

Below is a pseudo code implementation of our method.

Algorithm

Initialisation:

1: Perform multi-atlas registration using affine and bspline transformations

2: Obtain the shape priors region from the registration

3: Calculate a coarse boundary based on the voxel distance away from the highest overlap voxel within the shape priors region

4: Crop input image using boundary calculation

5: Create a signed distance map of multi-atlas region

6: Perform thresholding on voxels that have a signed distance value of under σ

7: Perform 3D region detection on the thresholded result

8: For each region r sort by descending order based on the number of voxels

    If the number of voxels in $r > \gamma$

        If $P(r) > \varphi$

            Add r to airway approximation

        End if

    End if

End

9: For each slice s in airway approximation

    Perform 2D region detection

    For each region sr detected

        If number of pixels in $sr > \lambda$

            Calculate centroid of sr

        End if

    End

End

10: Derive foreground seeds from centroids

11: Derive background seeds from the boundary of the constrained threshold region

Segmentation:

12: Create a search space localization from signed distance map on voxels that have a distance value of under $\sigma + 1$

13: Create probabilistic weight map (explained further in later section)

14: Perform random walk on localized search space

5.3.3 Results

Experimental Setup

We performed the leave-one-out cross validation on 20 CT images (20 folds) where 19 ground truth labels were used each time as part of our initialization process against the input image. Parameter setting for initialization was as following: $\sigma = 4$, $\gamma = 800$, $\lambda = 26$, and $\varphi = 0.8$. These values were empirically derived based on experiment validations. For our setup, we kept the parameter value σ relatively low in order to better accommodate for γ; as larger values of σ would cause additional lung voxels to be included during the approximation phase which would require higher values of γ to compensate for accuracy. The parameter γ was explained previously for determining which voxel regions to remove from the search space (Section II. B). Generally, higher γ values provide better accuracy as it would remove almost all other airway regions picked up during the initial threshold. However, we kept our γ value low in order to locate proximal airway regions that may be disconnected from the main bronchi due to pathological conditions. The resulting seed points were then used as part of the starting parameters for our segmentation process, where the edge weight parameter β was empirically set to 50.

We compared our proposed algorithm with both semi-automated and fully-automated segmentation algorithms including the Multi-Atlas based segmentation (MA) [139, 145], Grow Cut (GC) [140, 146], Connected Region Growing (CRG) [141] and Geodesic Active Contour (GAC) [132]. For MA, as consistent to our algorithm, for each test images, the rest of 19 atlases were registered into the input image and the final result was derived by averaging the transformed labels. We used the same seeds definition to initialize the segmentation for GC, CRG and GAC. For CRG a standard deviation was needed to be defined as convergence criteria. We iteratively tested the results with an increment of 0.1 and the best performing results were reported.

Experimental Results

Table 5.3.3.1 presents the segmentation results of our algorithm when compared to the other algorithms evaluated using the DSC measure. Our algorithm had the highest overall mean (87.2), the smallest standard deviation (2.8) and the best minimum (78.6) and maximum accuracy (90.8). GAC was the next best performing algorithm with an overall average of (77.4). GC, CRG, and MA performed much worse compared to our method and GAC.

Method	*Mean*	*SD*	*Min*	*Max*
Our Algorithm	**87.1**	**2.8**	**78.7**	**90.8**
GC	54.1	21	11.5	90
CRG	63.8	19	7.6	76
GAC	77.4	3.4	68.9	83.2
MA	57.2	8.3	36.4	66.5

Table 5.3.3.1 Comparative evaluation of our segmentation algorithm against other methods on 20 testing dataset measured using DSC

Table 5.3.3.2 presents the segmentation results of our algorithm with comparison to other methods evaluated using the full set of comprehensive metrics. Our method had the lowest averaged distance error of 0.37 *mm* ASSD, 0.9 *mm* ASRSD, and contained the least amount of VOE at 21.6%.

Evaluation Metrics	*Our algorithm*	*GC*	*CRG*	*GAC*
SRVD [ml]	**13.8**	-34.6	63.2	51.9
ARVD [%]	**13.7**	35.3	81	51.9
ASSD [mm]	**0.37**	2.21	1.8	2.8
ASRSD [mm]	**0.9**	3.8	2.4	7.4
MSD [mm]	12.3	15.8	**10.4**	39.8
VOE [%]	**21.6**	48.2	49.3	37.1

Table 5.3.3.2 Comparative evaluation of our segmentation algorithm and other methods measured using ASSD, ASRSD, ARVD, SRVD, MSD and VOE.

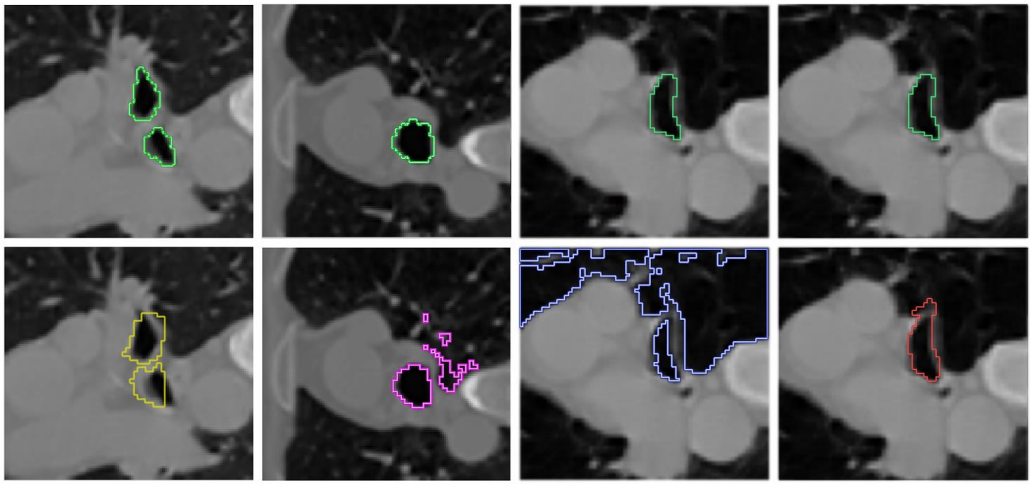

Figure 5.3.3.1 Example of airway segmentation results among different algorithms with comparison to our method. Green (our method), yellow (MA), purple (GA), blue (CRG) and red (GAC)

5.3.4 Discussion

Quantitative Evaluation

Our algorithm performed the best overall. This was mainly because it was able to address the region leakage via spatial constraints derived from the multi-atlas registration. Our algorithm further benefited the most from robust seeds derived from our initialization process optimized for our modified RW segmentation. Compared to conventional region-based methods, our algorithm was designed to take full advantage of knowledge derived from shape priors. Generally, region-based methods including GC, CRG and GAC performed well at segmenting the trachea when it was distinctively separated from the lungs; however, over segmentations commonly occurred when the distance between the trachea and the lungs became small, i.e., less than 3 voxels, and/or if the boundary voxels were fuzzy. Figure 5.3.3.1 shows examples of our algorithm correctly segmenting the trachea section while GC, GAC and CRG suffered from over-segmentation. GC performed the worst overall due to the excessive leakage. CRG generally performed well and had fewer leakages in the majority of the images; however it failed in images with weak boundaries. CRG had the lowest minimum accuracy of (7.6 DSC) and also suffered most from under-segmentation in the majority of the images, where smaller bronchial branches often went unsegmented. GAC performed second where it encountered less leakages compared to GC and CRG. However, the main issue that was experienced with GAC was the reliance on seeds. We observed that GAC was able to accurately segment sections of the airway which contains seeds derived from our initialization process. However, GAC was unable to extend its segmentation range beyond the location of derived seeds deeper

into the airway branches. MA also performed relatively poorly when compared to other evaluated methods, which was likely due to the large variations observed in the trachea where MA was based on averaging from the probabilistic atlases. Although the overall accuracy of MA was not high, as expected, it encountered minimal leakage due to the spatial constraint of the multi-atlases.

Segmentation Challenges

The greatest challenge experienced when segmenting the airway structure on low-contrast CT images was resolving the region leakage problem. Unlike in high-resolution CT images, the walls of the bronchial tree tends to fade into the background soon after the trachea bifurcates as shown in Figure 4. In situations like this, region-based algorithms tend to leak out into the lungs. Additional challenges encountered were from pathological conditions found within the airway structures such as patients with missing lungs or those suffering from tracheobronchial injury [147] where an entire section of the trachea to bronchi passage was disconnected from the main airway.

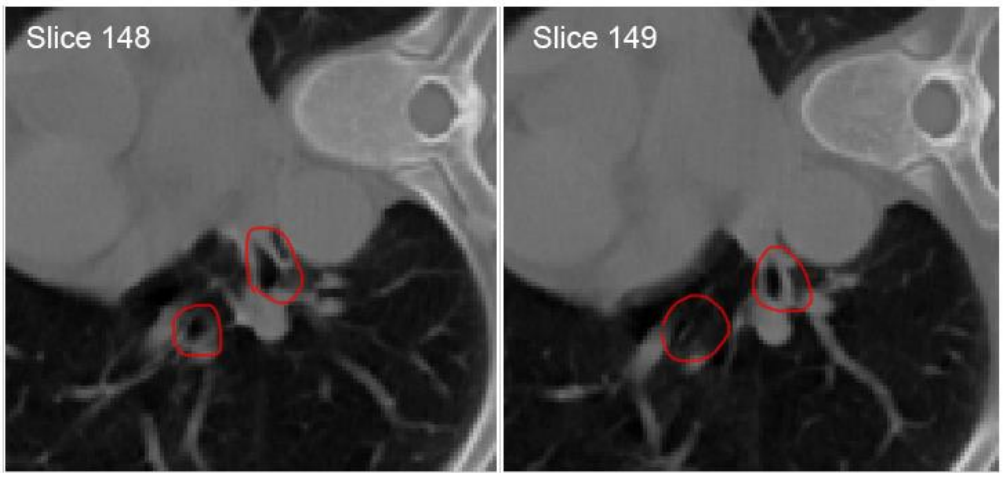

Figure 5.3.3.2 Illustration showing the disappearance of airway wall. The airspace that are connected to the main trachea structure are highlighted in red.

To overcome these challenges, we designed our initialization to identify large disconnected sections of the airway structure during the airway approximation stage. Seeds were then allocated to all the identified sections of the airway. We achieved this through the use of shape priors initialized from our multi-atlas registration. Airways that fell within the boundaries of the shape priors were included within our approximation process. Random walk segmentation using multiple seeds, including those derived from disconnected airway sections, was then able to correctly segment these pathological CT images.

Application to PET-CT Visualization

Figure 5.3.3.3 shows an application of our airway segmentation in a volume rendered visualization of a multi-modality PET-CT lung cancer. The CT volume rendering (with transfer function manipulations the same as in [148]) was augmented on a single slice of the PET image. In this figure, we can see the tumor region in context of the segmented trachea airway structure. Each column depicts different views: (a) coronal in left column; (b) axial in middle column; and (c) sagittal in right column. In this example, the segmented PET-CT enables visualization of patho-physiological function with PET in the spatial context of its anatomical CT counterpart. Our trachea segmentation provides visual distinction and thus allows differentiation of the trachea with neighboring CT structures.

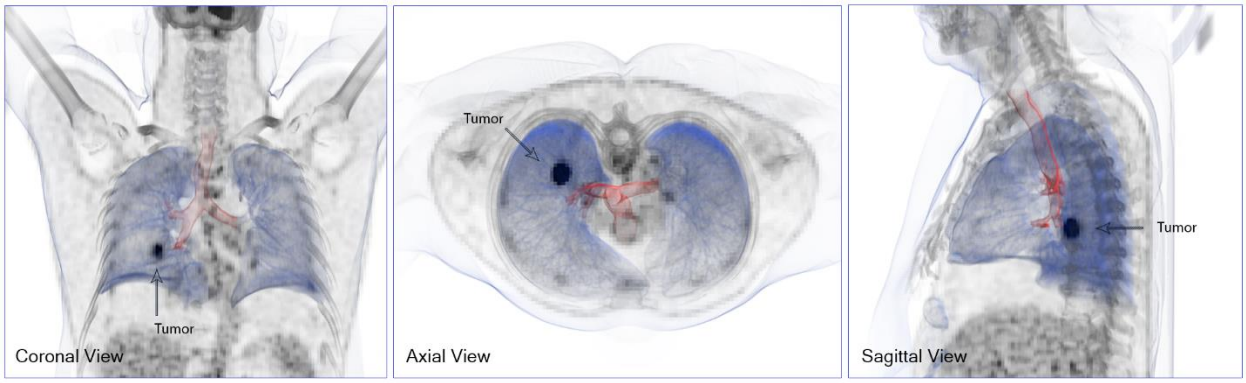

Figure 5.3.3.3. Volume visualizations of PET-CT in a lung cancer patient in which the segmented trachea (colorized by red) is outlined: (a) coronal; (b) axial; and (c) sagittal views. The relation of the parenchymal tumour (labeled and indicated by arrows) and its relation to the central airways is more easily appreciated from our segmentation.

Chapter 6. Computational Fluid Dynamics

6.1 Introduction

This chapter focuses on the applications of SSM and its clinical significance especially in the field of computational fluid dynamics (CFD). CFD is a branch of fluid mechanics that uses numerical analysis and data structures to solve and analyze problems that involve fluid flows. Accurate modelling and mapping of the nasal airway is essential for deriving a clearer understanding of the pathophysiology and airflow within the respiratory system. Many clinical applications and studies, such as nasal surgery, require detailed information regarding each individual patient's nasal structure and airflow, and recently, the use of computer-assisted measures via CFD has become a standard approach to model the airflow within the nasal cavity [26]. Although CFD modelling has become a fast and reliable research tool for the studying of nasal pathophysiology and airflow [24, 149-152], there is a lack of reliable frameworks to efficiently segment the nasal cavity from medical images for the creation of CFD models. Due to the connectivity between the nasal cavity and other airway components, such as the paranasal sinuses where the connected airways share a similar intensity value range and do not possess any distinct boundaries to differentiate between them, conventional algorithms are unable to reliably extract the nasal passage without manual delineation [153]. Hence, the majority of the methods targeted at the nasal structure have been either forced to include all nearby airway components as part of their segmentation [39, 49, 50] or require manual intervention in order to derive results [43-45]. In order to overcome the current limitations of a lack of efficient pipeline for the creation of accurate nasal models, and to meet the increasing demand of more readily available nasal models, an alternative method of nasal cavity model production needs to be considered.

Based on the initial segmentation framework presented in the earlier chapter, this thesis proposes an automated pipeline for the creation of nasal CFD models. In order to validate the usefulness of the proposed pipeline, the output of our segmentation models will be directly compared to the ground truth models in regards to performing CFD of turbulent flow through the nasal cavity. The results of the comparison will demonstrate the effectiveness of our nasal segmentation framework.

6.2 Experimental Setup

Ten pairs of nasal segmentations (from the output of our method and the corresponding ground truth) were arbitrarily selected for conducting CFD simulations. The segmentation output were directly exported

as STL and read into ANSYS SpaceClaim (version 17.0) where the geometry was checked for quality and any remaining spikes or disconnected regions were removed. This cleaned geometry was then read into ANSYS Fluent Meshing (version 17.0) where the inflow and outflow regions were separated from the wall region. A wrapping algorithm was then applied with minimum and maximum surface mesh sizes of typically 0.1 and 2.5 mm, respectively. An arbitrarily dimensioned rectangular prism was introduced as a body of influence which acted as a secondary sizing control limiting the size of surface mesh to a maximum of 0.1 mm in regions of the nasal cavity that were separated by narrow gaps. Once the volumetric region was computed it was automatically meshed using polyhedral elements growing according to the local size field of the region. Inflation was applied at all walls with the Fluent Meshing default algorithm, which uses a first aspect ratio of 10, last aspect ratio of 4.8, growth rate of 1.2 and is set to generate five layers at the walls. Node locations were then automatically adjusted by systematically reducing the threshold for the maximum skewness to approximately 0.6. The nasal geometry was then prepared for solving and a mesh file was produced and imported into the ANSYS Fluent solver. The number of elements per model ranged from 600,000 to about 1,000,000.

The study by Engelhardt et al. [154] which models airflow and particle deposition in the nasal cavity presents calculated Reynolds (Re) numbers for various flow rates. For the breathing rate of 30 L/min a Re > 3000 was calculated, indicating turbulent flow. A flow rate of 30 L/min was selected to replicate fast nasal inhalation as would practically occur with administration of therapeutic nasal sprays. As such, the flow was modelled using the realizable k-ε turbulence model and a target mass flow rate of 6.13×10^{-4} kg/s (30 L/min) set at the pressure outlet, where the static pressure was also set to 0 Pa gauge. The total pressure at the inlet was set to 0 Pa (gauge). The coupled solver was used with convergence achieved when all of the locally scaled residuals fell below 10^{-4}, which typically required 200 iterations.

Once the simulation was converged, Lagrangian particle tracking with a turbulent dispersion model was applied. The particle diameter size distribution is described using the Rosin-Rammler distribution, with the distribution parameters determined from experimental data obtained by analyzing water plumes from a spray bottle using a Malvern Spraytec®. The minimum and maximum diameters were set to 0.12 µm and 1000 µm, respectively, with a mean diameter of 85.8 µm and a spread parameter of 1.92. After the flow had converged, water droplets were injected from each inlet and the simulation completed when all the particles had either escaped from the outlet or collided with the rigid walls of the nasal cavity, which was set to trap particles upon contact.

6.3 Results

CFD simulations of turbulent flow was performed on the ten pairs of nasal models. The case number of the nasal models corresponds to the segmentation outcomes listed in figure 5.2.3.1. For each model, the pressure drop was calculated across the geometry in CFD-Post (Version 17.1) with the majority of the pressure drops ranging from 4–14 Pa (Figure 6.3.1). Between ground truth and segmented models, the results were consistent and not very different from one another except for cases 8 and 18. Additionally, case 12 (not shown) reported a pressure drop of about 100 Pa for both the ground truth model and the segmented model.

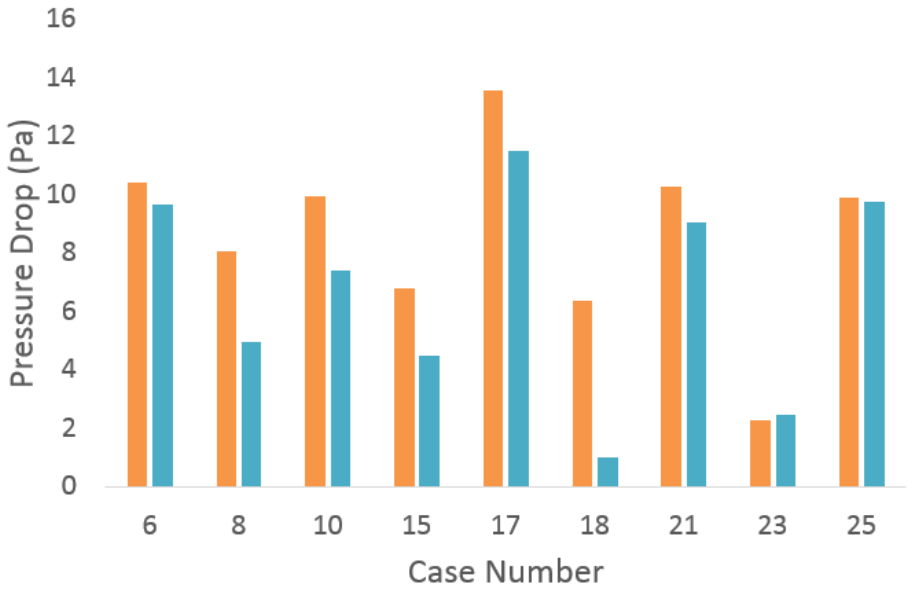

Figure 6.3.1**.** A summary of the pressure drop calculated for the different cases. Results shown in orange are from the ground truth models whereas those in blue are from the segmented models.

The results of case 10 were arbitrarily selected as a representative case to demonstrate the mesh quality, pressure values across the model and the velocity streamlines. In this particular case, the ground truth model had a cell count and maximum cell skewness of 639,000 and 0.6, respectively. The segmented model had approximately 13% increase in the cell count at 734,000, with a maximum cell skewness of 0.65. The mesh and the overall model geometry are shown in Figure 6.3.2.

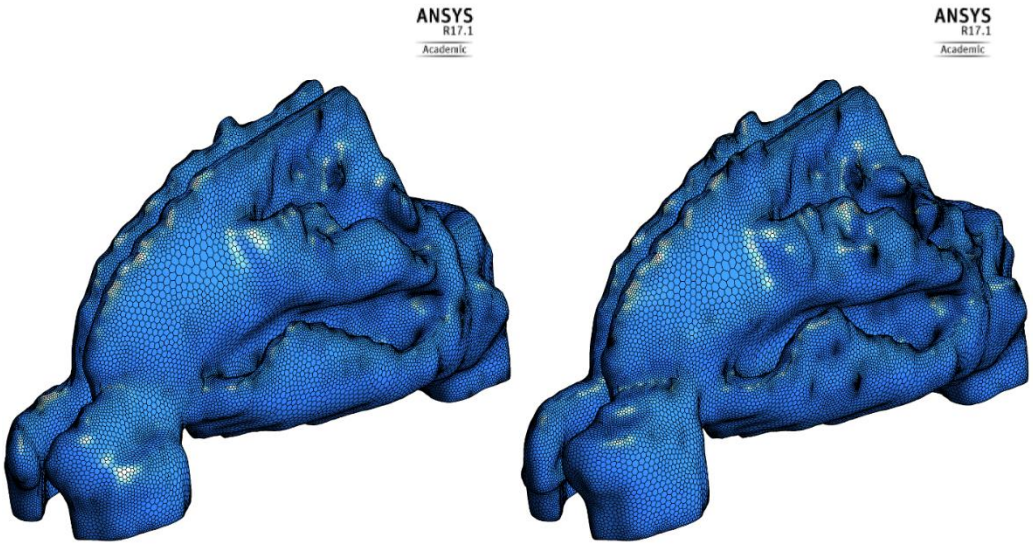

Figure 6.3.2. An image of the geometries showing the computational mesh for the nasal cavity case 10. The model on the left is the ground truth model and on the right is the segmented model.

Figure 6.3.3 shows the geometry used for case 12. When comparing the geometry of case 12 with that of case 10, there exist "lumpy" artefacts highlighted in region 1a which do not exist in the case 10 geometry and are more prominent in the segmented model of case 12. Additionally, region 2a and 2b show a disconnection between the inferior turbinate and the nasopharynx which is consistent in both models in case 12 but does not exist in case 10.

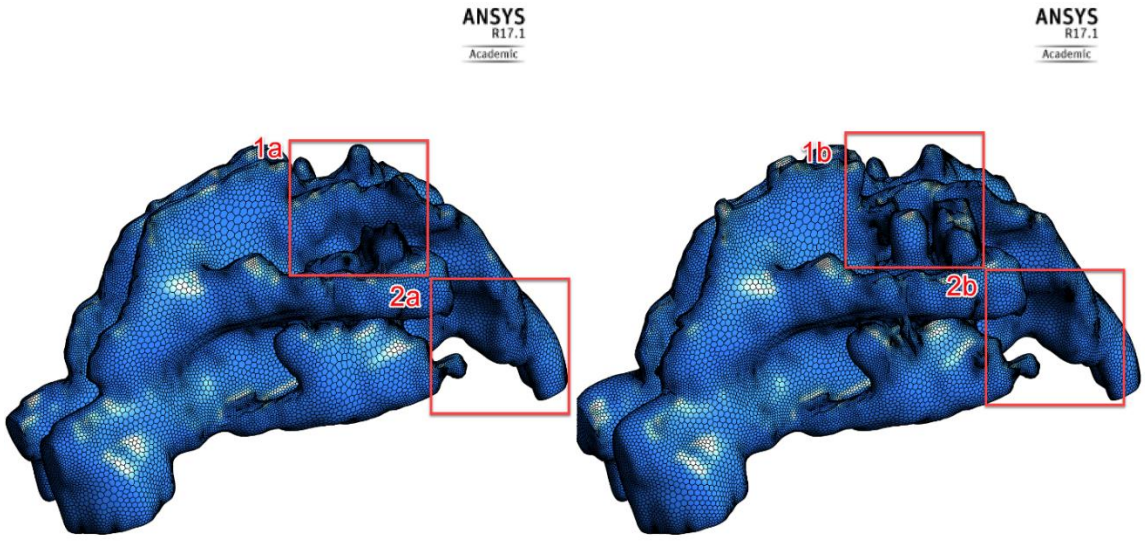

Figure 6.3.4. The geometry of the nasal cavity for case 12. The model on the left is the ground truth model and that on the right is the segmented model. Region 1a and 1b demonstrate the lumpy regions on the model and region 2a and 2b demonstrate a disconnection between the inferior turbinate and the nasopharynx.

Figure 6.3.5 illustrates the geometry used for case 18. When comparing the geometry to both case 10 and case 12 above, there exists another difference in that the inferior turbinate is connected the middle turbinate (present in the region highlighted by the red square). Additionally, when comparing with the two models in case 18, the ground truth model does not show this feature. Moreover, whilst case 18 does not contain lumpy artefacts or disconnected regions like those in case 12, the superior region of the nasal cavity does not appear to be fully formed as in case 10 (Figure 6.3.2). The connection between these two regions was a feature that was also observed in case 8 (not shown).

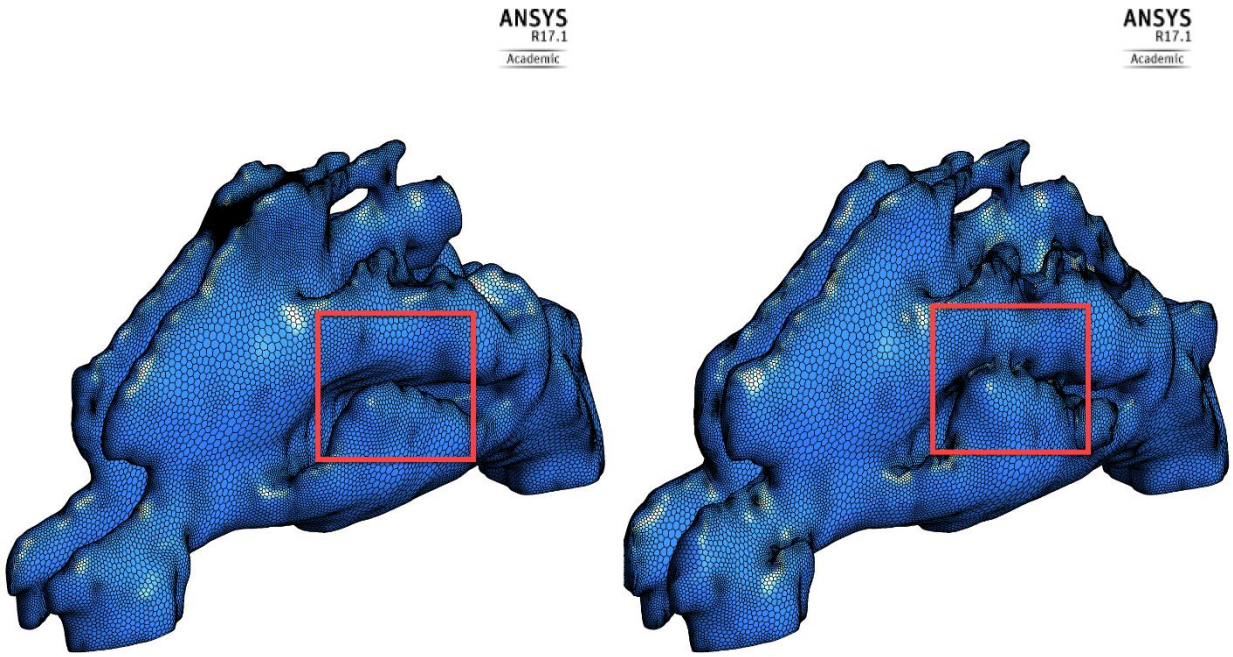

Figure 6.3.5. The nasal cavity geometry for case 18. The model on the left is the ground truth model and that on the right is the segmented model. The region highlighted by the red square shows a narrow connection formed between the inferior and middle turbinates in the segmented model.

The contour plots, shown in Figure 6.3.6, for both the ground truth and segmented models show very similar pressure distributions. There is a region of higher pressure on the left nostril indicated in both models, as well as higher pressure in the superior parts of the nasal cavities where the geometry narrows. The middle and inferior regions show lower pressure when compared with the superior regions and flow results (Figure 6.3.7) indicate the majority of the flow is passing through this region. Additionally, flow passing through this region is travelling at higher velocities (3.6 m/s) when compared with the superior regions (1.29 m/s).

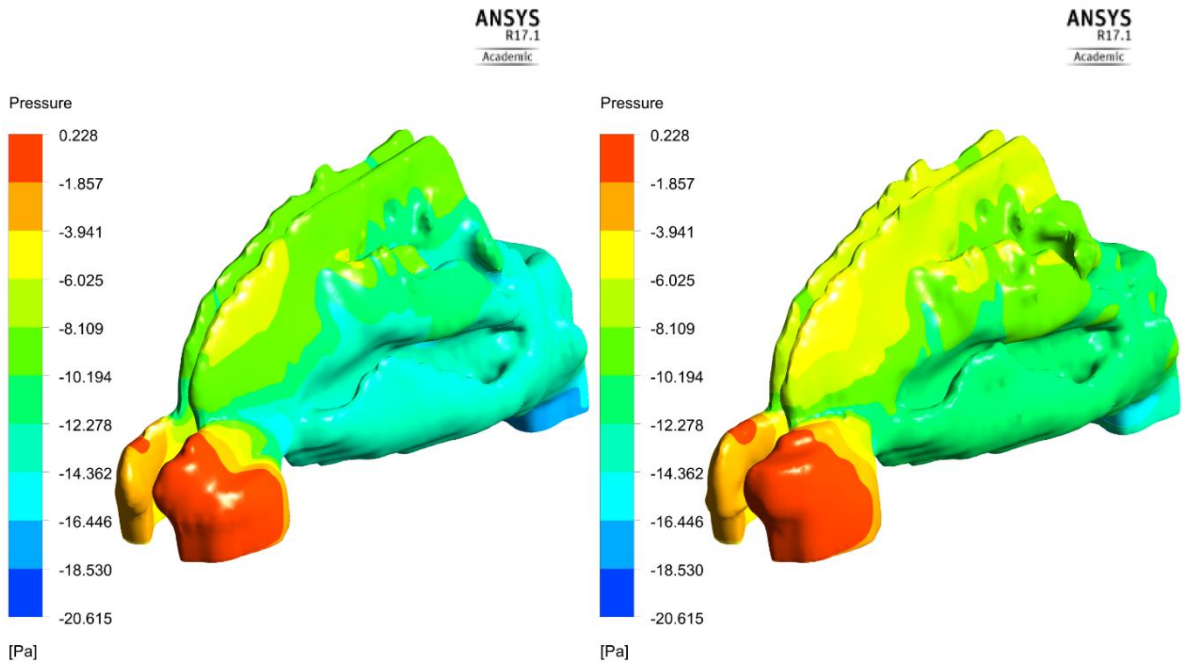

Figure 6.3.6**.** Wall pressure plots for the ground truth model (left) and segmented model (right) indicating the overall change in pressure across the mode from approximately –21 Pa to 0.2 Pa.

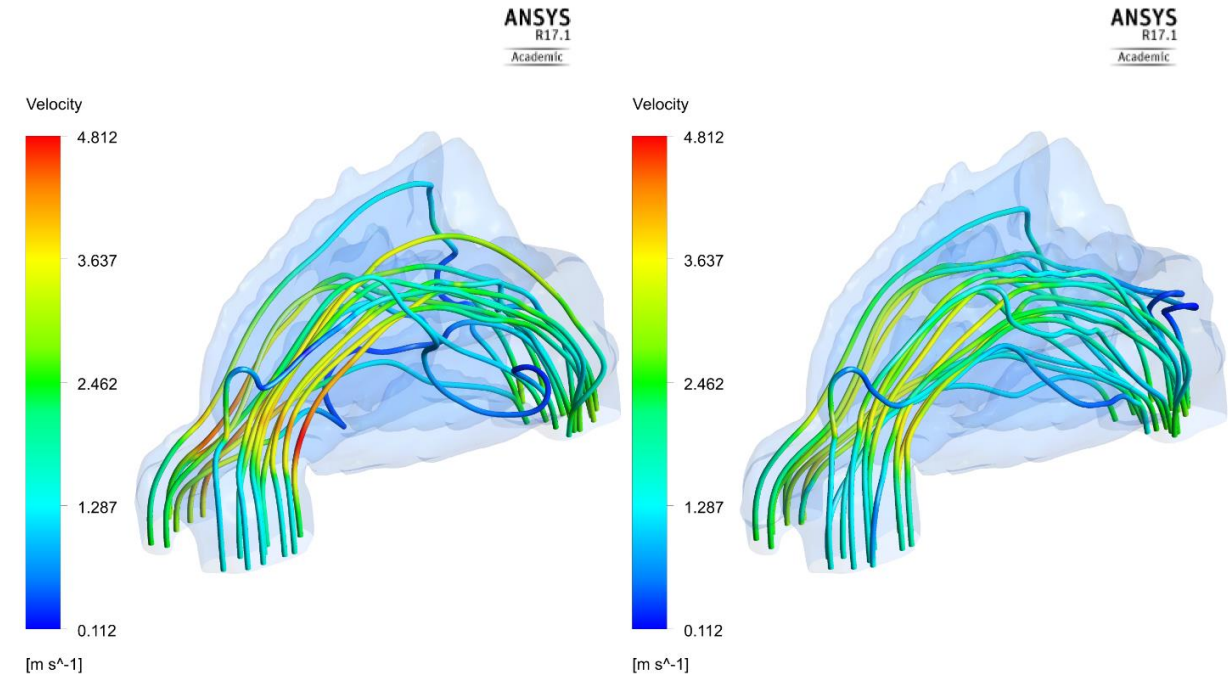

Figure 6.3.7 Streamline plots originating from the inlets for the ground truth (left) and the segmented model (right) coloured by velocity magnitude.

Additionally, an XZ plane was generated approximately halfway through each model (Y = 0.04 m) to display the local velocity at that region (Figure 6.3.8). Higher velocities are observed in the narrower regions of the cross-section with the highest velocity (4.7 m/s) occurring in the region of the middle turbinate of the ground truth model, through which the majority of the flow travels. In this region, the segmented model has a slightly lower velocity (4.2 m/s)

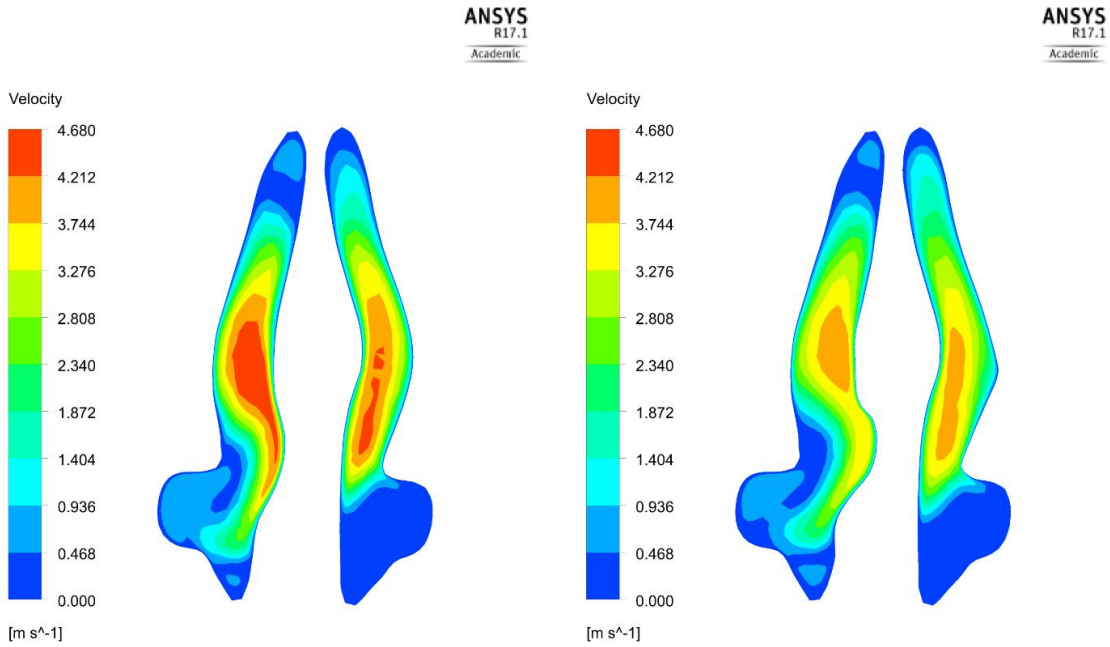

Figure 6.3.8. Local velocity magnitude on and XZ plane located at (Y = 0.04 m). The ground truth model (left) and segmented model (right) show similar patterns but the velocity in the ground truth model is higher.

There was little variation found between the ground truth and segmented models in each case for particle deposition efficiency which was calculated as the mass flow of particles that were trapped in the model during the simulation (Figure 6.3.9). The cases that demonstrated different air flow patterns within each case and when compared with the other cases, had particle deposition results that remained consistent with every other case. The amount of particles trapped ranged from 90% to 97% across the 10 the pairs.

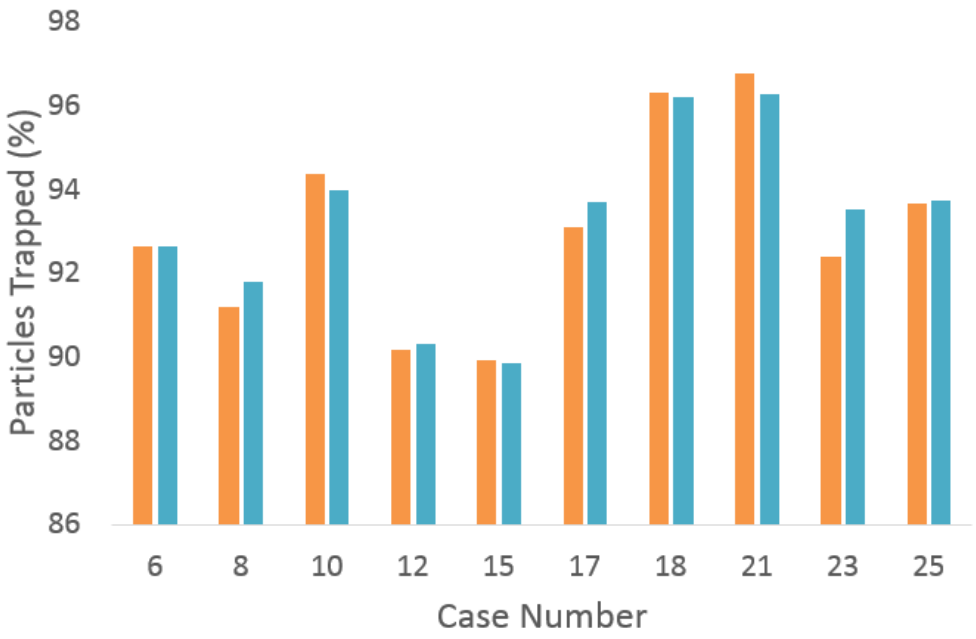

Figure 6.3.9. The percentage of particles trapped by the walls of the nasal geometry for each case: ground truth model (orange) and segmented models (blue).

6.4 Discussion

The primary objective of these simulations was to determine if models produced from our segmentation methods could be used to replace ground truth models as a quicker, more convenient alternative to having to manually segment the nasal cavity. The first apparent difference between the two types of models was the difference in the cell count of the mesh. As a result of the sensitivity of the segmentation process, a large majority of the segmented models have regions in their morphology which are artefacts and do not physically exist in the actual nasal cavity. Regions or lumps were apparent in case 12, particularly in the posterior region of the geometry just above the middle turbinate when comparing the ground truth with segmented models. In some cases, these regions are connected to the main body of the nasal cavity by narrow channels which when meshed produce large cell counts because a large number of small-sized cells are required to resolve these regions. Additionally, case 12 demonstrated a disconnection between the inferior turbinate and the nasopharynx which was not observed in any other case but was consistent within the pair. An explanation of this could be a fault in the CT scans or some underlying pathology in the patient rather than an error in the segmentation as it was present in the ground truth model as well.

These differences in connection of the geometry, particularly in case 12, explain the higher pressure drop that was observed when compared with other cases. Moreover, case 12 had another distinguishing morphological feature in which the nasopharynx region (i.e. outlet) is smaller in cross-sectional area and as such, for the same mass flow passing through attains a lower pressure affecting the overall drop in pressure. The narrow regions which connect the inferior turbinate to the middle turbinate in case 8 and 18 do not contribute to large changes in the external morphology of the nasal cavity, but do change the internal structure. They create small holes within the geometry allowing flow to pass through, creating pressure and velocity differences between the ground truth and segmented models. They alter the expected physical air flow patterns as they are not actual present in the patients from which the CT scans are obtained. The aforementioned artefacts are prominent to some extent in most of the cases analysed and thereby the slight difference in results in the majority of the cases can be attributed to them.

Considering the differences in air flow patterns, it would be expected that the particle deposition results between the cases and across the cases would vary as well. For the given breathing rate which was selected to represent a fast nasal inhalation rate and determined to be turbulent, it would be expected that a large majority of the injected droplets would come into contact with the rigid nasal walls and this was observed. Overall, The results of CFD showed small differences in airflow and particle deposition efficiency between the majority of segmented and ground truth models.

Chapter 7 Conclusion

7.1 Airway Modelling and Segmentation

The work presented in this thesis addressed the problem of the lack of standardized and quantifiable models of the upper airway through the introduction of a robust level set SSM approach capable of modeling the statistics of the nasal cavity using 50 clinical training data. This method was also applied to model the trachea and bronchial airway using 20 PET-CT clinical training data. Non-parametric SDMs were utilized to overcome the challenges of shape correspondence. Experimental results suggested that our proposed SSM was able to accurately capture the majority of variations observed from clinical datasets. Specificity assessment showed the capability of SSM at generating large amounts of valid nasal shape models. A normalized model of the upper airway based on an average of 50 patient image data was further created and 3D-printed. Overall, the constructed nasal SSM is the first of its kind based on a large clinical dataset and will be of benefit to future research in nasal sleep diagnosis, drug delivery and airflow modelling.

A robust RW algorithm adapted with level-set shape priors was implemented to automatically segment the nasal cavity, and thus, demonstrating its capability at separating the targeted structure from its surrounding neighbors in the upper respiratory tract. The superior performance of the proposed algorithm was demonstrated when compared to other well-known segmentation methods. Overall, it is the first automated segmentation algorithm targeted at segmenting the nasal cavity directly. For the trachea and bronchial airway, another fully automated algorithm was presented in this thesis to segment the airway structure under low-contrast CT images. Experimental evaluation was conducted on 20 low-contrast clinical patient studies and resulted in higher segmentation accuracy when compared to other conventional airway segmentation algorithms. The proposed algorithm showed potential at segmenting the trachea airway under pathological conditions.

7.2 Future Work

This thesis presented a framework for modelling the statistics of airway structures and applying knowledge of the anatomy to improve segmentation. Although the initial aims of this thesis may have been achieved, the work conducted could always benefit from additional evaluations and improvements. For the modelling of the upper airway, additional training data would have been of benefit for bringing in more variations and increasing the population-size for measuring the statistics. The modelling of the

paranasal sinuses regions could provide further potential for conducting new experiments as well as be useful for other research. While the models produced from both the constructed SSM and individual segmentations have been tested for 3D-printing, an optimized framework for patient-specific nasal printing can still be derived and established. Further testing samples of the trachea and bronchial airway especially of those containing pathological conditions would also be of benefit and can be used to evaluate the robustness of the proposed algorithm on segmenting disconnected airway.

Appendices

A.1 Acronyms

Acronyms used throughout the thesis and their definition:

ASM: Active Shape Model

CT: Computed Tomography

EVD: Eigenvalue Decomposition

LAP: Laplacian Coordinates

LSDM: Level Set Distribution Model

DRLSE: Distance Regularized Level Set Evolution

GC: Grow-Cut

LC: Local Constraint

MA: Multi-Atlas

MI: Mutual Information

MRI: Magnetic Resonance Imaging

PET-CT: Positron Emission Tomography-Computed Tomography

PCA: Principal Component Analysis

PDM: Point Distribution Model

ROI: Region of Interest

RW: Random Walker

SDF: Signed Distance Function

SDM: Signed Distance Map

SRG: Seeded Region Growing

SSM: Statistical Shape Model

A.2 Eigenvalue Output

Eigenvalues for Nasal SSM

λ in order of decreasing magnitude	$\frac{\lambda}{\sum \lambda}$	Percentage
3.08E+06	1.59E-07	15.87%
2.72E+06	1.4E-07	14.02%
1.82E+06	9.39E-08	9.39%
1.73E+06	8.89E-08	8.89%
1.16E+06	5.97E-08	5.97%
9.02E+05	4.64E-08	4.64%
8.25E+05	4.25E-08	4.25%
5.98E+05	3.08E-08	3.08%
5.69E+05	2.93E-08	2.93%
4.94E+05	2.55E-08	2.55%
4.80E+05	2.47E-08	2.47%
4.52E+05	2.33E-08	2.33%
3.72E+05	1.91E-08	1.91%
3.23E+05	1.66E-08	1.66%
3.05E+05	1.57E-08	1.57%
2.90E+05	1.5E-08	1.50%
2.64E+05	1.36E-08	1.36%
2.25E+05	1.16E-08	1.16%
2.13E+05	1.1E-08	1.10%
2.07E+05	1.07E-08	1.07%
1.95E+05	1.01E-08	1.01%
1.69E+05	8.72E-09	0.87%

1.60E+05	8.22E-09	0.82%
1.51E+05	7.75E-09	0.78%
1.30E+05	6.72E-09	0.67%
1.22E+05	6.26E-09	0.63%
1.13E+05	5.8E-09	0.58%
1.05E+05	5.41E-09	0.54%
9.75E+04	5.02E-09	0.50%
9.48E+04	4.88E-09	0.49%
9.03E+04	4.65E-09	0.47%
8.71E+04	4.49E-09	0.45%
7.98E+04	4.11E-09	0.41%
7.36E+04	3.79E-09	0.38%
7.04E+04	3.63E-09	0.36%
6.54E+04	3.37E-09	0.34%
6.47E+04	3.33E-09	0.33%
6.19E+04	3.19E-09	0.32%
5.66E+04	2.91E-09	0.29%
5.21E+04	2.68E-09	0.27%
5.04E+04	2.6E-09	0.26%
4.75E+04	2.45E-09	0.24%
4.35E+04	2.24E-09	0.22%
4.22E+04	2.17E-09	0.22%
3.83E+04	1.97E-09	0.20%

3.27E+04	1.68E-09	0.17%
3.22E+04	1.66E-09	0.17%
3.08E+04	1.59E-09	0.16%
2.87E+04	1.48E-09	0.15%
0.00E+00	0	0.00%

A3. List of Tools used

The following software were used throughout this study:

- Elastix Registration Toolkit
- GeoS Segmentation
- ITK and VTK Toolkit
- ImageJ
- Matlab
- MITK
- Solidworks

Bibliography

[1] J. F. Nunn, *Applied respiratory physiology*: Butterworth-Heinemann, 2013.

[2] C. V. Pardeshi and V. S. Belgamwar, "Direct nose to brain drug delivery via integrated nerve pathways bypassing the blood-brain barrier: an excellent platform for brain targeting," *Expert opinion on drug delivery,* vol. 10, pp. 957-972, 2013.

[3] A. E. Sher, K. B. Schechtman, and J. F. Piccirillo, "The efficacy of surgical modifications of the upper airway in adults with obstructive sleep apnea syndrome," *Sleep,* vol. 19, pp. 156-177, 1996.

[4] J. M. Marin, S. J. Carrizo, E. Vicente, and A. G. Agusti, "Long-term cardiovascular outcomes in men with obstructive sleep apnoea-hypopnoea with or without treatment with continuous positive airway pressure: an observational study," *The Lancet,* vol. 365, pp. 1046-1053, 2005.

[5] S.-J. Sung, S.-J. Jeong, Y.-S. Yu, C.-J. Hwang, and E.-K. Pae, "Customized three-dimensional computational fluid dynamics simulation of the upper airway of obstructive sleep apnea," *The Angle Orthodontist,* vol. 76, pp. 791-799, 2006.

[6] J. Cisonni, A. D. Lucey, A. J. King, S. M. S. Islam, R. Lewis, and M. S. Goonewardene, "Numerical simulation of pharyngeal airflow applied to obstructive sleep apnea: effect of the nasal cavity in anatomically accurate airway models," *Medical & biological engineering & computing,* pp. 1-11, 2015.

[7] M. Zhao, T. Barber, P. Cistulli, K. Sutherland, and G. Rosengarten, "Computational fluid dynamics for the assessment of upper airway response to oral appliance treatment in obstructive sleep apnea," *Journal of biomechanics,* vol. 46, pp. 142-150, 2013.

[8] G. J. Garcia, N. Bailie, D. A. Martins, and J. S. Kimbell, "Atrophic rhinitis: a CFD study of air conditioning in the nasal cavity," *Journal of applied physiology,* vol. 103, pp. 1082-1092, 2007.

[9] C. M. Hood, R. C. Schroter, D. J. Doorly, E. J. Blenke, and N. S. Tolley, "Computational modeling of flow and gas exchange in models of the human maxillary sinus," *Journal of Applied Physiology,* vol. 107, pp. 1195-1203, 2009.

[10] G.-x. Xiong, J.-M. Zhan, H.-Y. Jiang, J.-F. Li, L.-W. Rong, and G. Xu, "Computational fluid dynamics simulation of airflow in the normal nasal cavity and paranasal sinuses," *American journal of rhinology,* vol. 22, pp. 477-482, 2008.

[11] X. B. Chen, H. P. Lee, H. Chong, V. Fook, and D. Y. Wang, "Assessment of septal deviation effects on nasal air flow: a computational fluid dynamics model," *The Laryngoscope,* vol. 119, pp. 1730-1736, 2009.

[12] G. J. Garcia, J. S. Rhee, B. A. Senior, and J. S. Kimbell, "Septal deviation and nasal resistance: an investigation using virtual surgery and computational fluid dynamics," *American journal of rhinology & allergy,* vol. 24, pp. e46-e53, 2010.

[13] H. P. Lee, H. J. Poh, F. H. Chong, and D. Y. Wang, "Changes of airflow pattern in inferior turbinate hypertrophy: a computational fluid dynamics model," *American journal of rhinology & allergy,* vol. 23, pp. 153-158, 2009.

[14] S. Ozlugedik, G. Nakiboglu, C. Sert, A. Elhan, E. Tonuk, S. Akyar*, et al.*, "Numerical study of the aerodynamic effects of septoplasty and partial lateral turbinectomy," *The Laryngoscope,* vol. 118, pp. 330-334, 2008.

[15] X. B. Chen, H. P. Lee, V. F. H. Chong, and D. Y. Wang, "Impact of inferior turbinate hypertrophy on the aerodynamic pattern and physiological functions of the turbulent airflow—A CFD simulation model," *Rhinology,* vol. 48, p. 163, 2010.

[16] J. Lindemann, H.-J. Brambs, T. Keck, K. M. Wiesmiller, G. Rettinger, and D. Pless, "Numerical simulation of intranasal airflow after radical sinus surgery," *American journal of otolaryngology,* vol. 26, pp. 175-180, 2005.

[17] G. Xiong, J. Zhan, K. Zuo, J. Li, L. Rong, and G. Xu, "Numerical flow simulation in the post-endoscopic sinus surgery nasal cavity," *Medical & biological engineering & computing,* vol. 46, pp. 1161-1167, 2008.

[18] K. Zhao, E. A. Pribitkin, B. J. Cowart, D. Rosen, P. W. Scherer, and P. Dalton, "Numerical modeling of nasal obstruction and endoscopic surgical intervention: outcome to airflow and olfaction," *American journal of rhinology,* vol. 20, pp. 308-316, 2006.

[19] R. A. Segal, G. M. Kepler, and J. S. Kimbell, "Effects of differences in nasal anatomy on airflow distribution: a comparison of four individuals at rest," *Annals of biomedical engineering,* vol. 36, pp. 1870-1882, 2008.

[20] Y. Liu, M. R. Johnson, E. A. Matida, S. Kherani, and J. Marsan, "Creation of a standardized geometry of the human nasal cavity," *Journal of Applied Physiology,* vol. 106, pp. 784-795, 2009.

[21] J. Tan, D. Han, J. Wang, T. Liu, T. Wang, H. Zang*, et al.*, "Numerical simulation of normal nasal cavity airflow in Chinese adult: a computational flow dynamics model," *European Archives of Oto-Rhino-Laryngology,* vol. 269, pp. 881-889, 2012.

[22] S. Yu, Y. Liu, X. Sun, and S. Li, "Influence of nasal structure on the distribution of airflow in nasal cavity," *Rhinology,* vol. 46, pp. 137-143, 2008.

[23] C. V. Pardeshi and V. S. Belgamwar, "Direct nose to brain drug delivery via integrated nerve pathways bypassing the blood–brain barrier: an excellent platform for brain targeting," *Expert opinion on drug delivery,* vol. 10, pp. 957-972, 2013.

[24] H. Shi, C. Kleinstreuer, and Z. Zhang, "Laminar airflow and nanoparticle or vapor deposition in a human nasal cavity model," *Journal of biomechanical engineering,* vol. 128, pp. 697-706, 2006.

[25] K. Inthavong, Q. Ge, C. M. Se, W. Yang, and J. Tu, "Simulation of sprayed particle deposition in a human nasal cavity including a nasal spray device," *Journal of Aerosol Science,* vol. 42, pp. 100-113, 2011.

[26] S. K. Kim, Y. Na, J.-I. Kim, and S.-K. Chung, "Patient specific CFD models of nasal airflow: overview of methods and challenges," *Journal of biomechanics,* vol. 46, pp. 299-306, 2013.

[27] N. Alsufyani, C. Flores-Mir, and P. Major, "Three-dimensional segmentation of the upper airway using cone beam CT: a systematic review," *Dentomaxillofacial Radiology,* 2014.

[28] S. S. Pawar, G. J. Garcia, J. S. Kimbell, and J. S. Rhee, "Objective Measures in Aesthetic and Functional Nasal Surgery–Perspectives on Nasal Form and Function," *Facial plastic surgery: FPS,* vol. 26, p. 320, 2010.

[29] N. Morgan, F. MacGregor, M. Birchall, V. Lund, and Y. Sittampalam, "Racial differences in nasal fossa dimensions determined by acoustic rhinometry," *Rhinology,* vol. 33, pp. 224-228, 1995.

[30] J. Numminen, M. Ahtinen, H. Huhtala, J. Laranne, and M. Rautiainen, "Correlation between rhinometric measurement methods in healthy young adults," *American journal of rhinology,* vol. 16, pp. 203-208, 2002.

[31] J. Lu, D. Han, and L. Zhang, "Accuracy evaluation of a numerical simulation model of nasal airflow," *Acta oto-laryngologica,* vol. 134, pp. 513-519, 2014.

[32] R. L. Walenga, G. Tian, M. Hindle, J. Yelverton, K. Dodson, and P. W. Longest, "Variability in nose-to-lung aerosol delivery," *Journal of aerosol science,* vol. 78, pp. 11-29, 2014.

[33] C. F. Lee, M. Z. Abdullah, K. A. Ahmad, and I. Lutfi Shuaib, "Standardization of Malaysian adult female nasal cavity," *Computational and mathematical methods in medicine,* vol. 2013, 2013.

[34] E. Javaheri, L. Golshahi, and W. Finlay, "An idealized geometry that mimics average infant nasal airway deposition," *Journal of Aerosol Science,* vol. 55, pp. 137-148, 2013.

[35] D. L. Pham, C. Xu, and J. L. Prince, "Current methods in medical image segmentation 1," *Annual review of biomedical engineering,* vol. 2, pp. 315-337, 2000.

[36] T. F. Cootes, C. J. Taylor, D. H. Cooper, and J. Graham, "Active shape models-their training and application," *Computer vision and image understanding,* vol. 61, pp. 38-59, 1995.

[37] V. Blanz and T. Vetter, "A morphable model for the synthesis of 3D faces," in *Proceedings of the 26th annual conference on Computer graphics and interactive techniques*, 1999, pp. 187-194.

[38] L. B. Querol, P. Büchler, D. Rueckert, L. P. Nolte, and M. Á. G. Ballester, "Statistical finite element model for bone shape and biomechanical properties," in *Medical Image Computing and Computer-Assisted Intervention–MICCAI 2006*, ed: Springer, 2006, pp. 405-411.

[39] C. Last, S. Winkelbach, F. M. Wahl, K. W. Eichhorn, and F. Bootz, "A locally deformable statistical shape model," in *Machine Learning in Medical Imaging*, ed: Springer, 2011, pp. 51-58.

[40] D. D. Feng, *Biomedical information technology*: Academic Press, 2011.

[41] S. Kim and S. Chung, "An investigation on airflow in disordered nasal cavity and its corrected models by tomographic PIV," *Measurement Science and Technology,* vol. 15, p. 1090, 2004.

[42] J. Kelly, A. Prasad, and A. Wexler, "Detailed flow patterns in the nasal cavity," *Journal of Applied Physiology,* vol. 89, pp. 323-337, 2000.

[43] K. Tingelhoff, A. I. Moral, M. E. Kunkel, M. Rilk, I. Wagner, K. W. Eichhorn*, et al.*, "Comparison between manual and semi-automatic segmentation of nasal cavity and paranasal sinuses from CT images," in *Engineering in Medicine and Biology Society, 2007. EMBS 2007. 29th Annual International Conference of the IEEE*, 2007, pp. 5505-5508.

[44] A. Seo, S. Chung, J. Lee, J.-I. Kim, and H. Kim, "Semiautomatic segmentation of nasal airway based on collaborative environment," in *Ubiquitous Virtual Reality (ISUVR), 2010 International Symposium on*, 2010, pp. 56-59.

[45] P. Dastidar, T. Heinonen, J. Numminen, M. Rautiainen, and E. Laasonen, "Semi-automatic segmentation of computed tomographic images in volumetric estimation of nasal airway," *European archives of oto-rhino-laryngology,* vol. 256, pp. 192-198, 1999.

[46] H. Shi, W. C. Scarfe, and A. G. Farman, "Upper airway segmentation and dimensions estimation from cone-beam CT image datasets," *International Journal of Computer Assisted Radiology and Surgery,* vol. 1, pp. 177-186, 2006.

[47] T. Iwasaki, I. Saitoh, Y. Takemoto, E. Inada, R. Kanomi, H. Hayasaki*, et al.*, "Evaluation of upper airway obstruction in Class II children with fluid-mechanical simulation," *American Journal of Orthodontics and Dentofacial Orthopedics,* vol. 139, pp. e135-e145, 2011.

[48] A. S. El, H. El, J. M. Palomo, and D. A. Baur, "A 3-dimensional airway analysis of an obstructive sleep apnea surgical correction with cone beam computed tomography," *Journal of Oral and Maxillofacial Surgery,* vol. 69, pp. 2424-2436, 2011.

[49] N. L. Bui, S. H. Ong, and K. W. C. Foong, "Automatic segmentation of the nasal cavity and paranasal sinuses from cone-beam CT images," *International journal of computer assisted radiology and surgery,* pp. 1-9, 2014.

[50] C. Last, S. Winkelbach, F. M. Wahl, K. W. Eichhorn, and F. Bootz, "A model-based approach to the segmentation of nasal cavity and paranasal sinus boundaries," in *Pattern Recognition*, ed: Springer, 2010, pp. 333-342.

[51] X. Chen, H. Lee, V. Chong, and D. Wang, "Drug delivery in the nasal cavity after functional endoscopic sinus surgery: a computational fluid dynamics study," *The Journal of Laryngology & Otology,* vol. 126, pp. 487-494, 2012.

[52] P. Lo, B. Van Ginneken, J. M. Reinhardt, T. Yavarna, P. de Jong, B. Irving*, et al.*, "Extraction of airways from CT (EXACT'09)," *Medical Imaging, IEEE Transactions on,* vol. 31, pp. 2093-2107, 2012.

[53] B. Irving, P. Taylor, and A. Todd-Pokropek, "3D segmentation of the airway tree using a morphology based method," in *Proc. of Second International Workshop on Pulmonary Image Analysis*, 2009, pp. 297-307.

[54] M. Feuerstein, T. Kitasaka, and K. Mori, "Adaptive branch tracing and image sharpening for airway tree extraction in 3-D chest CT," in *Proc. Second International Workshop on Pulmonary Image Analysis*, 2009, pp. 273-284.

[55] P. C. P. Lo, J. Sporring, and M. de Bruijne, "Multiscale vessel-guided airway tree segmentation," in *The Second International Workshop on Pulmonary Image Analysis*, 2009, pp. 323-332.
[56] J. Lee and A. P. Reeves, "Segmentation of the airway tree from chest CT using local volume of interest," in *Proc. of Second International Workshop on Pulmonary Image Analysis*, 2009, pp. 273-284.
[57] X. Wang, C. Fang, Y. Xia, and D. Feng, "Airway segmentation for low-contrast CT images from combined PET/CT scanners based on airway modelling and seed prediction," *Biomedical Signal Processing and Control,* vol. 6, pp. 48-56, 2011.
[58] W. Tan, J. Yang, Z. Bian, Z. Gong, and D. Zhao, "Automatic Extraction of 3D Airway Tree from Multislice Computed Tomography Images," *Journal of Medical Imaging and Health Informatics,* vol. 4, pp. 768-775, 2014.
[59] E. M. Van Rikxoort, W. Baggerman, and B. van Ginneken, "Automatic segmentation of the airway tree from thoracic CT scans using a multi-threshold approach," in *Proc. of Second International Workshop on Pulmonary Image Analysis*, 2009, pp. 341-349.
[60] H. Geng, Z. Bian, J. Yang, W. Tan, and D. Zhao, "Fully automatic extraction of lung parenchyma from CT scans," in *Intelligent Control and Automation (WCICA), 2014 11th World Congress on*, 2014, pp. 5626-5630.
[61] Y. Shang, R. Deklerck, E. Nyssen, A. Markova, J. De Mey, X. Yang*, et al.*, "Vascular active contour for vessel tree segmentation," *Biomedical Engineering, IEEE Transactions on,* vol. 58, pp. 1023-1032, 2011.
[62] Z. Xu, U. Bagci, B. Foster, A. Mansoor, and D. J. Mollura, "Spatially constrained random walk approach for accurate estimation of airway wall surfaces," in *Medical Image Computing and Computer-Assisted Intervention–MICCAI 2013*, ed: Springer, 2013, pp. 559-566.
[63] R. S. J. Estépar, G. G. Washko, E. K. Silverman, J. J. Reilly, R. Kikinis, and C.-F. Westin, "Accurate airway wall estimation using phase congruency," in *Medical Image Computing and Computer-Assisted Intervention–MICCAI 2006*, ed: Springer, 2006, pp. 125-134.
[64] J. Tschirren, E. Hoffman, G. McLennan, and M. Sonka, "Intrathoracic airway trees: segmentation and airway morphology analysis from low-dose CT scans," *Medical Imaging, IEEE Transactions on,* vol. 24, pp. 1529-1539, 2005.
[65] O. Wirjadi, *Survey of 3d image segmentation methods*: ITWM, 2007.
[66] N. Otsu, "A threshold selection method from gray-level histograms," *Automatica,* vol. 11, pp. 23-27, 1975.
[67] T. Ridler and S. Calvard, "Picture thresholding using an iterative selection method," *IEEE transactions on Systems, Man and Cybernetics,* vol. 8, pp. 630-632, 1978.
[68] W. Niblack, *An introduction to digital image processing*: Strandberg Publishing Company, 1985.
[69] K. V. Mardia and T. Hainsworth, "A spatial thresholding method for image segmentation," *Pattern Analysis and Machine Intelligence, IEEE Transactions on,* vol. 10, pp. 919-927, 1988.
[70] W. Oh and W. B. Lindquist, "Image thresholding by indicator kriging," *Pattern Analysis and Machine Intelligence, IEEE Transactions on,* vol. 21, pp. 590-602, 1999.
[71] P. K. Sahoo, S. Soltani, and A. K. Wong, "A survey of thresholding techniques," *Computer vision, graphics, and image processing,* vol. 41, pp. 233-260, 1988.
[72] Y.-L. Chang and X. Li, "Adaptive image region-growing," *Image Processing, IEEE Transactions on,* vol. 3, pp. 868-872, 1994.
[73] R. Adams and L. Bischof, "Seeded region growing," *Pattern Analysis and Machine Intelligence, IEEE Transactions on,* vol. 16, pp. 641-647, 1994.
[74] Z. Lin, J. Jin, and H. Talbot, "Unseeded region growing for 3D image segmentation," in *Selected papers from the Pan-Sydney workshop on Visualisation-Volume 2*, 2000, pp. 31-37.
[75] O. Wirjadi, *Survey of 3d image segmentation methods* vol. 35: ITWM, 2007.

[76] B. Zitova and J. Flusser, "Image registration methods: a survey," *Image and vision computing,* vol. 21, pp. 977-1000, 2003.
[77] J. A. Maintz and M. A. Viergever, "A survey of medical image registration," *Medical image analysis,* vol. 2, pp. 1-36, 1998.
[78] A. Sotiras, C. Davatzikos, and N. Paragios, "Deformable medical image registration: A survey," *Medical Imaging, IEEE Transactions on,* vol. 32, pp. 1153-1190, 2013.
[79] L. Zagorchev and A. Goshtasby, "A comparative study of transformation functions for nonrigid image registration," *Image Processing, IEEE Transactions on,* vol. 15, pp. 529-538, 2006.
[80] F. L. Bookstein, "Principal warps: Thin-plate splines and the decomposition of deformations," *IEEE Transactions on Pattern Analysis & Machine Intelligence,* pp. 567-585, 1989.
[81] D. Rueckert, L. I. Sonoda, C. Hayes, D. L. Hill, M. O. Leach, and D. J. Hawkes, "Nonrigid registration using free-form deformations: application to breast MR images," *Medical Imaging, IEEE Transactions on,* vol. 18, pp. 712-721, 1999.
[82] J. P. Pluim, J. A. Maintz, and M. Viergever, "Mutual-information-based registration of medical images: a survey," *Medical Imaging, IEEE Transactions on,* vol. 22, pp. 986-1004, 2003.
[83] J. P. Pluim, J. A. Maintz, and M. A. Viergever, "Image registration by maximization of combined mutual information and gradient information," in *Medical Image Computing and Computer-Assisted Intervention–MICCAI 2000*, 2000, pp. 452-461.
[84] D. Rueckert, A. F. Frangi, and J. A. Schnabel, "Automatic construction of 3D statistical deformation models using non-rigid registration," in *Medical Image Computing and Computer-Assisted Intervention–MICCAI 2001*, 2001, pp. 77-84.
[85] D. Rueckert, A. F. Frangi, and J. Schnabel, "Automatic construction of 3-D statistical deformation models of the brain using nonrigid registration," *Medical Imaging, IEEE Transactions on,* vol. 22, pp. 1014-1025, 2003.
[86] T. Vrtovec, D. Tomaževič, B. Likar, L. Travnik, and F. Pernuš, "Automated construction of 3D statistical shape models," *Image Analysis & Stereology,* vol. 23, pp. 111-120, 2011.
[87] T. Rohlfing, D. B. Russakoff, and C. R. Maurer, "Expectation maximization strategies for multi-atlas multi-label segmentation," in *Information Processing in Medical Imaging*, 2003, pp. 210-221.
[88] A. Klein, B. Mensh, S. Ghosh, J. Tourville, and J. Hirsch, "Mindboggle: automated brain labeling with multiple atlases," *BMC medical imaging,* vol. 5, p. 7, 2005.
[89] J. E. Iglesias and M. R. Sabuncu, "Multi-Atlas Segmentation of Biomedical Images: A Survey," *arXiv preprint arXiv:1412.3421,* 2014.
[90] J. Ashburner and K. J. Friston, "Unified segmentation," *Neuroimage,* vol. 26, pp. 839-851, 2005.
[91] D. Terzopoulos, A. Witkin, and M. Kass, "Constraints on deformable models: Recovering 3D shape and nonrigid motion," *Artificial intelligence,* vol. 36, pp. 91-123, 1988.
[92] L. D. Cohen, "On active contour models and balloons," *CVGIP: Image understanding,* vol. 53, pp. 211-218, 1991.
[93] C. Xu and J. L. Prince, "Gradient Vector Flow," in *Computer Vision*, ed: Springer, 2014, pp. 349-354.
[94] C. Davatzikos and J. L. Prince, "An active contour model for mapping the cortex," *Medical Imaging, IEEE Transactions on,* vol. 14, pp. 65-80, 1995.
[95] T. McInerney and D. Terzopoulos, "T-snakes: Topology adaptive snakes," *Medical image analysis,* vol. 4, pp. 73-91, 2000.
[96] T. F. Chan and L. Vese, "Active contours without edges," *Image processing, IEEE transactions on,* vol. 10, pp. 266-277, 2001.
[97] B. Chen, J.-h. LAI, B. CHEN, and J.-h. LAI, "Active contour models on image segmentation: a survey," *Journal of Image and Graphics,* vol. 1, p. 002, 2007.
[98] T. McInerney and D. Terzopoulos, "Deformable models in medical image analysis: a survey," *Medical image analysis,* vol. 1, pp. 91-108, 1996.

[99] S. Osher and J. A. Sethian, "Fronts propagating with curvature-dependent speed: algorithms based on Hamilton-Jacobi formulations," *Journal of computational physics,* vol. 79, pp. 12-49, 1988.
[100] J. Montagnat, H. Delingette, and N. Ayache, "A review of deformable surfaces: topology, geometry and deformation," *Image and vision computing,* vol. 19, pp. 1023-1040, 2001.
[101] R. Malladi, J. Sethian, and B. C. Vemuri, "Shape modeling with front propagation: A level set approach," *Pattern Analysis and Machine Intelligence, IEEE Transactions on,* vol. 17, pp. 158-175, 1995.
[102] V. Caselles, R. Kimmel, and G. Sapiro, "Geodesic active contours," *International journal of computer vision,* vol. 22, pp. 61-79, 1997.
[103] M. Weber, A. Blake, and R. Cipolla, "Sparse finite elements for geodesic contours with level-sets," in *Computer Vision-ECCV 2004*, ed: Springer, 2004, pp. 391-404.
[104] C. Li, C. Xu, C. Gui, and M. D. Fox, "Distance regularized level set evolution and its application to image segmentation," *Image Processing, IEEE Transactions on,* vol. 19, pp. 3243-3254, 2010.
[105] D. Cremers, M. Rousson, and R. Deriche, "A review of statistical approaches to level set segmentation: integrating color, texture, motion and shape," *International journal of computer vision,* vol. 72, pp. 195-215, 2007.
[106] C. Li, R. Huang, Z. Ding, J. C. Gatenby, D. N. Metaxas, and J. C. Gore, "A level set method for image segmentation in the presence of intensity inhomogeneities with application to MRI," *Image Processing, IEEE Transactions on,* vol. 20, pp. 2007-2016, 2011.
[107] M. E. Leventon, W. E. L. Grimson, and O. Faugeras, "Statistical shape influence in geodesic active contours," in *Computer Vision and Pattern Recognition, 2000. Proceedings. IEEE Conference on*, 2000, pp. 316-323.
[108] R. Szeliski and D. Tonnesen, *Surface modeling with oriented particle systems* vol. 26: ACM, 1992.
[109] D. Levin, "Mesh-independent surface interpolation," in *Geometric modeling for scientific visualization*, ed: Springer, 2004, pp. 37-49.
[110] M. Alexa and A. Adamson, "On normals and projection operators for surfaces defined by point sets," in *Proceedings of the First Eurographics conference on Point-Based Graphics*, 2004, pp. 149-155.
[111] J. V. Miller, D. E. Breen, W. E. Lorensen, R. M. O'Bara, and M. J. Wozny, "Geometrically deformed models: a method for extracting closed geometric models form volume data," in *ACM SIGGRAPH Computer Graphics*, 1991, pp. 217-226.
[112] J.-O. Lachaud and A. Montanvert, "Deformable meshes with automated topology changes for coarse-to-fine three-dimensional surface extraction," *Medical Image Analysis,* vol. 3, pp. 187-207, 1999.
[113] J. G. Snel, H. W. Venema, and C. Grimbergen, "Deformable triangular surfaces using fast 1-D radial Lagrangian dynamics-segmentation of 3-D MR and CT images of the wrist," *Medical Imaging, IEEE Transactions on,* vol. 21, pp. 888-903, 2002.
[114] B. Willimon, I. Walker, and S. Birchfield, "3D non-rigid deformable surface estimation without feature correspondence," in *Robotics and Automation (ICRA), 2013 IEEE International Conference on*, 2013, pp. 646-651.
[115] H. Delingette, "General object reconstruction based on simplex meshes," *International Journal of Computer Vision,* vol. 32, pp. 111-146, 1999.
[116] B. Gilles, L. Moccozet, and N. Magnenat-Thalmann, "Anatomical modelling of the musculoskeletal system from MRI," in *Medical Image Computing and Computer-Assisted Intervention–MICCAI 2006*, ed: Springer, 2006, pp. 289-296.
[117] B. Gilles and N. Magnenat-Thalmann, "Musculoskeletal MRI segmentation using multi-resolution simplex meshes with medial representations," *Medical image analysis,* vol. 14, pp. 291-302, 2010.

[118] J. Schmid, J. Kim, and N. Magnenat-Thalmann, "Robust statistical shape models for MRI bone segmentation in presence of small field of view," *Medical image analysis,* vol. 15, pp. 155-168, 2011.
[119] T. Heimann and H.-P. Meinzer, "Statistical shape models for 3D medical image segmentation: A review," *Medical image analysis,* vol. 13, pp. 543-563, 2009.
[120] T. F. Cootes and C. J. Taylor, "Active shape models—'smart snakes'," in *BMVC92*, ed: Springer, 1992, pp. 266-275.
[121] D. G. Kendall, "A survey of the statistical theory of shape," *Statistical Science,* pp. 87-99, 1989.
[122] W. E. Lorensen and H. E. Cline, "Marching cubes: A high resolution 3D surface construction algorithm," in *ACM siggraph computer graphics*, 1987, pp. 163-169.
[123] R. H. Davies, C. J. Twining, T. F. Cootes, J. C. Waterton, and C. J. Taylor, "A minimum description length approach to statistical shape modeling," *Medical Imaging, IEEE Transactions on,* vol. 21, pp. 525-537, 2002.
[124] S. Wang, T. Kubota, and T. Richardson, "Shape correspondence through landmark sliding," in *Computer Vision and Pattern Recognition, 2004. CVPR 2004. Proceedings of the 2004 IEEE Computer Society Conference on*, 2004, pp. I-143-I-150 Vol. 1.
[125] B. C. Munsell, P. Dalal, and S. Wang, "Evaluating shape correspondence for statistical shape analysis: A benchmark study," *Pattern Analysis and Machine Intelligence, IEEE Transactions on,* vol. 30, pp. 2023-2039, 2008.
[126] B. C. Munsell, A. Temlyakov, M. Styner, and S. Wang, "Pre-organizing shape instances for landmark-based shape correspondence," *International journal of computer vision,* vol. 97, pp. 210-228, 2012.
[127] D. Cremers, T. Kohlberger, and C. Schnörr, "Shape statistics in kernel space for variational image segmentation," *Pattern Recognition,* vol. 36, pp. 1929-1943, 2003.
[128] A. Wimmer, G. Soza, and J. Hornegger, "A generic probabilistic active shape model for organ segmentation," in *Medical Image Computing and Computer-Assisted Intervention–MICCAI 2009*, ed: Springer, 2009, pp. 26-33.
[129] S. Tomoshige, E. Oost, A. Shimizu, H. Watanabe, and S. Nawano, "A conditional statistical shape model with integrated error estimation of the conditions; Application to liver segmentation in non-contrast CT images," *Medical image analysis,* vol. 18, pp. 130-143, 2014.
[130] Y. Y. Boykov and M.-P. Jolly, "Interactive graph cuts for optimal boundary & region segmentation of objects in ND images," in *Computer Vision, 2001. ICCV 2001. Proceedings. Eighth IEEE International Conference on*, 2001, pp. 105-112.
[131] L. Grady, "Random walks for image segmentation," *Pattern Analysis and Machine Intelligence, IEEE Transactions on,* vol. 28, pp. 1768-1783, 2006.
[132] A. Criminisi, T. Sharp, and A. Blake, "Geos: Geodesic image segmentation," in *Computer Vision–ECCV 2008*, ed: Springer, 2008, pp. 99-112.
[133] X. Wang, C. Zheng, C. Li, Y. Yin, and D. D. Feng, "Automated CT liver segmentation using improved Chan-Vese model with global shape constrained energy," in *Engineering in Medicine and Biology Society, EMBC, 2011 Annual International Conference of the IEEE*, 2011, pp. 3415-3418.
[134] X. Qin, X. Li, Y. Liu, H. Lu, and P. Yan, "Adaptive shape prior constrained level sets for bladder MR image segmentation," *Biomedical and Health Informatics, IEEE Journal of,* vol. 18, pp. 1707-1716, 2014.
[135] M. A. Styner, K. T. Rajamani, L.-P. Nolte, G. Zsemlye, G. Székely, C. J. Taylor*, et al.*, "Evaluation of 3D correspondence methods for model building," in *Information processing in medical imaging*, 2003, pp. 63-75.

[136] T. Heimann, B. Van Ginneken, M. A. Styner, Y. Arzhaeva, V. Aurich, C. Bauer*, et al.*, "Comparison and evaluation of methods for liver segmentation from CT datasets," *Medical Imaging, IEEE Transactions on,* vol. 28, pp. 1251-1265, 2009.

[137] J. S. Rhee, "Measuring outcomes in nasal surgery: realities and possibilities," *Archives of facial plastic surgery,* vol. 11, pp. 416-419, 2009.

[138] S. Klein, M. Staring, K. Murphy, M. A. Viergever, and J. P. Pluim, "Elastix: a toolbox for intensity-based medical image registration," *Medical Imaging, IEEE Transactions on,* vol. 29, pp. 196-205, 2010.

[139] E. van Rikxoort, Y. Arzhaeva, and B. van Ginneken, "Automatic segmentation of the liver in computed tomography scans with voxel classification and atlas matching," in *Proceedings of the MICCAI Workshop 3-D Segmentation Clinic: A Grand Challenge*, 2007, pp. 101-108.

[140] V. Vezhnevets and V. Konouchine, "GrowCut: Interactive multi-label ND image segmentation by cellular automata," in *proc. of Graphicon*, 2005, pp. 150-156.

[141] E. Day, J. Betler, D. Parda, B. Reitz, A. Kirichenko, S. Mohammadi*, et al.*, "A region growing method for tumor volume segmentation on PET images for rectal and anal cancer patients," *Medical physics,* vol. 36, pp. 4349-4358, 2009.

[142] W. Casaca, L. G. Nonato, and G. Taubin, "Laplacian Coordinates for Seeded Image Segmentation," in *Computer Vision and Pattern Recognition (CVPR), 2014 IEEE Conference on*, 2014, pp. 384-391.

[143] Y. Song, W. Cai, H. Huang, X. Wang, Y. Zhou, M. J. Fulham*, et al.*, "Lesion detection and characterization with context driven approximation in thoracic FDG PET-CT images of NSCLC studies," *Medical Imaging, IEEE Transactions on,* vol. 33, pp. 408-421, 2014.

[144] J. Kim, L. Wen, S. Eberl, R. Fulton, and D. D. Feng, "Use of anatomical priors in the segmentation of PET lung tumor images," in *Nuclear Science Symposium Conference Record, 2007. NSS'07. IEEE*, 2007, pp. 4242-4245.

[145] L. Bi, J. Kim, L. Wen, and D. D. Feng, "Automated and robust PERCIST-based thresholding framework for whole body PET-CT studies," in *Engineering in Medicine and Biology Society (EMBC), 2012 Annual International Conference of the IEEE*, 2012, pp. 5335-5338.

[146] L. Bi, J. Kim, L. Wen, A. Kumar, M. Fulham, and D. D. Feng, "Cellular automata and anisotropic diffusion filter based interactive tumor segmentation for positron emission tomography," in *Engineering in Medicine and Biology Society (EMBC), 2013 35th Annual International Conference of the IEEE*, 2013, pp. 5453-5456.

[147] M. Scaglione, S. Romano, A. Pinto, A. Sparano, M. Scialpi, and A. Rotondo, "Acute tracheobronchial injuries: Impact of imaging on diagnosis and management implications," *European journal of radiology,* vol. 59, pp. 336-343, 2006.

[148] Y. Jung, J. Kim, M. Fulham, and D. D. Feng, "Opacity-driven volume clipping for slice of interest (SOI) visualisation of multi-modality PET-CT volumes," in *Engineering in Medicine and Biology Society (EMBC), 2014 36th Annual International Conference of the IEEE*, 2014, pp. 6714-6717.

[149] J.-H. Lee, Y. Na, S.-K. Kim, and S.-K. Chung, "Unsteady flow characteristics through a human nasal airway," *Respiratory physiology & neurobiology,* vol. 172, pp. 136-146, 2010.

[150] D. Taylor, D. Doorly, and R. Schroter, "Inflow boundary profile prescription for numerical simulation of nasal airflow," *Journal of the Royal Society Interface,* vol. 7, pp. 515-527, 2010.

[151] Y. Na, K. Kim, S. K. Kim, and S.-K. Chung, "The quantitative effect of an accessory ostium on ventilation of the maxillary sinus," *Respiratory physiology & neurobiology,* vol. 181, pp. 62-73, 2012.

[152] X. B. Chen, H. P. Lee, V. F. H. Chong, and D. Y. Wang, "Numerical simulation of the effects of inferior turbinate surgery on nasal airway heating capacity," *American journal of rhinology & allergy,* vol. 24, pp. e118-e122, 2010.

[153] R. Huang, A. Li, L. Li, C. Li, P. Young, G. King*, et al.*, "A Locally Constrained Statistical Shape Model for Robust Nasal Cavity Segmentation in Computed Tomography," in *International Symposium on Biomedical Imaging: From Nano to Macro (ISBI)*, 2016, pp. 1-4.

[154] L. Engelhardt, M. Röhm, C. Mavoungou, K. Schindowski, A. Schafmeister, and U. Simon, “First steps to develop and validate a CFPD model in order to support the design of nose-to-brain delivered biopharmaceuticals," *Pharmaceutical research*, vol. 33, no. 6, pp. 1337-1350, 2016.

[155] Grady, Leo. "Multilabel random walker image segmentation using prior models." Computer Vision and Pattern Recognition, 2005. CVPR 2005. IEEE Computer Society Conference on. Vol. 1. IEEE, 2005.

[156] Baudin, P-Y., et al. "Prior knowledge, random walks and human skeletal muscle segmentation." International Conference on Medical Image Computing and Computer-Assisted Intervention. Springer Berlin Heidelberg, 2012.